Thermal Convection in Liquid Metal Blankets for Tokamak Fusion Reactors

by

Xuan Zhang

A dissertation submitted in partial fulfillment
of the requirements for the degree of
Doctor of Philosophy
(Automotive Systems Engineering)
in the University of Michigan-Dearborn
2017

Doctoral Committee:

Professor Oleg Zikanov, Chair
Professor Ghassan Kridli
Assistant Professor Patrick Lynch
Professor Pravansu Mohanty

ACKNOWLEDGEMENTS

I would like to express my special thanks to my advisor Prof. Oleg Zikanov for his extensive direction to both the research and my scientific education. His unlimited supply of encouragement, patience and extraordinary support are invaluable to me.

I would like to thank my fellow labmates for the stimulating discussion and the memorable time we work together.

Thanks also go to my family for supporting me spiritually throughout my Ph.D. study and my life in general.

Thanks for the financial supports from US NSF (Grant CBET 1232851 and CBET 1435269) and from the Interdisciplinary Engineering Programs.

TABLE OF CONTENTS

LIST OF FIGURES

Figure

LIST OF TABLES

Table

ABSTRACT

Thermal convection in liquid metal flows with strong heating and strong imposed magnetic fields is studied numerically using the method of direct numerical simulation (DNS). The goal is to understand the effect of convection in ducts of conceptual liquid metal blankets of fusion reactors. Models related to two types of the blankets are explored: a separately cooled blanket with walls maintained at constant temperature and no significant mean flow along the duct and a dual-coolant blanket with thermally insulating walls and non-negligible mean flow. The results for three configurations of a toroidal duct and one configurations of a poloidal duct are presented.

In the flow within a toroidal (horizontal) duct of a separately cooled blanket, turbulent convection appears at high Grashof number when the magnetic field is purely axial. Flow maintains good two-dimensionality at parameters close to the conditions of a real fusion reactor. A weaker (5% in amplitude of the axial component) vertical magnetic field (induced by the currents in the plasma) suppresses the turbulence, elongates convection structures, and leads to formation of strong shear layers and near-wall jets. Stability analysis reveals that the transformation makes the flow more unstable to three-dimensional perturbations. In the flow within a toroidal (horizontal) duct of a dual-coolant blanket, the flow develops strong thermal convection in the transverse plane at moderate Grashof numbers. At large Grashof numbers, the flow is dominated by the top-bottom asymmetry of the streamwise velocity and stable stratification of temperature, which are caused by the buoyancy force due to the mean temperature growing along the duct. This leads to suppression of thermal convection, weak mixing, and substantial gradients of wall temperature. In the flow within

a poloidal (vertical) duct of a dual-coolant blanket, three regimes: steady-state, intermittent, or unstable with developed instability, are found at different parameters. The results of a parametric study show that the flow behavior is dominated by the buoyancy effect and magnetic damping together. At the conditions close to those of a fusion reactor, the flow is likely to be unstable with developed instability. Temperature fluctuations appear in the flow, which is detrimental to the blanket operation.

Keywords Thermal convection, Magnetohydrodynamics, Liquid metal blanket

CHAPTER I

Introduction

1.1 Fusion reactor and blanket

The work presented in this dissertation is motivated by the design of liquid metal blankets of future Tokamak nuclear fusion reactors. It is one of the most-researched devices on the way to controlled thermonuclear fusion power production. In such reactors, a strong magnetic field is used to confine the plasma in a toroidal chamber, where the fusion reaction takes place. As shown in Fig. 1.1, electromagnets are arranged surrounding the torus.

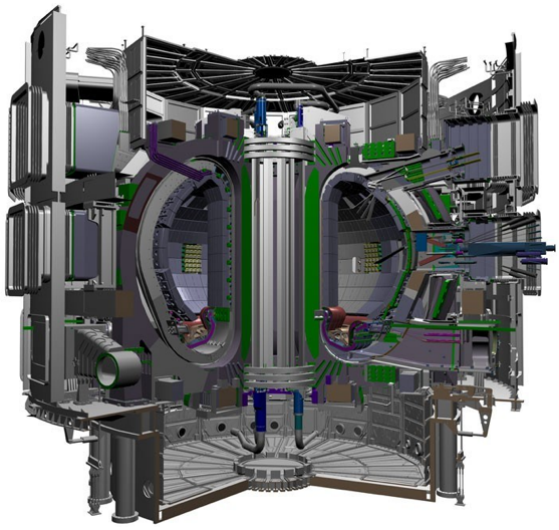

Figure 1.1: Structure of the Tokamak nuclear fusion reactor in ITER (International Thermonuclear Experimental Reactor) (www.iter.org).

These magnets generate an extremely strong magnetic field (4-12 T) along the toroidal direction. A secondary weaker, but still strong magnetic field is produced by the axial electric currents glowing through the plasma along the poloidal direction (see Fig. 1.2). These magnetic fields achieve the confinement of the extremely hot plasma (the temperature of the order of 10^8 K) in such a way that it does not touch the walls. This is necessary because no solid material can withstand contact with such plasma.

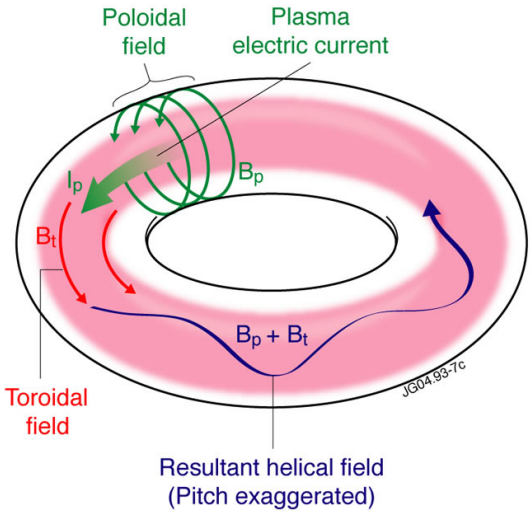

Figure 1.2: Structure of Magnetic field in a Tokamak (www.euro-fusion.org).

The main fusion reaction in the chamber is presented as:

$$T + D \rightarrow^4 He + n + 17.6\ MeV, \tag{1.1}$$

where T is the tritium and D is the deuterium [8]. Deuterium is naturally abundant in Earth's oceans, while tritium is rare. The low availability of tritium is one of the obstacles on the way of practical use of fusion energy. One possible way to produce tritium is the neutron activation of lithium-6:

$$n +^6 Li \rightarrow^4 He + T + 4.8\ MeV. \tag{1.2}$$

In the fusion reaction (1.1), high-energy neutrons and a huge amount of heat flux are generated. Neutrons are electrically neutral and cannot be confined magnetically in the plasma. Some measures are needed to protect the electromagnets and other exterior reactor components from hitting by the neutrons and the high heat flux. One also needs a device for conversion of the neutron's kinetic energy and the reaction heat flux into heat and transport of the heat into exterior conventional electricity generation cycle. Finally, a device, where the tritium fuel is produced via the reaction (1.2) is required. In the currently designed reactors, these purposes of shielding, power conversion, and tritium breeding are served by a single device - the breeder blanket (see Fig. 1.1 and 1.3).

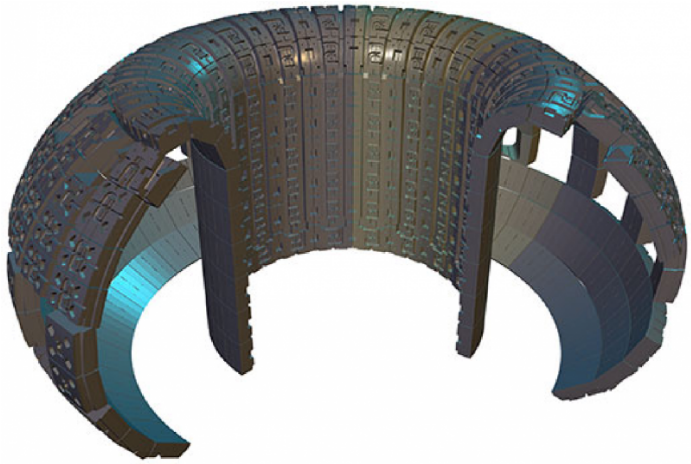

Figure 1.3: Blanket modules in Tokamak (www.iter.org).

Many types of blanket interior design have been proposed: ceramic breeder blanket, molten salts blanket, liquid metal blanket, etc (see [9] for a review). In this work, we focus on the liquid metal blanket, which has critical advantages over the competitors by providing higher thermal efficiency and the possibility of long-term continuous operation.

As mentioned above, to achieve the breeding purpose, lithium-containing liquid metals are used in the blanket. The eutectic lead-lithium alloy (Li(17)Pb(83)) is the primary choice due to its low reactivity with water and air compared to pure Li. Throughout the dissertation, we use the physical properties of PbLi in the estimates of the practically rel-

evant parameters. The wall of a blanket facing reaction chamber (the so-called first wall) is subjected to much stronger heat flux due to the energy released from the reaction. The heat generated from the capture of neutrons (up to 20 MW/m^2) and breeding reaction is distributed in the volume of the flow.

There are three main concepts of the liquid metal blanket that have been intensively studied in recent decades: self-cooled blanket, dual-coolant blanket and separately-cooled blanket.

Self-cooled blanket is the earliest pursued concept due to its design simplicity. In such a blanket the liquid metal serves three purposes stated above. It is pumped at high flow rate through a system of ducts and manifolds. Magnetohydrodynamic (MHD) effects are found to be critical for this concept, especially the high MHD pressure drop resulting in the pressure stress exceeding the structural material limits of the walls of the ducts [10]. The MHD pressure drop results from the interaction between the liquid metal flowing at high rate and the magnetic field. The problem could be alleviated by electrical insulation of the inner surface of the ducts. Such insulation has, however, proven difficult to design due to low tolerance of coatings to cracks and other insulation defects [11, 12]. Thus, the feasibility of the concept largely depends on the successful overcoming of this obstacle.

Separately-cooled blanket was proposed to solve the MHD pressure drop problem. Here, the liquid metal only serves for breeding of tritium, while heat is removed by an external coolant (water or pressurised helium gas) circulating within the walls. A typical example is the helium-cooled lead-lithium (HCLL) blanket. It is currently developed in Europe [13, 14] and considered to be used in fusion power reactors in future. It is also a candidate for testing in the ITER [15]. As the entire thermal power is designed to be diverted by the external cooling system, only a weak flow of a liquid metal is needed (0.1-1 mm/s) for the purpose of tritium extraction and purification. The MHD pressure drop issue is relived significantly in this design. But it requires more complicated fabrication techniques. Furthermore, due to small flow velocity, tritium permeation from PbLi into

walls and coolant would be a safety issue. In particular, no stagnant flow regions are allowed in this design to avoid high tritium losses.

Dual-coolant blanket concept is a combination of these two ideas. It uses an auxiliary coolant such as Helium (He) to remove the heat flux on the first wall, and the flow of liquid metal to divert the volumetric heat flux inside the blanket module. DCLL (Dual Coolant Lead Lithium) blanket is a typical example of this concept and it is currently developed in the US as a candidate for testing in DEMO reactor [16, 1, 17]. The velocity of liquid metal flow is about 10 cm/s. Electrical insulation is needed at such velocity to reduce the MHD pressure effect. Flow Channel Inserts (FCI) made of composite or porous SiC is proposed to be a key element to achieve the insulation but its study is still underway. The advantage of this concept is that, as the walls of the duct are thermally insulated by the inserts, the working temperature can be much higher than in a self-cooled blanket, and thus the thermal efficiency is improved significantly.

One example of DCLL blanket module is shown in Fig. 1.4. There are several ducts oriented poloidally in a blanket module. The eutectic alloy PbLi circulates slowly in long ($\sim$ 2 m) ducts. Additional cooling of the first wall is carried out by pressurized helium. The SiC FCI are used to cover the duct walls.

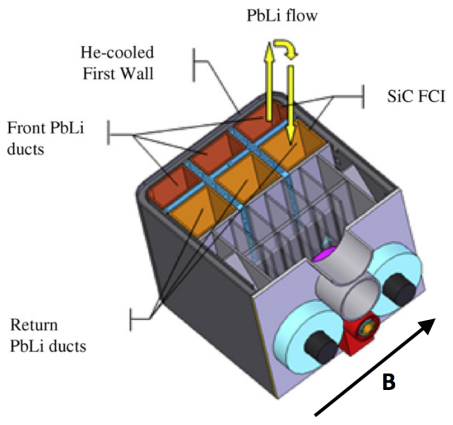

Figure 1.4: Schematic sketch of a DCLL blanket [1]. B is the main (toroidal) component of the magnetic field. The fusion reactor chamber is on the side of the first wall.

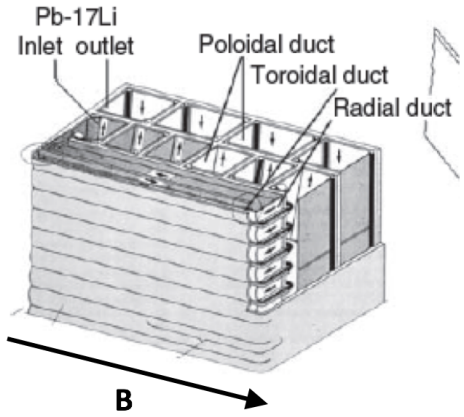

Figure 1.5: Schematic sketch of a self-cooled blanket with toroidal ducts [2]. B is the main (toroidal) component of the magnetic field. The toroidally oriented ducts are located at the first wall.

There are also designs of blanket module with most of the ducts oriented toroidally (see Fig. 1.5). This concept of blanket was proposed in the 1970s as a self-cooled blanket. The liquid metal in the toroidal ducts are pumped very fast to divert the heat by the flow itself. The duct walls are electrically and thermally insulated. Some poloidal manifolds are used to collect PbLi.

In this dissertation, the flow and heat transfer in the main elements of the blankets - long ducts oriented toroidally or poloidally will be analyzed. The typical dimensions of the ducts in the currently considered designs are: length of 1-2 m and width 10-20 cm.

1.2 Liquid metal blanket development and challenges

As described in section 1.1, each blanket concept has its feasibility issues related to design complexity, reliability, thermal efficiency, safety, etc. These concerns partially arise from the MHD effects. In particular, development of the most efficient self-cooled blankets has been largely suspended in the recent decades due to the extremely high MHD pressure gradient. Development of separately cooled blankets requires further investigation

of reliable wall materials to prevent tritium permeation into the helium. The dual-coolant blanket, while a popular choice studied widely around the world in recent years, is also not free from unsolved problems.

The main challenge present in all the blanket concepts is that the strong magnetic field affects the velocity distribution in the flowing liquid metal. The strength of the magnetic field is about 4 T in the blanket area of the ITER and is expected to be as strong as 10-12 T in the next generation DEMO reactor. Such a strong magnetic field makes it difficult or even impossible to do experiments at the conditions, similar to those of a fusion reactor, in a laboratory. The lack of experimental information makes the numerical modeling particularly important in the blanket studies.

Another challenge is the extremely strong heating (up to 20 MW/m^2) suffered by the blanket which is also hard to be reached in a laboratory experiment. It is difficult to find a heating technique to mimic the non-uniform volumetric internal heating associated with absorption of neutrons. As demonstrated further in this dissertation, the combination of a strong magnetic field, and strong heating makes the flows of liquid metals in the blanket highly unusual, counterintuitive, and impossible to predict on the basis of common knowledge and experience.

Though we introduce the blanket designs here, we are not going to discuss specific design concepts in this dissertation. The focus will be on the fundamental physics of the liquid metal flows in the blanket conditions, specifically on the thermal convection in the presence of very strong magnetic fields.

1.3 Magnetohydrodynamics (MHD) effects

Magnetohydrodynamics (MHD) is a scientific field dealing with the mutual interaction of flows of electrically conducting fluids and magnetic fields. Such fluids can be liquid metals, plasmas or electrolytes [18]. The interaction of a magnetic field and a moving fluid can be generally described, in the non-relativistic approximation, by the laws of Faraday

and Ampere, and the Lorentz force experienced by the fluid. Details of these laws in their application to liquid metals are discussed in Chapter II. Here we briefly summarize the general MHD effects involved in the operation of liquid metal blankets as follows: suppression of turbulence, generation of large pressure drop in a duct flow, and complete change of the nature of common hydrodynamic instabilities.

1.4 Thermal convection effects

As we mentioned in section 1.2, the two main physical effects that determine the blanket operation are the strong magnetic field and strong heat flux. Many investigations have been carried out to study the first effect, resulting in the awareness of the challenging problem of the MHD pressure drop in the case of conducting walls in all blanket designs (see [1, 19]), and the expectation of reduced heat and mass transfer due to the suppression of turbulence by the magnetic field. However, the second effect, strong heat flux, has not received sufficient attention. It was assumed that the resulting heat transfer would be entirely passive, i.e. fully determined by the flow. The possible effect of the natural thermal convection on the flow was ignored.

We understand now that thermal convection is significant in the presence of strong heat flux present in the blanket. Importantly, the flow structures and properties are changed profoundly by the convection. This was first found in the experiments with mercury flows in pipes and ducts [see, e.g. 20, 21, 22, 23, 24, 25]. Later, numerical computations [26, 27, 28, 29, 30, 31, 32, 33] have confirmed that the convection effect is critical to the flow behavior. In some configurations, convection leads to large-amplitude slow (with the period $\sim 1\,s$) fluctuations of temperature and velocity [22, 23, 25, 27, 29, 33]. These fluctuations lead to strong and unsteady thermal stresses in the walls, safety issues which may lead to loss of structural integrity of the blanket. Such findings make it even more important to understand the thermal convection in a flow of a liquid metal in strong magnetic field.

The possibility of destructive large-amplitude temperature fluctuations is particularly

troubling because the fluctuations are found in the poloidally oriented ducts (see Fig. 1.2), i.e. in the configurations at the center of the currently actively pursued blanket designs (see Fig. 1.3). This it invites us to analyze the effect more thoroughly, and also to revisit an alternative concept of a toroidal blanket.

1.5 Blanket with toroidal ducts

The toroidal blanket is an old concept firstly proposed in 1970s [34]. In such a blanket, most ducts are oriented toroidally, i.e. parallel to the main component of the magnetic field (see Fig. 1.4). The study of this concept was active during 1980s to 1990s [2, 35, 36, 37, 38, 39, 40, 41]. This idea was finally abandoned in the 1990s. Many reasons of that were cited in the literature (see the chapter by L. Bühler in [42]), such as the MHD pressure drop in the non-toroidal manifolds, complex and poorly predictable behavior, electromagnetic coupling between the ducts (the Madarame effect), etc. However, all the previous studies did not take the thermal convection into consideration. As thermal convection has been realized to be critical to the flow behavior in recent years, this is a serious drawback, which largely invalidate the conclusions. This invites us to revisit the concept analyzing it in the framework of a full physical model.

1.6 Objectives

The general purpose of this work is to use numerical methods to study how the thermal convection affects the liquid metal flows in strong magnetic fields. Several idealized configurations, in which the convection effect has never been analyzed before, are considered.

Through analysis of different configurations using high-resolution numerical simulations, we attempt to answer the following questions:

1. Does the concept of a toroidal blanket serve as a solution to avoid high-amplitude temperature fluctuations.

2. Does convection generate sufficient rate of heat and mass transfer in the toroidal blanket.

3. Which version of a toroidal blanket is preferable.

4. Are there temperature fluctuations in a poloidal duct with downward flow at conditions close to those of a reactor.

The study is theoretical and is not directly related to any currently pursued design of the blanket. The results will, however, benefit the blanket design by providing more understanding of behavior of liquid metal flows in the fusion reactor conditions.

1.7 Outline of the Thesis

In the next chapter, we discuss the MHD equations and physical models used in the study. Starting from the basic laws used in MHD problems, we introduce the MHD approximations suitable for liquid metal flows in blankets, and then present the governing equations of two-dimensional and three-dimensional flows. The numerical methods developed for different models are also presented. The basic scheme of each solver, the boundary condition treatment and the clustering schemes are introduced in detail.

From Chapter III to Chapter VI, in each chapter we discuss the results of one configuration corresponding to a certain idealized blanket model. Convection is found as either beneficial or detrimental to the blanket operation in each configuration. They all confirm that, the thermal convection is the key factor in determining liquid metal behavior at the fusion reactor conditions, and should always be considered in future development of the blanket.

CHAPTER II

Governing Equations and Models

2.1 Physical models

2.1.1 Basic laws

In general, the equations consist of conservation of mass, conservation of linear momentum, conservation of energy and the MHD electrodynamic equations.

We consider the liquid metal flow as incompressible, thus the conservation of mass is represented by (2.1), where $\boldsymbol{u}$ is the velocity field. In the conservation of momentum (2.2), P is the pressure field, and $\boldsymbol{f}$ is the force which consists of buoyancy force and Lorentz force. ρ and ν are the density and kinematic viscosity of the liquid metal, respectively. In the conservation of energy (2.3), Q represents the internal heating source. c_p is the heat capacity and κ is the heat conductivity of the flow.

$$\text{Conservation of mass} \qquad \nabla \cdot \boldsymbol{u} = 0 \tag{2.1}$$

$$\text{Conservation of momentum} \qquad \frac{\partial \boldsymbol{u}}{\partial t} + (\boldsymbol{u} \cdot \nabla)\boldsymbol{u} = -\frac{1}{\rho}\nabla P + \nu \nabla^2 \boldsymbol{u} + \boldsymbol{f} \tag{2.2}$$

$$\text{Conservation of mass} \qquad \rho c_p [\frac{\partial T}{\partial t} + (\boldsymbol{u} \cdot \nabla)T] = \kappa \nabla^2 T + Q. \tag{2.3}$$

For the electromagnetic effects, we start with the Maxwell's equations:

$$\text{Gauss's Law} \qquad \nabla \cdot \boldsymbol{E} = \frac{\rho_e}{\epsilon_0} \tag{2.4}$$

$$\text{Solenoidal nature of magnetic field} \qquad \nabla \cdot \boldsymbol{B} = 0 \tag{2.5}$$

$$\text{Faraday's law in differential form} \qquad \nabla \times \boldsymbol{E} = -\frac{\partial \boldsymbol{B}}{\partial t} \tag{2.6}$$

$$\text{Ampère-Maxwell equation} \qquad \nabla \times \boldsymbol{B} = \mu_0 \boldsymbol{J} + \mu_0 \epsilon_0 \frac{\partial \boldsymbol{E}}{\partial t}. \tag{2.7}$$

In these equations, ϵ_0 is the electric constant (also called the permittivity of free space), μ_0 is the magnetic constant (also called the permeability of free space), σ is the electrical conductivity, treated here as a constant, q is the charge, ρ_e is the charge density, m is the mass, $\boldsymbol{J}$ is the electric current density, and $\boldsymbol{E}$ and $\boldsymbol{B}$ are the electric and magnetic fields. The MHD electrodynamic equations are simplified from the Maxwell's equations (2.4)–(2.7), charge conservation (2.8), Ohm's law (2.9) and Lorentz force (2.10)

$$\text{charge conservation} \qquad \nabla \cdot \boldsymbol{J} = -\frac{\partial \rho_e}{\partial t} \tag{2.8}$$

$$\text{Ohm's law} \qquad \boldsymbol{J} = \sigma \left(\boldsymbol{E} + \boldsymbol{u} \times \boldsymbol{B} \right) \tag{2.9}$$

$$\text{Lorentz force} \qquad \boldsymbol{F}_L = q \left(\boldsymbol{E} + \boldsymbol{u} \times \boldsymbol{B} \right), \tag{2.10}$$

where q is the charge. In MHD, the charge density ρ_e is immaterial. It is assumed that any positive and negative charges are equilibrated on the time scale related to the speed of light, i.e. practically immediately in comparison to the typical time scale of the flow. The electric force $q\boldsymbol{E}$ is also minute compared to the other component of the Lorentz force. Thus, the Guass's law is dropped and the charge conservation equation (2.8) is reduced to (2.11). Also, in MHD, displacement currents are negligible compared to the current density $\boldsymbol{J}$, thus $Ampère's$-Maxwell equation (2.7) reduces to equation (2.12). The MHD equations become (2.11)-(2.16). Detailed derivation can be found in many textbooks, including [18]

and [43].

$$\nabla \cdot \boldsymbol{J} = 0 \tag{2.11}$$

$$\nabla \times \boldsymbol{B} = \mu_0 \boldsymbol{J} \tag{2.12}$$

$$\nabla \times \boldsymbol{E} = -\frac{\partial \boldsymbol{B}}{\partial t} \tag{2.13}$$

$$\nabla \cdot \boldsymbol{B} = 0 \tag{2.14}$$

$$\boldsymbol{J} = \sigma \left(\boldsymbol{E} + \boldsymbol{u} \times \boldsymbol{B} \right) \tag{2.15}$$

$$\boldsymbol{F}_L = \boldsymbol{j} \times \boldsymbol{B} \tag{2.16}$$

2.1.2 MHD approximations for liquid metal flows in blankets

A. Quasi-static Approximation

We consider the situation when a steady magnetic field $\boldsymbol{B}_0$ is imposed in the flow domain. The electric currents induced in the flow $\boldsymbol{j}_0 \sim \sigma \boldsymbol{u} \times \boldsymbol{B}_0$ generate additional magnetic field $\boldsymbol{b}$. The total field written as $\boldsymbol{B} = \boldsymbol{B}_0 + \boldsymbol{b}$ satisfy the MHD equations presented in section 2.1.1. It can be derived theoretically (see, e.g. [18]) and verified experimentally and numerically that in the laboratory and industrial flows of liquid metals, the model can be simplified using the quasi-static approximation.

To start the explanation of this approximation, two important parameters used in MHD should be defined. The magnetic Reynolds number is

$$R_m = ul/\lambda = \mu\sigma ul, \tag{2.17}$$

which is the ratio of advection to diffusion of magnetic field. U and L are the typical velocity and length scales of the flow. The magnetic Prandtl number is

$$Pr_m = \nu/\lambda. \tag{2.18}$$

where ν is the kinematic viscosity of the fluid and $\lambda = 1/(\sigma\mu_0)$ is the magnetic diffusivity. σ and μ_0 are the electric conductivity of the fluid and magnetic permittivity of vacuum. For almost all technological flows of liquid metals, including the flows in the liquid metal blankets of fusion reactors, the magnetic Reynolds number and magnetic Prandtl number are both small

$$R_m \ll 1 \tag{2.19}$$

$$Pr_m \ll 1. \tag{2.20}$$

In such conditions, the magnetic field $\boldsymbol{b}$ associated with induced currents, $\boldsymbol{j}_0 \sim \sigma \boldsymbol{u} \times \boldsymbol{B}_0$, is negligible compared to the imposed magnetic field $\boldsymbol{B}_0$. Furthermore, it can be assumed, as an accurate approximation, that $\boldsymbol{b}$ adjusts instantaneously to changes of the flow velocity. Thus, under the quasi-static approximation, diffusion of the magnetic field dominates its advection, and the two-way coupling between the fluid motion and the magnetic field is reduced to the one-way effect of the magnetic field on the flow. The Lorentz force and Ohm's law are reduced as:

$$\boldsymbol{F}_L = \boldsymbol{j} \times (\boldsymbol{B_0} + \boldsymbol{b}) \approx \boldsymbol{j} \times \boldsymbol{B_0}, \tag{2.21}$$

$$\boldsymbol{J} \approx \sigma(\boldsymbol{E}_0 + \boldsymbol{u} \times \boldsymbol{B}_0). \tag{2.22}$$

Here, $\boldsymbol{B}_0$ is the imposed steady magnetic field, and, as the magnetic field fluctuations $\boldsymbol{b}$ is ignored from now on, we use $\boldsymbol{B}$ to represent the imposed, steady magnetic field. Though in a real fusion reactor, the magnetic field is not that uniform and steady, it would be more convenient and sufficient for our purposes to use this approximation. The electric field E_0 is irrotational (see (2.13)) and can be represented by $-\nabla\phi$, where ϕ is the electric potential. Combining with conservation of current equation $\boldsymbol{\nabla \cdot J} = 0$, the current $\boldsymbol{J}$ can be uniquely

determined as

$$\boldsymbol{J} = \sigma(-\nabla\phi + \boldsymbol{u} \times \boldsymbol{B}), \tag{2.23}$$

with the potential ϕ being the solution of the Poisson equation:

$$\nabla^2\phi = \nabla \cdot (\boldsymbol{u} \times \boldsymbol{B}). \tag{2.24}$$

B. Boussinesq approximation

It is conventional to use the Boussinesq approximation when dealing with natural convection. According to this approximation, the density variations are very small in comparison to the average density so that we treat the flow as incompressible with constant density ρ, except for the buoyancy force term $\rho\beta T\boldsymbol{g}$ entering the Navier-Stokes equation. Here β is the expansion coefficient. The validity of the Boussinesq approximation depends on the magnitude of temperature variations (see [44] for a discussion). Variations of temperature in the blankets of fusion reactors can be quite large, so one can question the applicability of the Boussinesq approximation. We rely on the previous blanket related studies [45, 46, 22] where the approximation is used, and it is suggested that non-Boussinesq effects can be quantitatively significant but unlikely to affect the flow qualitatively [47]. We choose to adopt the approximation, and postpone ultimate analysis of its validity for the future.

2.2 Flow configuration and governing equations

2.2.1 Flow configuration

A blanket consists of a network of duct segments with liquid metal flowing inside. Currently pursued shapes of the ducts are usually of square cross-section. The configurations considered in this dissertation are always long ducts of square cross-section. For dimensional estimates, we use the typical size of the ducts used in modern blanket designs: width $\sim 20\,cm$ and length $\sim 2\,m$. We consider a flow in a duct with volumetric heating

and imposed strong magnetic field. The specific configurations will be explained in the beginning of the respective chapters. The main attention is given to the toroidal blanket concept, where horizontal ducts oriented along the main component of the magnetic field are considered. The imposed magnetic field is very strong (4 - 12 T), uniform and steady. For simplicity, the duct we consider is always located around the middle of the blanket. That is, in the coordinate system illustrated in Fig. 2.1, the toroidal direction perfectly corresponds to the x-axis (axial direction), while poloidal direction corresponds to y-axis (vertical direction). For the rest of the dissertation, the toroidal and axial or poloidal and vertical refer the same direction. The internal heating by absorbed neutrons is modeled by a volumetric internal heat source concentrated near the first wall ($y = -1$) and decreasing with the distance to this wall (see [48]). The general three-dimensional duct configuration and the heat flux distribution are shown in Fig. 2.1.

Besides the duct configurations of the toroidal concept blanket, in Chapter VI, we discuss the results obtained for a downward flow in a vertical duct. It is a configuration related to the currently popular poloidal blanket concept. The main magnetic field is perpendicular to the flow direction. Under the assumption that the magnetic field is strong enough to make the flow quasi-two-dimensional, it is common to study this configuration using the two-dimensional model proposed in [49]. Thus, the governing equations and numerical method are quite different from those of the toroidal duct flow, and will be discussed in details in Chapter VI. Here we only introduce the general governing equations used in Chapters III-V for the analysis of flows in toroidal blanket configurations.

2.2.2 Governing equations

Under the assumption of an incompressible and Newtonian fluid, the governing equations consist of conservation of mass, conservation of momentum, conservation of energy and MHD electrodynamic equations. After applying the Quasi-static and Boussinesq ap-

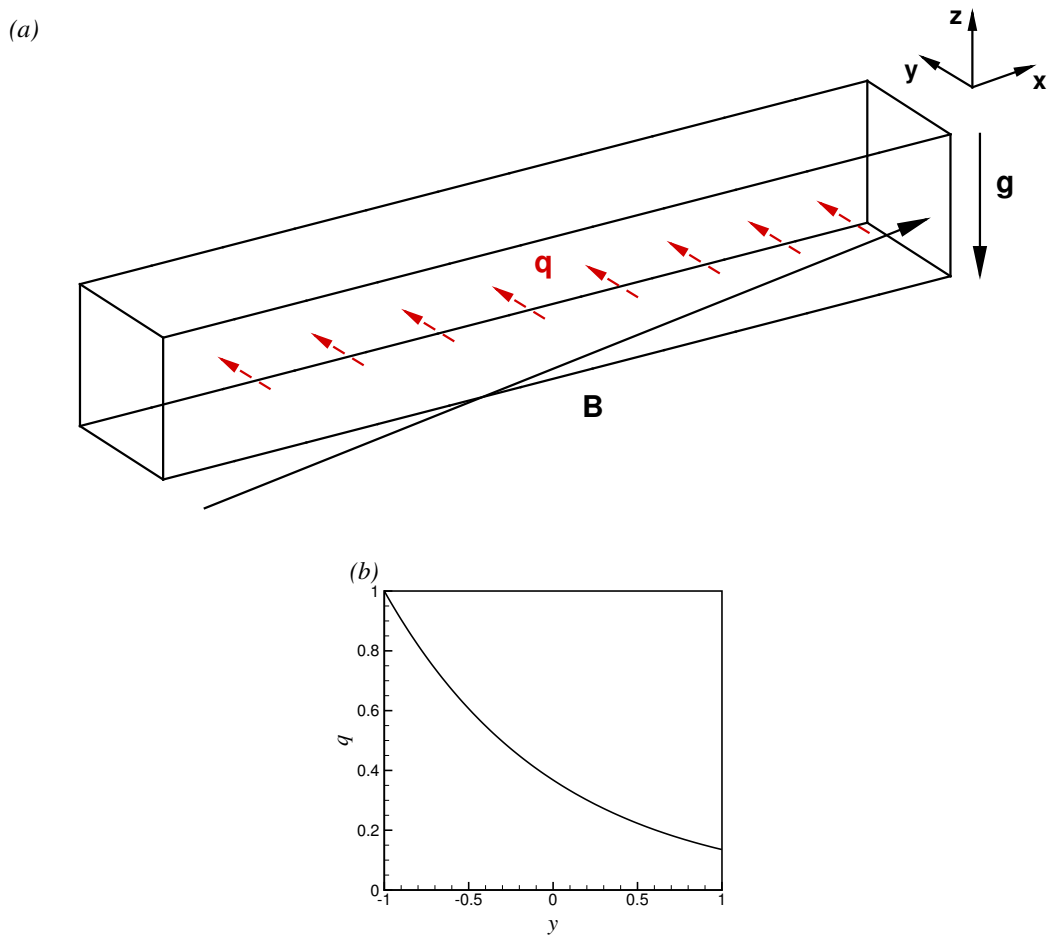

Figure 2.1: Geometry of the flow and coordinate system for 3D simulations *(a)*, and the distribution of the non-dimensional internal heating rate $q(y)$ *(b)*. $\boldsymbol{B}$ is the imposed magnetic field, and $\boldsymbol{g}$ is the gravity acceleration.

proximations in section 2.1.2, the governing equations are as follows:

$$\nabla \cdot \boldsymbol{u} = 0, \tag{2.25}$$

$$\rho \left[\frac{\partial \boldsymbol{u}}{\partial t} + (\boldsymbol{u} \cdot \nabla)\boldsymbol{u} \right] = -\nabla P + \nu \nabla^2 \boldsymbol{u} + \boldsymbol{F}_b + \boldsymbol{F}_L, \tag{2.26}$$

$$\rho c_p \left[\frac{\partial T}{\partial t} + (\boldsymbol{u} \cdot \nabla)T \right] = \kappa \nabla^2 T + Q, \tag{2.27}$$

$$\boldsymbol{F}_b = -\rho g \beta T \boldsymbol{e}_g, \tag{2.28}$$

$$\boldsymbol{F}_L = \boldsymbol{J} \times \boldsymbol{B}, \tag{2.29}$$

$$\boldsymbol{J} = \sigma(-\nabla \phi + \boldsymbol{u} \times \boldsymbol{B}), \tag{2.30}$$

$$\nabla^2 \phi = \nabla \cdot (\boldsymbol{u} \times \boldsymbol{B}). \tag{2.31}$$

$\boldsymbol{F}_b$ and $\boldsymbol{F}_L$ are the buoyancy and Lorentz forces. $\boldsymbol{e}_g$ is the unit vector in the direction of gravity, and T is the temperature perturbation with respect to an appropriate reference value.

To non-dimensionalize the equations, we use the half-width of the duct d as the typical length scale, the imposed magnetic field strength B as the magnetic field scale and q_0 as the typical scale of volumetric internal heating rate. However, in the different problems solved below, different velocity scale and different temperature scale have to be used. In the configurations with the considerable mean-flow velocity, mean-flow velocity U_m is chosen as the velocity scale U. In the configurations with zero mean flow, we use the free fall speed $U = \sqrt{\beta g \Delta T d}$ as the velocity scale. In the configurations with isothermal boundary conditions, $\Delta T = q_0 d^2 \kappa^{-1}$ is used as the scale of temperature deviation from the wall temperature T_0. In the configurations with thermally insulated walls, the scale of temperature is $\Delta T = q_0 d^2 \kappa^{-1}$, where κ is the thermal conductivity. The typical scales for time, pressure, electric potential and electric current density are d/U, ρU^2, dUB, and

σBU, respectively. The general form of the non-dimensional governing equations are:

$$\begin{aligned}
\nabla \cdot \boldsymbol{u} &= 0, && (2.32)\\
\frac{\partial \boldsymbol{u}}{\partial t} + (\boldsymbol{u}\cdot\nabla)\boldsymbol{u} &= -\nabla P + \frac{1}{Re}\nabla^2 \boldsymbol{u} + \boldsymbol{F}_b + \boldsymbol{F}_L, && (2.33)\\
\frac{\partial T}{\partial t} + \boldsymbol{u}\cdot\nabla T &= \frac{1}{Pe}(\nabla^2 T + q), && (2.34)\\
\nabla^2 \phi &= \nabla\cdot(\boldsymbol{u}\times\boldsymbol{e}_b), && (2.35)\\
\boldsymbol{J} &= -\nabla\phi + \boldsymbol{u}\times\boldsymbol{e}_b, && (2.36)\\
\boldsymbol{F}_b &= -\frac{Gr}{Re^2} T \boldsymbol{e}_g, && (2.37)\\
\boldsymbol{F}_L &= \frac{Ha^2}{Re}\boldsymbol{J}\times\boldsymbol{B}. && (2.38)
\end{aligned}$$

Here, $\boldsymbol{u}$ is the velocity field, P is the pressure field and $\boldsymbol{e}_b$ is the non-dimensional magnetic field. The non-dimensional rate of internal heating q due to absorption of neutrons proposed by [48] is approximated as:

$$q(y) = \exp\left[-(y+1)\right] \text{ (see Fig. 2.1b).} \tag{2.39}$$

The non-dimensional parameters are the Reynolds number,

$$Re \equiv \frac{Ud}{\nu}, \tag{2.40}$$

the Prandtl number

$$Pr = \nu/\chi, \tag{2.41}$$

the Peclet number

$$Pe \equiv \frac{Ud}{\chi} = RePr, \tag{2.42}$$

the Hartmann number

$$Ha \equiv Bd\left(\frac{\sigma}{\rho\nu}\right)^{1/2}, \tag{2.43}$$

and the Grashof number

$$Gr \equiv \frac{g\beta q_0 d^5}{\nu^2 \kappa}, \tag{2.44}$$

where, $\chi, \sigma, \nu, \beta, \kappa, \rho$ are the temperature diffusivity, electric conductivity, kinematic viscosity, thermal expansion coefficient, thermal conductivity and density of the fluid.

In the study of thermal convection in MHD flows, there is another parameter which is very important, the Stuart number

$$N \equiv Ha^2 Re^{-1}. \tag{2.45}$$

It represents the relative importance of the Lorentz and inertial forces and can be viewed as a measure of the strength of the effect of the magnetic field on the flow. Large Stuart number means the effects of the Lorentz force is strong and rapid. In most of the cases we studied, the Hartmann number is very large, thus we can assume the velocity field is transformed by the Lorentz force substantially.

The group $GrRe^{-2}$ is yet another important parameter. It measures the relative importance of the forced convection and natural convection.

2.2.3 Boundary conditions

We consider several configurations with different cooling schemes, thus the boundary conditions are different. We always assume that the walls are electrically insulated. The effect of finite electrical conductance of the walls is left for future work.

In a separately cooled blanket, the heat is diverted almost totally by an external cooling system built into the walls. In Chapter III and IV, we model this by setting the wall temperature to a constant value

$$T = 0 \text{ at } y = \pm 1, \ z = \pm 1. \tag{2.46}$$

In the model of a dual-coolant blanket, the radiative heat deposited at the first wall is removed by a built-in coolant system, and the heat associated with the high-speed neutrons captured by the liquid metal is diverted by the liquid metal flow. This configuration is modeled in Chapter V using the approximation of thermally insulated walls

$$\frac{\partial T}{\partial n} = 0 \text{ at } y = \pm 1, \ z = \pm 1. \tag{2.47}$$

In the model of poloidal dual-coolant blanket, we consider the configuration with a downward flow in a vertical duct. For this configuration, we model the experimental design currently tested in some labs where internal heating is hard to accomplish in lab condition. The boundary conditions are those of a constant heat flux at one wall and thermal insulation at the others (see Chapter VI for expressions).

We always use no-slip and electrical insulation conditions at the walls for the velocity and electric potential:

$$\boldsymbol{u} = 0 \text{ at } y = \pm 1, \ z = \pm 1, \tag{2.48}$$

$$\frac{\partial \phi}{\partial n} = 0 \text{ at } y = \pm 1, \ z = \pm 1. \tag{2.49}$$

It should be mentioned that we solve the equations in non-dimensional form but consider the PbLi in a certain temperature range. The physical properties of the PbLi used in the study are shown in table 2.1.

$T[K]$	$\rho[kg/m^3]$	$c_p[J/kg \cdot K]$	$\kappa[W/(m \cdot k)]$	$\sigma[S/m]$	$\nu[m^2/s]$	$\beta[K^{-1}]$
570	10.4×10^3	189.8	13.065	7.90×10^5	2.10×10^{-7}	1.210×10^{-4}
625	9.4×10^3	186.3	14.138	7.76×10^5	1.87×10^{-7}	1.218×10^{-4}

Table 2.1: Physical properties of eutectic alloy Li(17)Pb(83) [6, 7].

The typical values of *Gr*, *Ha* and *Re* studied in the dissertation are in the wide range that includes the values typical for a blanket of a fusion reactor (see table 2.2). It is the first time that the regimes of the flow at the parameters approaching the parameters of a reactor

are addressed.

$q_0[MW/m^3]$	$B[T]$	$U[m/s]$	$d[m]$	*Gr*	*Ha*	*Re*	*Pr*
$0.2-20$	$4-12$	$0.1-2$	$0.05-0.1$	$1.3\times10^8-$ 4.8×10^{11}	$3.8\times10^3-$ 2.5×10^4	$2.4\times10^4-$ 1.1×10^6	$0.023-0.032$

Table 2.2: Physical conditions in a blanket of a fusion reactor and the corresponding non-dimensional parameters.

We note that the suppression of motion (see section 2.2.4) is an important effect in our study. All the extreme and unusual effects present in following chapters only occur because conventional turbulence is suppressed by the magnetic field. If the suppression were absent, the flows would all be strongly turbulent at such *Gr*.

2.2.4 Effects of a magnetic field on a flow of an electrically conducting fluid

The main effect of an imposed magnetic field on a fluid flow can be summarized as three-fold: suppression of motion, development of anisotropy and development of special MHD boundary layers.

The suppression of motion is a result of magnetic damping. The mechanism of magnetic damping is that motion of a conductor across the magnetic field lines induces electrical current and leads to the Joule dissipation, which results in the conversion of the kinetic energy of the motion into the thermal energy. As a result of such damping effect, turbulence and, in general, fluctuations of velocity are suppressed [18]. Laminarization of the flow by the strong magnetic field results in poor mixing and transport properties.

The second effect, the flow anisotropy is due to that the strength of the Joule dissipation is anisotropic. According to the energy balance of a single Fourier mode $\hat{\boldsymbol{u}}(\hat{\boldsymbol{k}},t)$, The Joule dissipation of the currents induced by a single Fourier mode $\hat{\boldsymbol{u}}(\hat{\boldsymbol{k}},t)$ is $\mu(k) = N|\hat{\boldsymbol{u}}(\hat{\boldsymbol{k}},t)|^2\cos^2\alpha$ [50], where α is the angle between the wavenumber vector $\hat{\boldsymbol{k}}$ and the magnetic field $\boldsymbol{B}$. It shows that, the Joule dissipation is maximum for modes with wavenumber vector parallel to the magnetic field and decreases as the angle α increases. Thus the flow becomes anisotropic with much smaller velocity gradient along the field direction

$\left|\partial_{\parallel}\boldsymbol{u}\right| \ll |\partial_{\perp}\boldsymbol{u}|$. In the limit of very strong magnetic field, the flow tends to become two-dimensional with all variables independent of magnetic field's direction.

The third effect is that special MHD boundary layers are formed when the magnetic field is strong. In particular, in flows within ducts with transverse magnetic fields, the balance between the pressure gradient, Lorentz, and viscous forces results in the velocity profiles, which are nearly flat in the core and exhibit sharp boundary layers near the walls. In a rectangular duct with wall-paralleled field, there are two kinds of boundary layers, the Hartmann layers and Shercliff layers. The Hartmann boundary layers form at the walls perpendicular to the magnetic field lines. Their thickness decreases as the Hartmann number increases $\sim d/Ha$. The Shercliff layers develop at the walls parallel to the magnetic field. Their thickness follows $\sim d/\sqrt{Ha}$. Here, d is the duct's half-width and *Ha* is the Hartmann number in (2.43). The Hartmann layers are thin at high *Ha*, thus need to be dealt with very carefully in numerical simulations to ensure enough resolution. The MHD boundary layers lead to the flow resistance much stronger than the resistance in conventional hydraulic flow without magnetic field [see, e.g. 42].

2.2.5 Two-dimensionality and Lorentz force in 2D flows

One thing need to be mentioned is that the suppression of motion (introduced in section 2.2.4) by the magnetic field leads to an important assumption we adopted in Chapters III-V. In a duct with a strong axial magnetic field, velocity fluctuations in the axial direction are suppressed and flow becomes two-dimensional in the sense that all the variables depend on y, z but not on the axial coordinate x (see Fig. 2.1) if the magnetic field is sufficiently strong. However, a two-dimensional flow is unstable in nature, and as we discuss later, there always remains the possibility of three-dimensional instabilities growing in the presence of the magnetic field. Thus in each chapter, after analyzing the flow in the two-dimensional approximation, we present the three-dimensional stability analysis as well.

The discussion of the Lorentz force deserves special attention because in the two-

dimensional model adopted for some of our studies presented in Chapter III-V, the Lorentz force can be simplified or even omitted in the governing equations.

In these models, the flow is assumed to be streamwise uniform (independent of the x-axis), thus we have: $\boldsymbol{u} = \boldsymbol{u}(y,z,t) = (u(y,z,t)\hat{\boldsymbol{i}}, v(y,z,t)\hat{\boldsymbol{j}}, w(y,z,t)\hat{\boldsymbol{k}})$.

1. Purely toroidal (axial) magnetic field

Firstly, we consider the model with purely axial magnetic field $\boldsymbol{B} = B_t\hat{\boldsymbol{i}}$. The electric current follows these rules:

$$\nabla \cdot \boldsymbol{J} = 0 \tag{2.50}$$

$$\boldsymbol{J} = \sigma(-\nabla\phi + \boldsymbol{u} \times \boldsymbol{B}), \tag{2.51}$$

$$\boldsymbol{J}_n = 0, \text{ at } y = \pm 1, \ z = \pm 1, \tag{2.52}$$

where $\boldsymbol{J}_n$ is the wall normal current vanishing at the insulating walls. It is obvious that:

$$\nabla \times \boldsymbol{J} = \sigma(-\nabla \times (\nabla\phi) + \nabla \times (\boldsymbol{u} \times \boldsymbol{B})), \tag{2.53}$$

$$= \sigma \nabla \times (\boldsymbol{u} \times \boldsymbol{B}). \tag{2.54}$$

As we have $\boldsymbol{u} = \boldsymbol{u}(y,z,t)$ and $\partial/\partial x = 0$, $\nabla \times (\boldsymbol{u} \times \boldsymbol{B})$ is then calculated:

$$\nabla \times (\boldsymbol{u} \times \boldsymbol{B}) = B_t \left(\frac{\partial v}{\partial y} + \frac{\partial w}{\partial z} \right) \hat{\boldsymbol{i}}. \tag{2.55}$$

The incompressibility condition $\nabla \cdot \boldsymbol{u} = \partial v/\partial y + \partial w/\partial z = 0$ leads to $\nabla \times (\boldsymbol{u} \times \boldsymbol{B}) = 0$. So, using $\nabla \times \boldsymbol{J} = 0$ together with $\nabla \cdot \boldsymbol{J} = 0$ and boundary condition $\boldsymbol{J}_n = 0$, we get $\boldsymbol{J} = 0$. It means that no current is generated by fluid motion and the axial magnetic field, and thus, Lorentz force is zero. This is true for flows with ($u \neq 0$) or without ($u = 0$) axial mean flow.

2. Both toroidal and poloidal magnetic field

We now consider the model with both toroidal and poloidal magnetic field $\boldsymbol{B} = B_t\hat{\boldsymbol{i}} +$

$B_p\hat{\boldsymbol{k}}$. In the Ohm's law (2.51), the current generated by the fluid motion and total magnetic field can be separated into parts $\boldsymbol{u}\times\boldsymbol{B} = \boldsymbol{u}\times(B_t\hat{\boldsymbol{i}}+B_p\hat{\boldsymbol{k}})$, in which the currents associated with $\boldsymbol{u}\times B_t\hat{\boldsymbol{i}}$ are always zero. The currents associated with the poloidal magnetic field $\boldsymbol{u}\times B_p\hat{\boldsymbol{k}} = vB_p\hat{\boldsymbol{i}}$ are purely toroidal and do not interact with the $B_t\hat{\boldsymbol{i}}$ to generate a Lorentz force:

$$\begin{aligned}\boldsymbol{F}_L = \boldsymbol{J}\times\boldsymbol{B} &= (\boldsymbol{J}_\parallel + \boldsymbol{J}_\perp)\times(B_t\hat{\boldsymbol{i}} + B_p\hat{\boldsymbol{k}}) &(2.56)\\ &= (0 + vB_p\hat{\boldsymbol{i}})\times(B_t\hat{\boldsymbol{i}} + B_p\hat{\boldsymbol{k}}) &(2.57)\\ &= vB_p\hat{\boldsymbol{i}}\times B_p\hat{\boldsymbol{k}}. &(2.58)\end{aligned}$$

The $\boldsymbol{J}_\parallel$ and $\boldsymbol{J}_\perp$ denote the currents associated with the toroidal magnetic field and poloidal magnetic field respectively. Thus, only the poloidal component of the magnetic field generates Lorentz force and should be included in the momentum equation and electric related equations.

If the walls are not electrically insulated, we do not have the electric current to be zero, but can prove that the Lorentz force associated with the toroidal magnetic field is non-active (potential force) with zero curl $\nabla\times\boldsymbol{F}_L = 0$.

2.3 Numerical Method

2.3.1 Three-dimensional solver

The numerical method used in the work presented in Chapter III-V is a version of the finite difference method firstly introduced in [51]. It has been used in many simulations such as [52, 53, 27]. It has been further changed to include the implicit treatment of temperature in [29]. The method was validated using comparison with earlier experimental and computational results in [52, 27, 53] and other recent works. Additional validation was carried out at the beginning of the work. The classical $Rayleigh - Bénard$ convection problem was

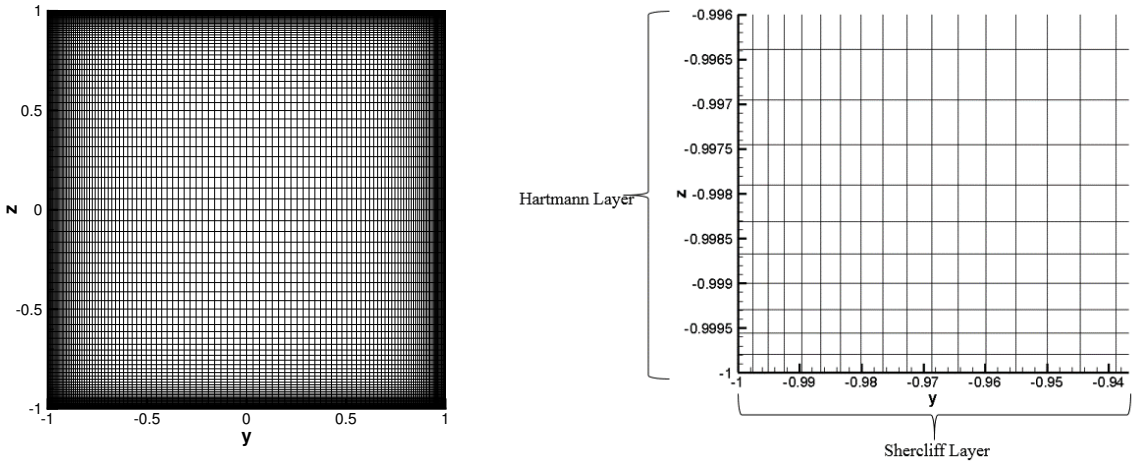

Figure 2.2: Grid used in the simulation of $Ha_p = 250$, $Gr = 10^{10}$ with $N_y = N_z = 128$, $A_y = 2.0$ and $A_z = 3.5$ according to clustering scheme (2.59) (different scales of y and z are used in the zoom-in plot).

solved. The critical Reyleigh numbers agreed well with the data of [54]. The spatial discretization uses central differences on a non-uniform structured collocated grid. It is of the second order of accuracy. As we mentioned early, the MHD boundary need to be resolved well. To save the computational cost, the grid is clustered near the walls. Two clustering schemes are used (see Fig. 2.2-2.3). They are based on the coordinate transformations:

$$y = \frac{\tanh(A_y \eta)}{\tanh(A_y)}, \quad z = \frac{\tanh(A_z \xi)}{\tanh(A_z)}, \tag{2.59}$$

$$y = C_y \sin(\pi\xi/2) + (1 - C_y)\xi, \quad z = C_z \sin(\pi\eta/2) + (1 - C_z)\eta, \tag{2.60}$$

where $-1 \leq \xi \leq 1$ and $-1 \leq \eta \leq 1$ are the transformed coordinates, in which the grid is uniform. The stretching coefficients A_y, A_z are the coefficients determining the degrees of near-wall clustering in (2.59). In (2.60), C_y and C_z are the blending coefficients of the Chebyshev and identity transformations.

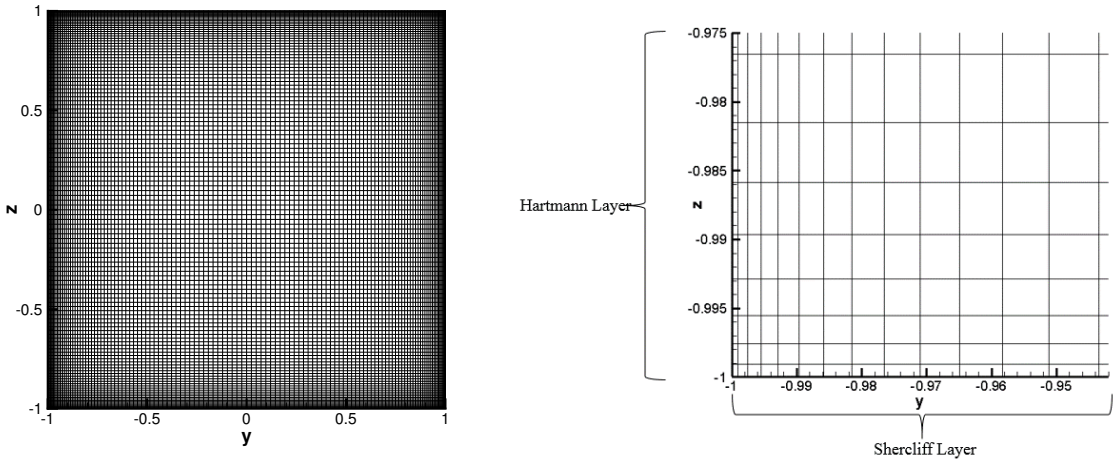

Figure 2.3: Grid used in the simulation of $Ha_p = 40$, $Gr = 10^9$ with $N_y = N_z = 128$ and $C_y = C_z = 0.96$ according to clustering scheme (2.60) (different scales of y and z are used in the zoom-in plot).

Grid sensitivity studies have been conducted to identify proper resolution for different models. The integral properties such as kinetic energy, average mean temperature, Nusselt number are examined to assure that further increase of grid does not lead to change of these properties by more than a few percents. To get accurate time averaging, each simulation has been conducted for a long time and averaged upon enough data. The spatial derivatives are treated as introduced in [55] and [56]. Half-integer grid points are used to calculate the fluxes of velocity and electric currents, which are then used for approximation of derivatives. This results in a highly conservative scheme. In the non-dissipative limit, the mass, momentum, electric charge, and internal energy are conserved exactly by the numerical solution, while the kinetic energy is conserved up to a dissipative error of the 3rd order.

The standard projection algorithm [57] is applied to find pressure and assure incompressibility. The time discretization scheme is of the 2nd order. It is based on the fully explicit Backward Differentiation scheme with Adams-Bashforth extrapolation for the nonlinear terms and body forces. The conduction and viscosity terms are treated implicitly.

The step-by-step description of the procedure from time layer n to n+1 is as follows:

1. Determining body forces: computing the buoyancy force

$$\boldsymbol{F}_b{}^n = -GrRe^{-2}\boldsymbol{e}_g T^n, \tag{2.61}$$

solving the elliptic equation for electric potential

$$\nabla^2\phi^n = \nabla\cdot(\boldsymbol{u}^n\times\boldsymbol{e}_b), \tag{2.62}$$

computing electric current and the Lorentz force

$$\boldsymbol{J} = -\nabla\phi^2 + \boldsymbol{u}^n\times\boldsymbol{e}_b, \tag{2.63}$$

$$\boldsymbol{F}_L{}^n = Ha^2Re^{-1}\boldsymbol{j}_n\times\boldsymbol{e}_b, \tag{2.64}$$

and computing the explicit right hand side

$$\boldsymbol{F}^n = -(\boldsymbol{u}^n\cdot\nabla)\boldsymbol{u}^n + \boldsymbol{F}_b^n + \boldsymbol{F}_L^n. \tag{2.65}$$

2. Determining the intermediate velocity field $\boldsymbol{u}^*$ from:

$$\frac{3\boldsymbol{u}^* - 4\boldsymbol{u}^n + \boldsymbol{u}^{n-1}}{2\Delta t} = 2\boldsymbol{F}^n - \boldsymbol{F}^{n-1} + Re^{-1}\nabla^2\boldsymbol{u}^*. \tag{2.66}$$

In this sub-step, three elliptic equations are solved for the three components of $\boldsymbol{u}^*$.

3. Solving for the pressure fluctuations:

$$\nabla^2 p^{n+1} = \frac{3}{2\Delta t}\nabla\cdot\boldsymbol{u}^*. \tag{2.67}$$

4. Updating the velocity field and to ensure incompressibility:

$$\boldsymbol{u}^{n+1} = -\frac{2}{3}\Delta t\nabla p^{n+1} + \boldsymbol{u}^*. \tag{2.68}$$

5. Solving the elliptic equation for temperature:

$$\frac{3T^{n+1} - 4T^n + T^{n-1}}{2\Delta t} = \frac{1}{Pe}\nabla^2 T^{n+1} + q + 2G^n - G^{n-1}, \tag{2.69}$$

where $G^n = -\nabla \cdot (T^n \boldsymbol{u}^n)$. The implicit treatment of the conduction term is particularly useful, since it allows us to avoid the strong numerical instability limitations on the size of time step when the Prandtl number is small.

The algorithm is parallelized using the hybrid MPI-OpenMP approach. The MPI memory is distributed along the spanwise coordinate direction in the physical space, and along the streamwise coordinate in the Fourier space.

The elliptic equations of potential, pressure, velocities and temperature are solved by using the Fourier decomposition in the streamwise coordinate. The two-dimensional equations for the Fourier components are solved in the transformed coordinates (η-ξ) using the direct cyclic reduction method [see 51]. The subroutines of the library FishPack (see [58]) are utilized for this part of the solution.

2.3.2 Two-dimensional solver

Another code has been developed to study the 2D flow in a vertical duct with transverse magnetic field and more practical inlet-exit boundary condition. The flow is approximated according to the two-dimensional model proposed in [49]. It is a two-dimensional solver.

The governing equations are expressed in ψ-ω formulation and the effect of strong magnetic field is represented by a linear friction term in the momentum equation.

The matrices of the discretized equations of this model are block tridiagonal. The Thomas algorithm (see e.g. [57]) is used in this solver and is parallelized using OpenMP. The main computational costs come from doing inverse of the matrix and multiplication of matrix. With the help of the libraries Lapack and MKL (Math Kernel Library), and by storing the resulting block matrix properly, the solver is able to solve the matrix equations

with high efficiency.

This solver is also adaptable to different kinds of inlet-exit boundary condition as it does not require periodic inlet-exit to use the Fourier transform in axial direction. This allows us to study the vertical duct flow with more practical inlet-exit condition.

CHAPTER III

Separately Cooled Toroidal Blanket

The results presented in this chapter were published in [3]. Flow in a horizontally oriented duct with uniform axial magnetic field and internal heating is analyzed. This configuration is related to the toroidal design concept of the liquid metal blanket, which is a possible alternative to the poloidal design concept troubled by convection-induced high-amplitude low-frequency temperature fluctuations. The configuration considered in this chapter is the first idealized model of the toroidal duct that takes the thermal convection into account. Our goal is to understand its effect and to see if it still leads to detrimental instability and dangerous temperature profile.

The simulations are divided into two parts. In the first half, the magnetic field is assumed to be very strong and, due to the suppression effect, the flow is assumed to be streamwise-uniform and studied as two-dimensional. In the second half, we study the three-dimensional flow in long segments of the duct to test the robustness of our two-dimensionality assumption.

3.1 Configuration

A flow in a horizontal duct aligned with a strong uniform magnetic field is analyzed. The poloidal component of the magnetic field (about 5% of the total field strength) and curvature effects are neglected. A square fairly long duct is considered (see Fig. 3.1a). As

we mentioned in Chapter II, the ducts of a blanket we consider are $\sim$ 1-2 m long. Comparing this to the radius of the Tokamak (inner radius $\sim$ 6.2 m in ITER), we see that the curvature of the duct is negligible. In addition, the effect of the curvature influences the flow not more than the other effects neglected in our study, such as those of realistic inlet-exit condition. Thus we assume that both the duct and the magnetic field are horizontal and straight. Non-uniform volumetric internal heating representing the heat generated by stopping high-speed neutrons is concentrated near the wall $y = -1$ and distributed according to (2.39). The walls are assumed to be maintained at constant temperature with all the deposited heat diverted by an auxiliary coolant system (e.g. pressurized He) built into the walls. Mean flow is assumed zero as it is an idealized model of a separately cooled blanket in which the mean flow would be negligibly slow ($\sim$ 1 mm/s or less).

As the main component of the magnetic field corresponding to fusion reactor condition is very strong, the flow variations in the axial direction are assumed to be negligible due to the suppression by the magnetic field. The effects of the duct's ends are neglected. Under these assumptions, the computational domain for two-dimensional simulations is a square as shown in Fig. 3.1b.

In the stability analysis, three-dimensional flows in 3D domain shown in Fig. 3.1a are studied.

3.2 Governing Equations and Boundary Conditions

We use the set of governing equations (2.32)-(2.38) introduced in Chapter II, section 2.2.2. The temperature deviation from the wall temperature $\Delta T = q_0 d^2 \kappa^{-1}$ is used as the temperature scale. There is no mean flow in this model, thus the free-fall speed

$$U = \sqrt{\beta g \Delta T d} \tag{3.1}$$

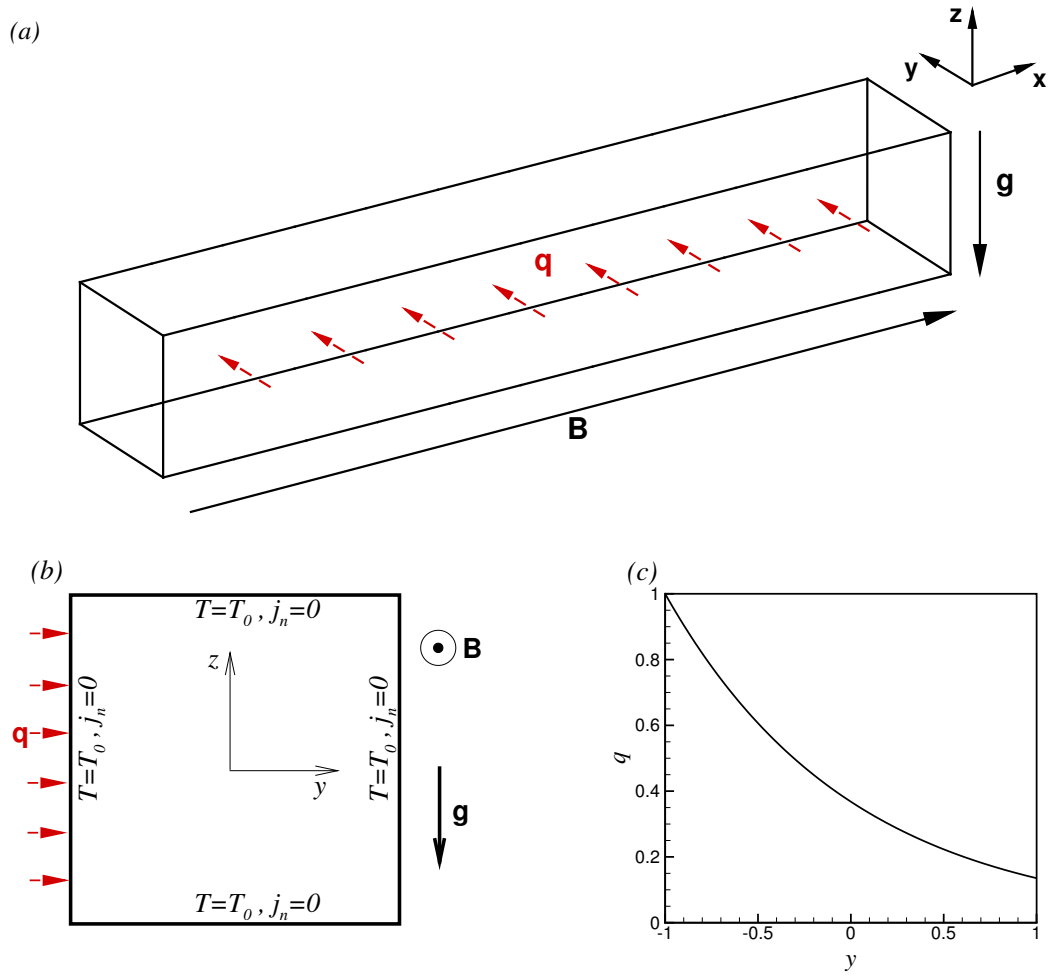

Figure 3.1: Geometry of the flow and coordinate system for 3D simulations *(a)*, 2D simulations *(b)*, and the distribution of the non-dimensional internal heating rate $q(y)$ *(c)*.

is used as the velocity scale. The non-dimensional governing equations are:

$$\frac{\partial \boldsymbol{u}}{\partial t} + (\boldsymbol{u} \cdot \nabla)\boldsymbol{u} = -\nabla p + \frac{1}{\sqrt{Gr}}\nabla^2 \boldsymbol{u} + T\boldsymbol{e}_z + \boldsymbol{F}_L, \tag{3.2}$$

$$\nabla \cdot \boldsymbol{u} = 0, \tag{3.3}$$

$$\frac{\partial T}{\partial t} + \boldsymbol{u} \cdot \nabla T = \frac{1}{Pr\sqrt{Gr}} \left(\nabla^2 T + q\right), \tag{3.4}$$

$$\boldsymbol{u} = T = 0 \text{ at } y = \pm 1,\ z = \pm 1, \tag{3.5}$$

where $\boldsymbol{u} = (u_x, u_y, u_z)$ and T are the non-dimensional velocity and temperature deviation from T_0. The distribution of non-dimensional rate of internal heating q is (2.39).

As discussed in Chapter II, section 2.2.5, the Lorentz force is zero in a duct with with insulated walls and purely axial magnetic field if the flow is two-dimensional.

In three-dimensional flows, electric currents and Lorentz force are computed by:

$$\nabla^2 \phi = \nabla \cdot (\boldsymbol{u} \times \boldsymbol{e}_x), \tag{3.6}$$

$$\boldsymbol{j} = -\nabla \phi + \boldsymbol{u} \times \boldsymbol{e}_x, \tag{3.7}$$

$$\boldsymbol{F}_L = Ha^2 Re^{-1} \boldsymbol{j} \times \boldsymbol{e}_x. \tag{3.8}$$

The walls are electrically insulated

$$\frac{\partial \phi}{\partial n} = 0 \text{ at } y = \pm 1,\ \ z = \pm 1. \tag{3.9}$$

In three-dimensional flows, periodicity of the electric potential ϕ, velocity $\boldsymbol{u}$, temperature fluctuations T and pressure p at $x = 0, L$ (L is the length of the duct) is assumed. The non-dimensional parameters are the Grashof, Prandtl, and Hartmann numbers defined in Chapter II (see (2.44),(2.41),(2.43)). The use of the free-fall speed as the velocity scale U (see (3.1)) implies that the Reynolds number is $Re = Gr^{1/2}$.

3.3 Parameters and Grid

Simulations are conducted at $10^6 \leq Gr \leq 10^{11}$, $Pr = 0.0321$ (PbLi alloy at about 570 K) and $800 \leq Ha \leq 10^4$. They refer to the typical values corresponding to fusion reactors conditions [42]: *Gr* up to 10^{12} and *Ha* up to 10^4. The axial length of the computational domain in three-dimensional simulations is $4\pi \leq L \leq 30\pi$. The following integral characteristics of the flow are computed. The Nusselt number is defined as

$$Nu = \frac{Q}{\overline{T}}, \tag{3.10}$$

where $Q = \int_A q dA$ is the total heating rate and $\overline{T} = A^{-1} \int_A T dA$ is the averaged mean temperature. We also compute the kinetic energy, enstrophy, and angular momentum with respect to the centre of the duct

$$E = \frac{1}{A} \int_A (|u_x|^2 + |u_y|^2) dA, \tag{3.11}$$

$$\Omega = \frac{1}{2A} \int_A \omega^2 dA, \tag{3.12}$$

$$\mathcal{L} = \frac{1}{A} \int_A (y u_z - z u_y) dA = -\frac{1}{A} \int_A r^2 \omega dA. \tag{3.13}$$

A discussion of the detailed meaning of these properties can be found in [59]. For the purpose of code verification, the total vorticity is computed:

$$\omega = \frac{\partial u_z}{\partial y} - \frac{\partial u_y}{\partial z}, \tag{3.14}$$

$$W = \int_A \omega dA. \tag{3.15}$$

The direct integration of ω with velocity boundary conditions shows that W should be zero for all flows.

The problem is solved numerically using the finite difference method described in sec-

tion 2.3. Since the magnetic field is in the axial direction, no Hartmann or Shercliff layers are formed at the duct walls and thus the requirement on the clustering of the grid is not stringent, not more so than for conventional thermal convection flow in a box. We use the second clustering scheme (2.60) with the blending coefficients $C_y = C_z = 0.96$. The grid is uniform in the axial direction (in three-dimensional computations).

The results of grid sensitivity study at $10^6 \le Gr \le 10^{11}$ are shown in table 3.1. For every *Gr*, further increase of the grid size above the chosen grid does not significantly affect the integral properties of the flow. The total vorticity W obtained by Simpson-rule integration of ω is sufficiently close to zero.

Gr	N_y	N_z	*Nu*	W	E	Ω	$\mathcal{L}$
10^6	32	32	35.4	6.41×10^{-2}	6.62×10^{-2}	4.33	-3.45×10^{-1}
10^6	64	64	35.3	6.74×10^{-2}	6.74×10^{-2}	4.20	-3.46×10^{-1}
10^6	96	96	35.3	1.07×10^{-3}	6.74×10^{-3}	4.18	-3.45×10^{-1}
10^7	64	64	44.9	4.28×10^{-3}	4.25×10^{-2}	5.20	-2.10×10^{-1}
10^7	96	96	45.2	1.6×10^{-3}	4.27×10^{-2}	5.12	-2.11×10^{-1}
10^7	128	128	44.9	1.02×10^{-3}	4.29×10^{-2}	5.13	-2.14×10^{-1}
10^8	96	96	56.1	1.57×10^{-3}	1.52×10^{-2}	4.60	-1.58×10^{-1}
10^8	128	128	56.1	7.4×10^{-4}	1.62×10^{-2}	4.64	-1.67×10^{-1}
10^8	256	256	55.9	5.18×10^{-5}	1.63×10^{-2}	4.61	-1.69×10^{-1}
10^9	128	128	81.5	7.04×10^{-4}	7.99×10^{-3}	4.91	-8.67×10^{-2}
10^9	256	256	81.6	2.00×10^{-4}	8.48×10^{-3}	4.93	-9.63×10^{-2}
10^9	512	512	81.2	3.78×10^{-5}	8.50×10^{-3}	4.93	-9.17×10^{-2}
10^{10}	128	128	126.2	2.32×10^{-3}	4.86×10^{-3}	4.77	-5.51×10^{-2}
10^{10}	256	256	126.5	4.58×10^{-4}	5.64×10^{-3}	4.97	-5.65×10^{-2}
10^{10}	512	512	128.1	7.4×10^{-5}	5.50×10^{-3}	4.78	-5.90×10^{-2}
10^{11}	256	256	204.6	6.21×10^{-4}	2.77×10^{-3}	4.26	-3.37×10^{-2}
10^{11}	512	512	206.0	3.11×10^{-4}	3.14×10^{-3}	4.49	-3.65×10^{-2}
10^{11}	1024	1024	206.6	2.6×10^{-5}	3.03×10^{-3}	4.39	3.80×10^{-2}

Table 3.1: Grid sensitivity study. Parameters of computational grids and integral characteristics of two-dimensional solutions are shown. The characteristics are obtained by time-averaging at $Gr \ge 10^7$. The grids used in simulations of two-dimensional flows are underlined [3].

In three-dimensional analysis, we keep the axial grid step Δx less than 0.1. The typical wavelength of the unstable modes observed in section 3.4.2 is about 100 times larger than the grid step, thus the resolution in axial direction is reasonable.

3.4 Results

3.4.1 Two-dimensional flows

We performed two-dimensional simulations at $10^6 \leq Gr \leq 10^{11}$. Significant convection structures caused by internal heating are found in all of them. Flows vary from steady state, to oscillating, and to turbulent as Gr increases. Typical distributions of streamfunction, temperature and magnitude of vertical velocity at $Gr = 10^6$, $Gr = 10^8$ and $Gr = 10^{11}$ are shown in Fig. 3.2. The integral properties at different Gr are shown in table 3.1, and in Figs. 3.3-3.5.

Firstly, we look at the flow at low Grashof number $Gr = 10^6$ (see Fig. 3.2a-c). The flow is steady state. The internal heating causes two big convection rolls. These convection structures occupy the whole domain, and the temperature is higher in the core than near the walls.

As Gr increases, for example at $Gr = 10^7$ or $Gr = 10^8$ (see Fig. 3.2d-f), the flow becomes oscillating. The convection structures are similar to those in the case of $Gr = 10^6$, but the convection rolls are stronger and have stronger shear near the walls. Thus the heat transfer is more effective than at $Gr = 10^6$ and the resulting temperature field is more uniform. The 'hot zone' is not only in the up center as shown in Fig. 3.2b, but penetrates closer to the walls. The vertical velocity field indicates strong jets at the walls, which are beneficial for diverting heat into walls (see Fig. 3.2f). The energy spectra from the Fourier analysis of the time signal of kinetic energy $E(t)$ show that flow is periodic at $Gr = 10^7$ with three dominant frequencies, and becomes irregular at $Gr = 10^8$ with one dominant frequency and weaker frequencies distributed continuously over a small interval (see Figs. 3.4a,b).

At high Grashof numbers $10^9 \leq Gr \leq 10^{11}$, which are more relevant to the blanket operation and more interesting for us, the flows are found to be turbulent. The flow structures are observed to be similar to the forced two-dimensional turbulence as described by

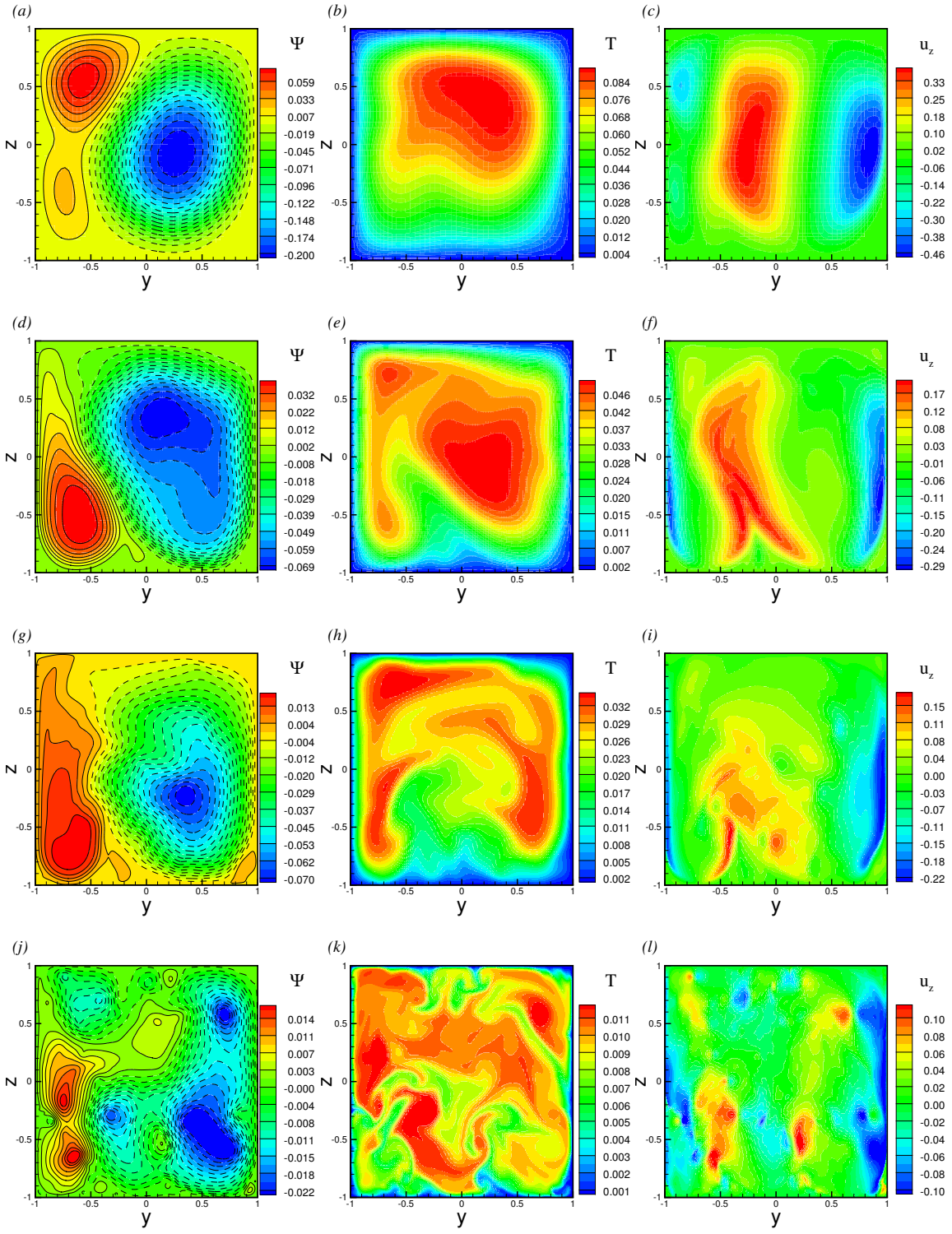

Figure 3.2: Instantaneous distributions of streamfunction Ψ (solid lines indicate counter-clockwise motion, while dashed lines indicate clockwise motion), temperature T and amplitude of vertical velocity u_z in two-dimensional flows at $Gr = 10^6$ *(a)-(c)*, $Gr = 10^8$ *(d)-(f)*, $Gr = 10^9$ *(g)-(i)*, $Gr = 10^{11}$ *(j)-(l)*. Note that the isolevels are different at different *Gr*.

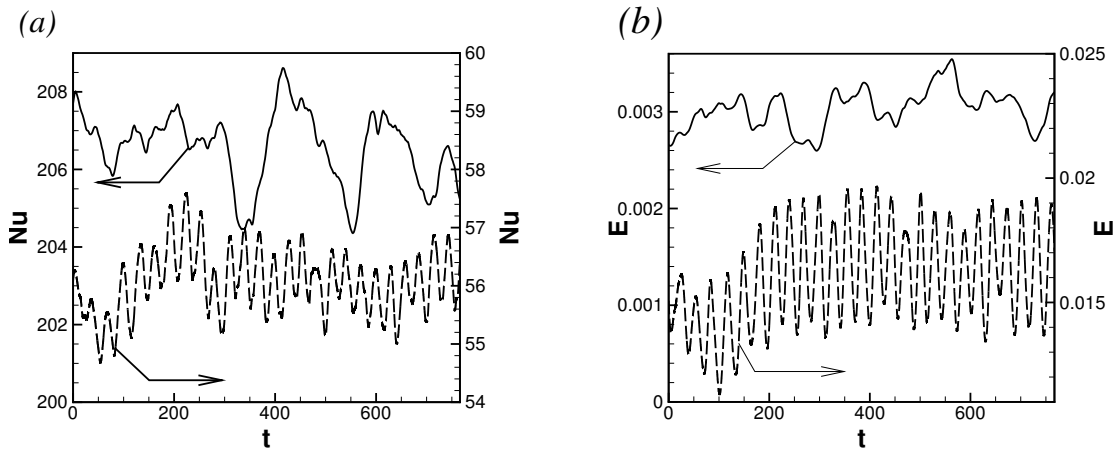

Figure 3.3: Nusselt number *(a)* and total kinetic energy *(b)* in two-dimensional flows at $Gr = 10^8$ (dashed lines) and $Gr = 10^{11}$ (solid lines). Only parts of actual simulations are shown. Note that different scales are used at $Gr = 10^8$ and $Gr = 10^{11}$ [3].

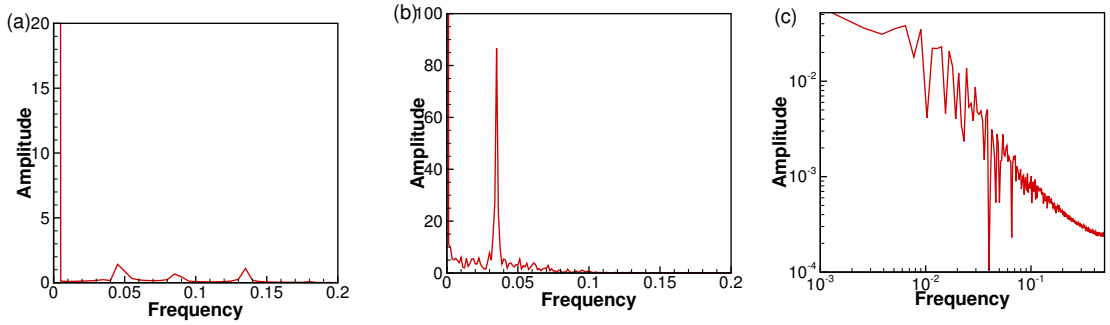

Figure 3.4: Spectral decompositions of total kinetic energy signal $E(t)$ in two-dimensional flows at $Gr = 10^7$ *(a)*, $Gr = 10^8$ *(b)*, $Gr = 10^{11}$ *(c)* (in log-scale) [3].

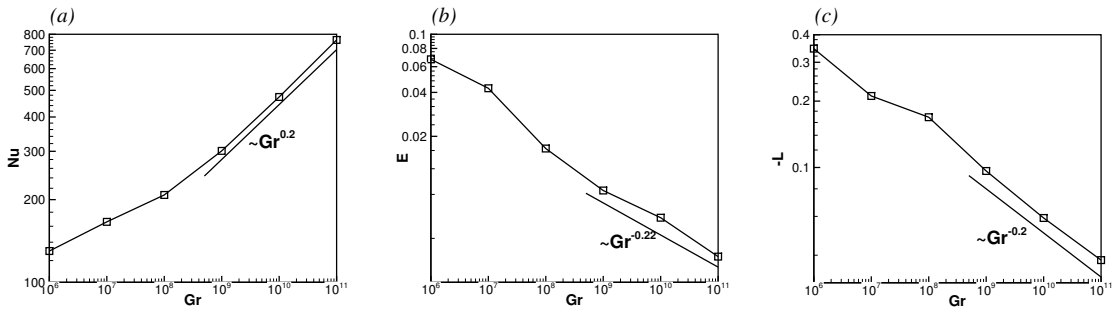

Figure 3.5: Integral time-averaged (at $Gr \geq 10^7$) characteristics of the 2D flows listed in table 3.1. Approximate slopes at $10^9 \leq Gr \leq 10^{11}$ are indicated [3].

[59]: continuous instability and breakdown of large-scale structures, and their recreation by forcing (see Fig. 3.2g-l). There are thin shear layers and vorticity filaments forming at the walls. The turbulent behavior can be verified by the Fourier analysis of the energy signal (see Fig. 3.4c). The spectrum shows wide ranges of active frequencies typical for two-dimensional turbulence. The inverse energy cascade is not observed in our simulations, as the convection forcing acts on the length scale similar to the size of the flow domain.

The integral properties *Nu* and E change as *Gr* increases. At higher *Gr*, *Nu* increases significantly due to stronger mixing by convection. We actually found that the flow follows a scaling law in the turbulent regime at $Gr \geq 10^9$. As shown in Fig. 3.5, the Nusselt number grows as

$$Nu \sim Gr^{0.2}. \tag{3.16}$$

A similar scaling was observed in simulations of two-dimensional convection in a horizontal layer with uniform internal heating by [60]. The total kinetic energy and the amplitude of total angular momentum $-L$ decrease due to the redistribution of kinetic energy from large to small length scales. The data in Fig. 3.5 suggest the scaling

$$E \sim Gr^{-0.22}, \tag{3.17}$$

$$\mathcal{L} \sim Gr^{-0.2}. \tag{3.18}$$

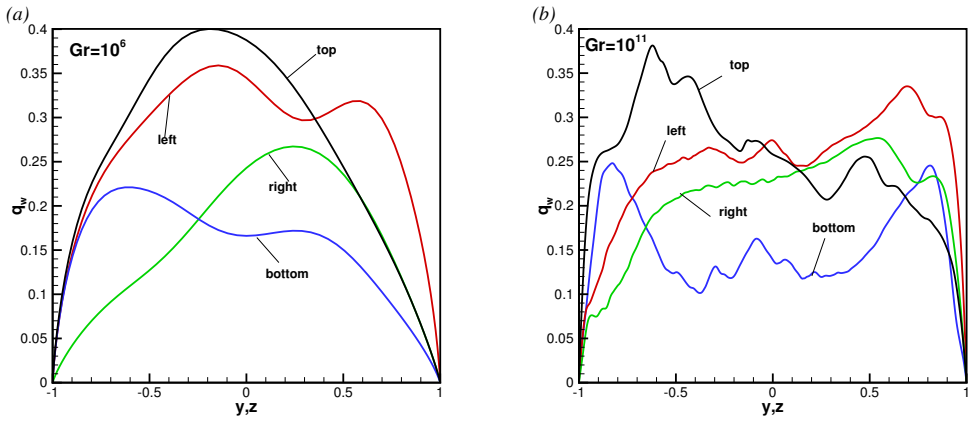

Figure 3.6: Distributions of wall heat flux at $Gr = 10^6$ and $Gr = 10^{11}$.

The total angular momentum is always negtive $\mathcal{L} < 0$, which reflects the asymmetry introduced by the forcing.

As the configuration we studied is related to a separately cooled blanket with external heat exchanger built into walls, it is important to know how the heat flux from the interior is distributed over the walls. The non-dimensional heat flux is computed as

$$q_w = -\left.\frac{dT}{dn}\right|_{\text{wall}}, \tag{3.19}$$

where $\boldsymbol{n}$ refers wall-normal direction. The heat flux distributions to the four walls at $Gr = 10^6$ and $Gr = 10^{11}$ are taken as examples and shown in Fig 3.6. At low Grashof number $Gr = 10^6$, we have more heat flux diverted into the left and top walls. The flow structure consists of large convection rolls, and these convection structures provide some mixing effect. But as we can see, the heat flux distribution varies from wall to wall, and not quite sufficient. The flow at $Gr = 10^8$ has a similar heat flux distribution.

The heat flux distribution at $Gr = 10^{11}$ is different from the low-Gr cases. The curves in Fig. 3.6 indicate that the heat flux varies less along each wall. Comparing between the walls, we see these lines are closer to each other in Fig. 3.6b than in Fig. 3.6a. Thus the heat flux distribution between walls is more uniform at high Gr. It indicates that the turbulent

regime at high *Gr* proves more effective in providing sufficient heat transfer between the interior of the flow and the external heat exchanger in the walls, which is beneficial to the operation of blanket.

3.4.2 Stability Analysis

We did 3D stability analysis by adding small-amplitude random 3D perturbations to the 2D solutions and computing the flow evolution for long periods of time to see if the transition to 3D states occured or not. The flows are computed with periodic inlet-exit conditions.

The perturbations with respect to the two-dimensional solutions are computed as:

$$\boldsymbol{u}' = \boldsymbol{u} - \overline{\boldsymbol{u}}, \quad T' = T - \overline{T} \tag{3.20}$$

where $\overline{\boldsymbol{u}}$ and $\overline{T}$ are the instantaneous averages in the axial direction. The perturbation energies are computed as:

$$E' = \langle f'^2 \rangle, \tag{3.21}$$

where $\langle \ldots \rangle$ stands for volume averaging, and f' stands for perturbations of a velocity component or temperature. If perturbation energies continuously grow and saturate at a considerable amplitude (see Fig. 3.7a), the 2D flow is considered unstable to the 3D perturbations. If perturbation energies exponentially decrease (see Fig. 3.7b), the flow is considered stable to 3D perturbations.

Duct length L is an important parameter as it determines the maximum axial wavelength λ_x of the perturbations. The suppression (Joule dissipation) strength of the magnetic field is proportional to $Ha^2 Re^{-1} \lambda_x^{-2}$, thus at any strength of the magnetic field, one can select a sufficiently long domain such that perturbations with $\lambda_x \sim L$ survive the suppression. Our tests cover the duct lengths up to 30π, which is long enough to consider all the possible perturbations that can develop in a typical duct of a blanket with few cm width and not

Gr	*Ha*	L_z	N_x	N_y	N_z	E'	E'/E_{2D}
10^9	500	4π	64	64	96	3.5×10^{-4}	4.4%
10^9	800	4π	64	64	96	5.0×10^{-5}	0.6%
10^9	900	4π	64	64	96	1.0×10^{-6}	0.01%
10^9	1000	4π	64	64	96	stable	stable
10^9	1050	10π	64	64	256	2.4×10^{-4}	3.0%
10^9	1500	10π	64	64	256	8.0×10^{-5}	1.0%
10^9	1700	10π	64	64	256	2.5×10^{-6}	0.03%
10^9	1750	10π	64	64	256	stable	stable
10^9	2000	20π	64	64	512	3.5×10^{-4}	4.4%
10^9	2500	20π	64	64	512	2.0×10^{-8}	0.0003%
10^9	2700	20π	64	64	512	stable	stable
10^9	3700	30π	64	64	1024	6.0×10^{-8}	0.0008%
10^9	4000	30π	64	64	1024	stable	stable
10^{10}	2000	10π	128	128	256	3.0×10^{-4}	6.0%
10^{10}	4000	10π	128	128	256	8.0×10^{-5}	1.6%
10^{11}	10^4	4π	256	256	96	3.0×10^{-6}	0.1%
10^{11}	2×10^4	4π	256	256	96	stable	stable
10^{11}	10^4	10π	256	256	256	6.0×10^{-5}	2.0%

Table 3.2: Results of three-dimensional simulations. Computational parameters, energy of three-dimensional perturbations E' (for unstable cases), and the ratio between E' and the kinetic energy of the corresponding two-dimensional flows E_{2D} are shown.

longer than 2 m. The most extensive computations are conducted at $Gr = 10^9$, while at $Gr = 10^{10}$, $Gr = 10^{11}$ only some runs were performed to confirm that the situation is similar. Though only very high *Gr* cases are related to the blanket application, we also did some simulations at low Grashof numbers.

To make three-dimensional computations feasible, we reduce the size of the computational grid in the y-z-plane in 3D simulations (see tables 3.1 and 3.2).

The main results at $Gr = 10^9$ are summarized in Fig. 3.8. For a certain length of duct L, there is a critical Hartmann number Ha_{cr} above which the perturbations would be suppressed and the flow maintains two-dimensionality. If *Ha* is smaller than Ha_{cr}, transition to three-dimensionality occurs. Flow becomes less stable as *Gr* increases, which is indicated by Ha_{cr} growing with *Gr*. Also, for a flow at a certain *Gr*, the Ha_{cr} increases if the length of the duct L increases (see Fig. 3.8). So, the stability requires either larger *Ha*

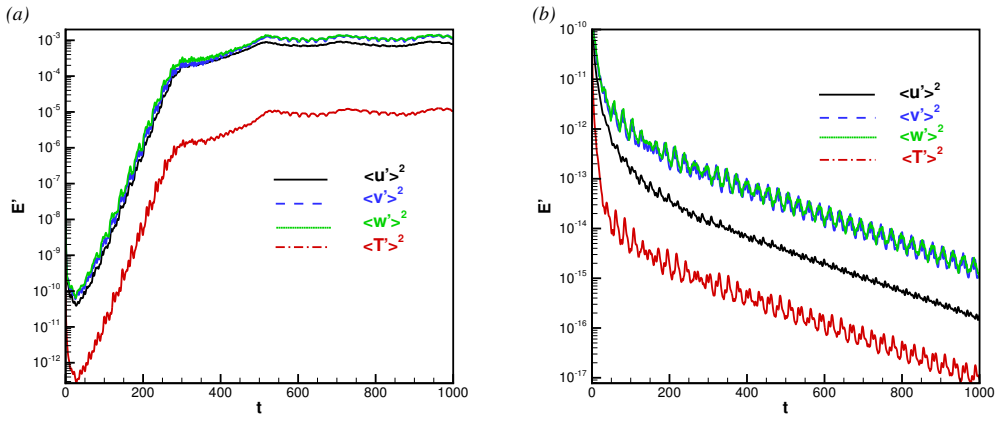

Figure 3.7: Evolution of three-dimensional perturbation energy E' for the unstable flow at $Ha = 80$, $Gr = 10^7$, $L = 4\pi$ *(a)* and the stable flow at $Ha = 100$, $Gr = 10^7$, L=4π *(b)*.

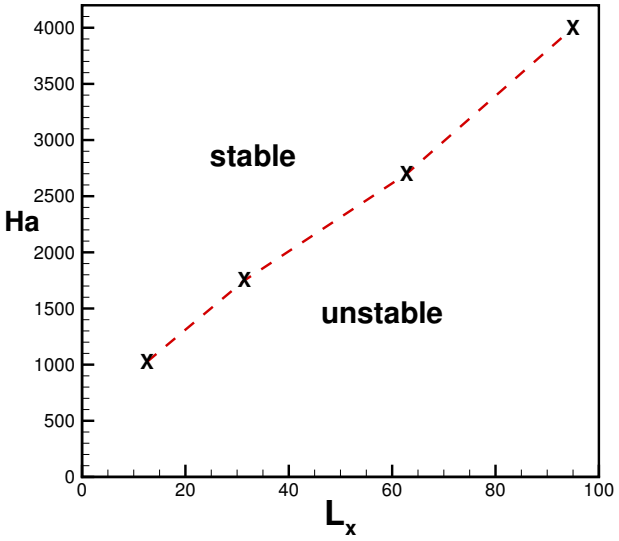

Figure 3.8: Stability diagram for two-dimensional solutions at $Gr = 10^9$. Stability thresholds at different L determined in the simulations are indicated by crosses.

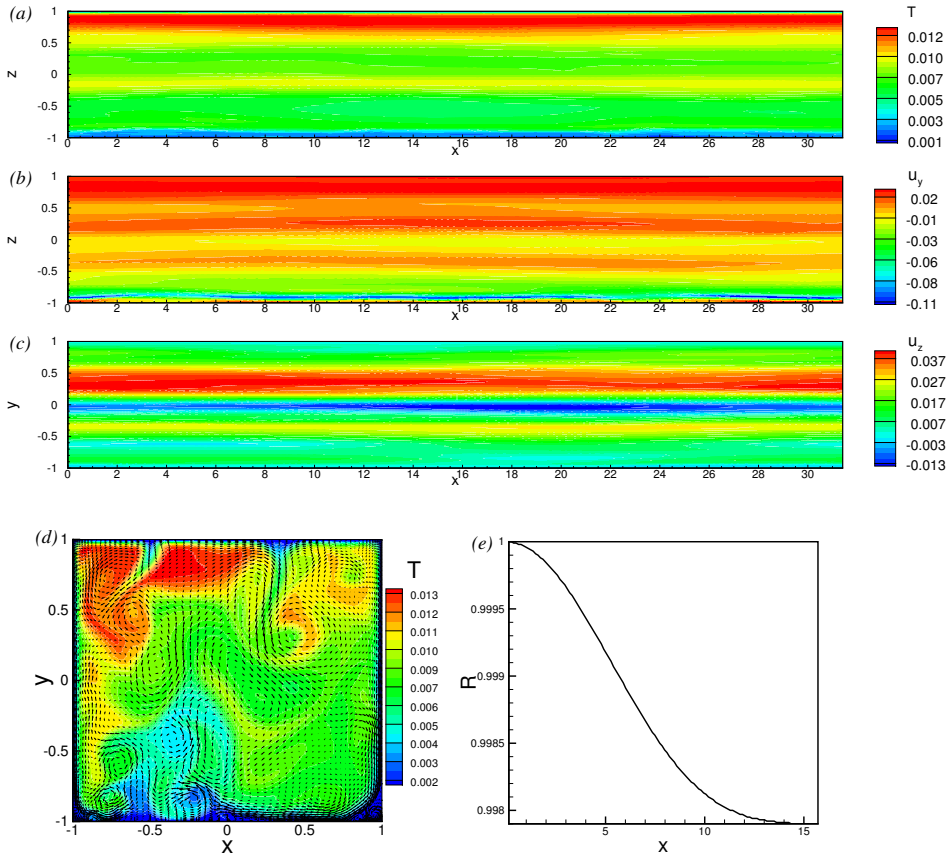

Figure 3.9: Results of 3D simulations at $Gr = 10^{11}$, $Ha = 10^4$, $L = 10\pi$. Instantaneous distributions of temperature T, and spanwise velocity u_y in the vertical plane at y=0 *(a)-(b)*, of vertical velocity u_z in the horizontal plane at z=0 *(c)*, and of T and velocity vectors in the transverse cross-section $x = L/2$ *(d)*. The two-point correlation coefficient R (3.22) is shown in *(e)*.

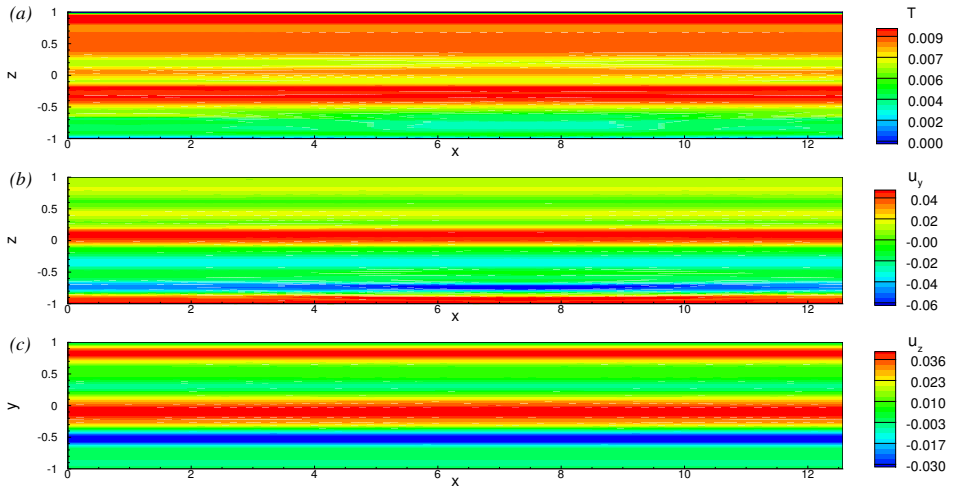

Figure 3.10: Results of 3D simulations at $Gr = 10^{11}$, $Ha = 10^4$, $L = 4\pi$. Instantaneous distributions of temperature T, and spanwise velocity u_y in the vertical plane at y=0 *(a)-(b)*, of vertical velocity u_z in the horizontal plane at z=0 *(c)*.

or smaller L.

Firstly, we look at the developed three-dimensional flow at $Gr = 10^{11}$, $Ha = 10^4$ and $L = 10\pi$ (see Fig. 3.9). The Hartmann number is slightly lower than the critical value in this case, and the perturbation energies grow in the same manner as shown in Fig. 3.7a. However, the saturation level of the perturbation energies is not large (of the order of 10^{-5}). The magnitude of perturbation velocity is only about 2% of the mean flow velocity of two-dimensional flow (see table 3.2). In Fig. 3.9a-3.9c we can see that development of 3D velocity distribution is limited to a small region close to the bottom of the duct. The rest of the flow remains practically two-dimensional. In order to quantitatively estimate the degree of three-dimensionality, we compare the two-point correlation coefficient for the vertical velocity component:

$$R(\ell) = \frac{\langle v(\boldsymbol{x}, t) v(\boldsymbol{x} + \ell \boldsymbol{e}_x, t) \rangle}{\langle v^2(\boldsymbol{x}, t) \rangle}, \tag{3.22}$$

where $\boldsymbol{x}$ is the point $(x, 0, 0)$ and the averaging is done over the streamwise direction. This coefficient is 1 if the flow is two-dimensional, and decreases to zero the degree of three-dimensionality increases. As we can see in Fig. 3.9e, the coefficient at $Gr = 10^{11}$,

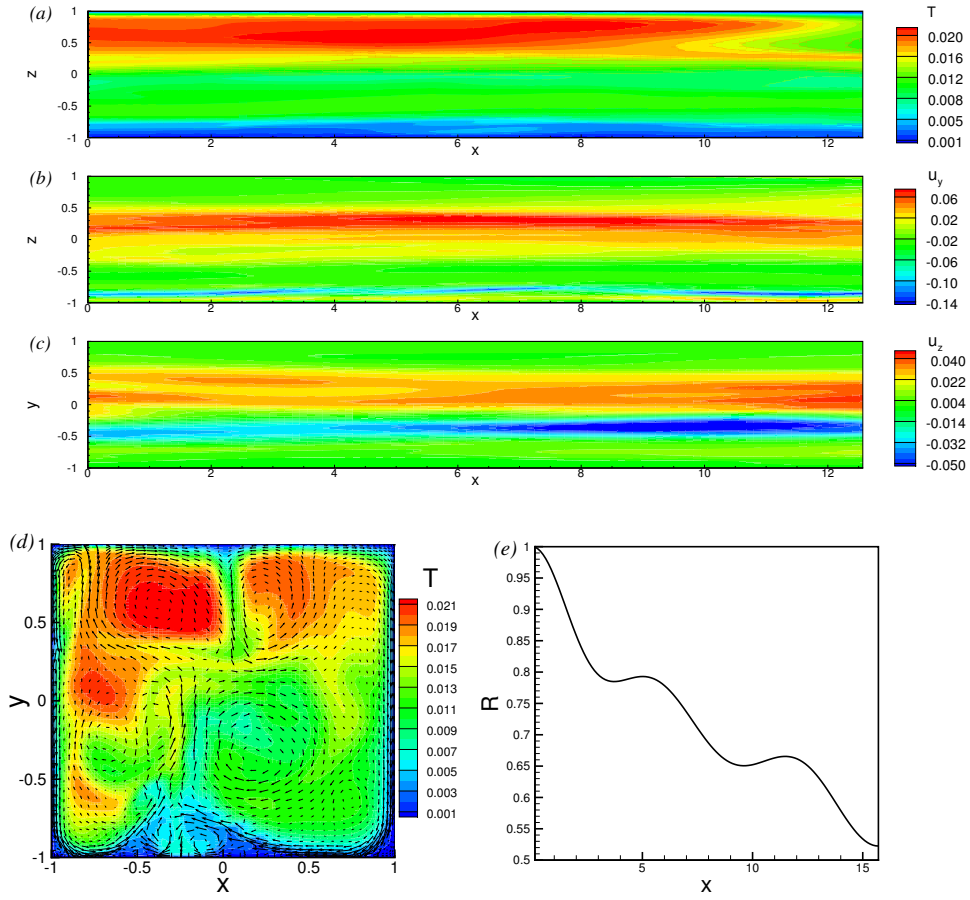

Figure 3.11: Results of 3D simulations at $Gr = 10^{10}$, $Ha = 2000$, L=10π. Instantaneous distributions of temperature T, and spanwise velocity u_y in the vertical plane at y=0 *(a)-(b)*, of vertical velocity u_z in the horizontal plane at z=0 *(c)*, and of T and velocity vectors in the transverse cross-section $x = L/2$ *(d)*. The two-point correlation coefficient R (3.22) is shown in *(e)*.

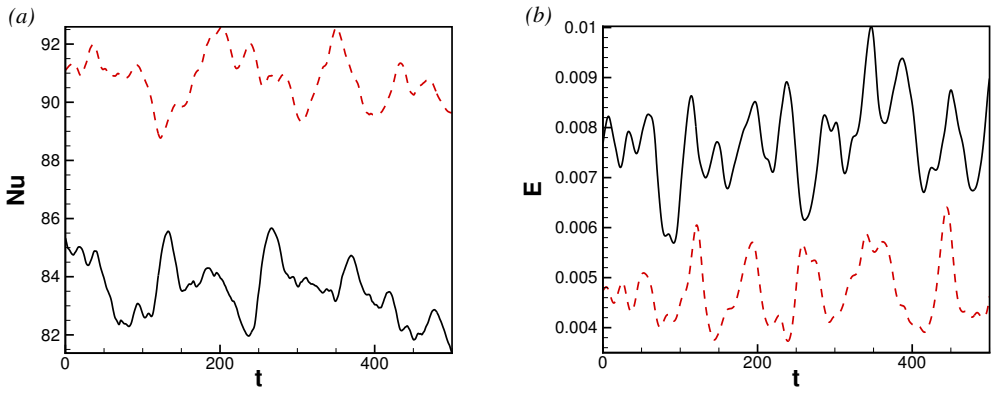

Figure 3.12: Nusselt number *Nu (a)* and total kinetic energy *(b)* at $Gr = 10^9$ as computed for the two-dimensional regime (black, solid) and three-dimensional regime at $Ha = 800$, L_z=4π (red, dashed).

$Ha = 10^4$ and $L = 10\pi$ remains well above 0.99, which indicates practically no variability in the axial direction. The fact that the 3D structures are limited to a small region close to the bottom of the duct, suggests that the transition to three-dimensionality in this flow is possibly due to the instabilities forming in the thin shear layers in the two-dimensional solution (see Fig. 3.9d).

An example of the stabilizing role of smaller duct length is shown in Fig. 3.10. The case of the same Grashof and Hartmann numbers $Gr = 10^{11}$, $Ha = 10^4$ as in Fig. 3.9 but $L = 4\pi$ is shown. We see both temperature field and velocity field maintain good two-dimensionality (see also values of E' in table 3.2).

The previous cases are all at parameters close to the critical value $Ha_{cr}(\mathrm{L})$. If the flows are at parameters far away from the critical curve, three-dimensional structures can be strong. As an example, the flow at $Gr = 10^{10}$, $Ha = 2000$, $L = 10\pi$ is shown in Fig. 3.11. The three-dimensionality becomes clearly visible. The correlation coefficient decreases to about 0.5 at ℓ close to L. A range of active x-wavelengths can be recognized from the 3D fields. The 3D structures now occupy the entire duct.

The transition to three-dimensionality affects the heat transfer in the flow. The Nusselt number is found to increase by few percent (see Fig. 3.12a). The total kinetic energy

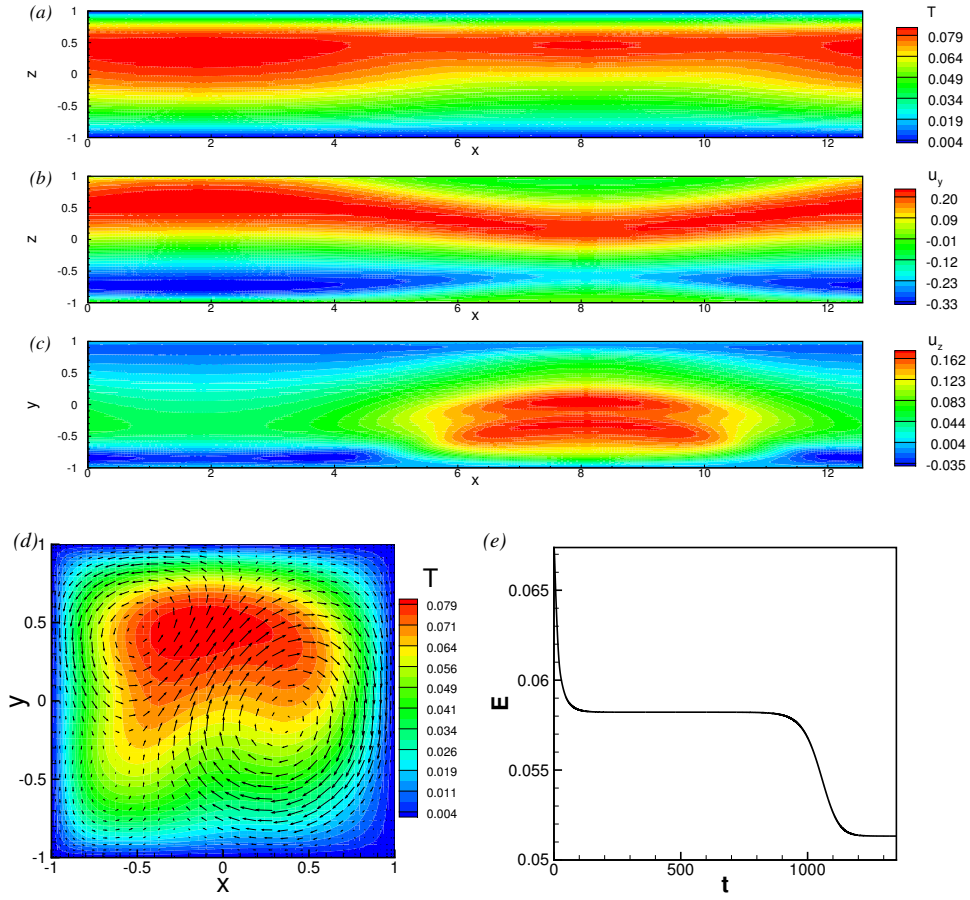

Figure 3.13: Results of 3D simulations at $Gr = 10^6$, $Ha = 30$, L=4π. Instantaneous distributions of temperature T, and spanwise velocity u_y in the vertical plane at y=0 *(a)-(b)*, of vertical velocity u_z in the horizontal plane at z=0 *(c)*, and of T and velocity vectors in the transverse cross-section $x = L/2$ *(d)*. Time evolution of the average kinetic energy is shown in *(e)*.

decreases when the transition occurs (see Fig. 3.12b), which indicates energy transfer from large-scale convection structures to small-scale structures.

It has been found in simulations of isothermal MHD flows in periodic boxes [61] and channels with spanwise magnetic field [62, 63, 64] that in a range of *Ha* around the 2D-3D critical threshold, the flow may develop characteristic MHD intermittency. In this case, the magnetic field is not strong enough to prevent the flow from transition to 3D, but it is sufficient to suppress the turbulence after it develops. This leads to a nearly periodic evolution of the flow with its period including the stage of growth of 2D structures, their instability to 3D perturbations, transition to three-dimensionality, 3D turbulent burst, and then decay to a laminar state. We have performed several long tests (more than 3000 time units) at *Ha* slightly above the instability threshold at $10^9 \leq Gr \leq 10^{11}$, but found no such intermittent behavior in our system. One possible reason is that the 3D perturbations are weak with their saturation energy much lower than the mean flow energy. Therefore, the 3D perturbations do not destroy the 2D flow structure as they are found to do in [61, 62] and thus, can not remove the mechanisms leading to the 3D instability.

We also performed tests at low *Gr* to explore if the mechanism of the transition to three-dimensionality is similar to that at high *Gr*, and whether the intermittency is present in this case. We found that the flow becomes 3D once *Ha* is greater than the critical value, and no intermittency exits. The type of the flow regime (steady or oscillatory) is kept the same as in the two-dimensional solution after the transition. This can be seen in Fig. 3.13e that the total kinetic energy of the flow decreases after the transition to three-dimensionality occurs, but the flow is still in a steady state. From the temperature and velocity field, we can see that the three-dimensional structures are of large scale, and not limited to a small region (compared to the flow at $Gr = 10^{11}$ in Fig. 3.9) but occupy the whole duct. It indicates the flow takes a form of convection with less kinetic energy when instability occurs, and the instability is no longer due to the shear layer as in the flow at high Grashof number $Gr = 10^{11}$.

3.5 Conclusions

The convection driven by internal heating in a horizontal duct with axial magnetic field has been studied in two-dimensional and three-dimensional simulations. The mean flow is neglected in this configuration, thus it is a natural convection problem.

We have studied flows in a wide range of Grashof numbers, including very high Grashof numbers, i.e. the cases, which are hard to mimic in a laboratory and for which experimental data are rarely available. The range $10^9 \leq Gr \leq 10^{11}$ corresponds to the typical heating rate q_0 from about 0.048 to 4.8 MW/m^3 (based on duct's half-width of 10 cm and physical properties of LiPb at 570 K [6]). This range entirely covers the variety of heating rates expected in a future fusion reactor, thus the results can be useful to better elucidate the impact of thermal convection on fatigue, corrosion and heat transfer in a blanket .

Flow is found to be two-dimensional and turbulent at the practically relevant high Grashof numbers $Gr \geq 10^9$, and high Hartmann numbers $Ha \sim 10^4$. Turbulent two-dimensional convection provides an effective mechanism of mixing and transport resulting in a reasonably uniform heat transfer into cooled walls. This indicates that the effect of convection is not necessarily detrimental, but can be positive, providing an efficient mechanism of mixing and heat transfer within a blanket.

Three-dimensional computations have verified that in fairly long duct, the flow maintains its two-dimensional form at $Ha \sim 10^4$ and $10^9 \leq Gr \leq 10^{11}$ typical for reactor conditions. Even when transition to three-dimensionality occurs, the energy of the saturated three-dimensional perturbations is small in comparison to the energy of the two-dimensional flow components and limited to large wavelengths. The three-dimensionality has little impact on flow structure and little to moderate impact on heat transfer. This means that, in the blanket design, the key flow parameters can be reasonably accurately evaluated in two-dimensional analysis.

In this study, we have used several idealized assumptions which make the results not directly applicable to practical blanket applications. The assumptions of zero mean velocity

and constant wall temperature are, in particular, need validation. The average amplitude of velocity caused by volumetric heating is $\sim$ 0.05 m/s in our simulations at $Gr = 10^{11}$ (based on the duct width of 10 cm and physical properties of LiPb at 570 K [6]), which is much larger than the mean axial velocity supposed in a separately cooled blanket ($\sim$ 5 mm/s in the WCLL blanket and $\sim$ 1 mm/s in the HCLL blanket). Thus the mean axial velocity would be much weaker than the circulation velocity. Our assumption of zero mean velocity is justified. The constant wall temperature assumption is less justified, since the wall temperature may vary even at high flow rates of the wall coolant. We currently do not have adequate data for a more practical temperature boundary condition. Also, the flow may change when realistic inlet and exit conditions and accompanying three-dimensional MHD effects are included. We leave the analysis of the thermal boundary condition and inlet/exit conditions to future studies.

Although our study is theoretical and based on a highly idealized model, it does show significantly different flow properties compared to the previous studies, in which the convection effects were not considered. The results of the study show potential new advantages of the old concept of a blanket with toroidal ducts. This inspires us to future investigate this concept, with more real-life complexities. This is done in the following chapters of this dissertation.

CHAPTER IV

Effect of Poloidal Magnetic Field

4.1 Configuration

The results discussed in this chapter are published in [4] and [65]. The configuration we consider in this chapter is still a liquid metal flow in a square duct with strong internal volumetric heating (see Fig. 4.1). However, the magnetic field is different. Previously, we only considered the main component of the magnetic fields (B_t in Fig. 4.1) in a fusion reactor, which is along the toroidal direction. However, there is another component, which is much weaker always and runs along the poloidal direction. Usually this field is neglected in blanket flow studies, as its strength is only about 5% of the strength of the toroidal component. However, we want to study the effect of this field to approach a more realistic model of the fusion reactor. Since the duct width ($\sim$ 10 cm) is much smaller than the typical radius of the torus of the blanket, the poloidal component can be approximated as a uniform vertical field (B_p in Fig. 4.1). The strength of the poloidal component is taken to be 5% of the toroidal one. The net magnetic field is, thus

$$\boldsymbol{B} = B_t \boldsymbol{e}_x + B_p \boldsymbol{e}_z, \tag{4.1}$$

$$B_p = 0.05 B_t. \tag{4.2}$$

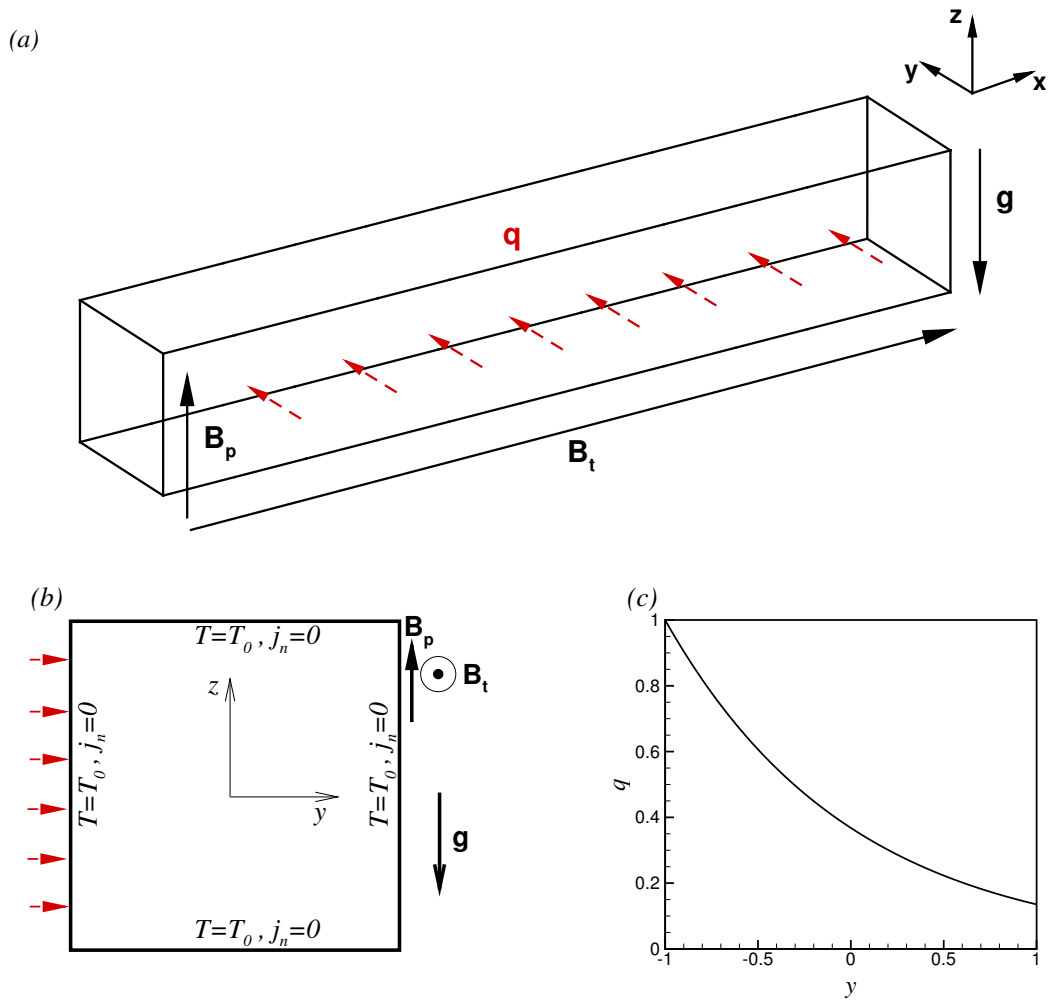

Figure 4.1: Geometry of the flow and coordinate system for 3D and 2D simulations. q is the volumetric internal heating rate.

We consider the case of liquid metal moving very slow in the duct only for the purpose of tritium extraction or purification. This is modeled by assuming that there is no mean flow. The effect of the mean flow will be studied separately in Chapter V. The duct is long compared to its width, and as an approximation, we neglect the inlet-exit effect on the flow.

In the three-dimensional simulations, we test the flows in the duct with lengths in the range $4\pi \leq L \leq 10\pi$, which covers all the possible design of a blanket in a fusion reactor.

4.2 Governing Equations and Boundary Conditions

The same set of governing equations as in the previous chapter is considered here. The only difference as we discuss below is the treatment of the Lorentz force term in the momentum conservation equation. Walls are maintained at constant temperature T_0, thus T which represents the temperature deviation from the wall temperature is zero at the walls. Further boundary conditions include those of electrically insulated and no-slip walls.

The same typical scales as in Chapter III are used to non-dimensionalize the governing equations. The only variation concerns the non-dimensionalization of the magnetic field, electric currents, and electric potential, for which the strength of the toroidal component B_t instead of the total strength of the magnetic field is used (see section 2.2.2 for a discussion of the typical scales and nondimensionalization). The non-dimensional governing equations and boundary conditions are:

$$\frac{\partial \boldsymbol{u}}{\partial t} + (\boldsymbol{u}\cdot\nabla)\boldsymbol{u} = -\nabla p + \frac{1}{\sqrt{Gr}}\nabla^2\boldsymbol{u} + T\boldsymbol{e}_z + \boldsymbol{F}_L, \tag{4.3}$$

$$\nabla\cdot\boldsymbol{u} = 0, \tag{4.4}$$

$$\frac{\partial T}{\partial t} + \boldsymbol{u}\cdot\nabla T = \frac{1}{Pr\sqrt{Gr}}\left(\nabla^2 T + q\right), \tag{4.5}$$

$$\boldsymbol{u} = T = \boldsymbol{j}_n = 0 \text{ at } y = \pm 1,\ z = \pm 1. \tag{4.6}$$

In three-dimensional simulations, periodic inlet-exit conditions are applied. For the non-dimensional parameters, we use the Grashof number *Gr*, Hartmann number *Ha*, Prandtl number *Pr*, Reynolds number $Re = Gr^{1/2}$ and the Stuart number $N = Ha^2Re^{-1}$ defined as in Chapter II (see (2.40)-(2.45)). As discussed in section 2.2.5, the toroidal magnetic field does not cause electric currents and Lorentz forces in a two-dimensional (axially uniform) flow. The currents and forces are, however, produced by the poloidal component. This means that in all the simulations, we need to solve the Poisson equation for the electric potential

$$\nabla^2\phi = \nabla\cdot(\boldsymbol{u}\times\boldsymbol{e}_b), \tag{4.7}$$

find the electric currents

$$\boldsymbol{J} = -\nabla\phi + \boldsymbol{u} \times \boldsymbol{e}_b, \tag{4.8}$$

and the Lorentz force

$$\boldsymbol{F}_L = \frac{Ha^2}{Gr^{-1/2}} \boldsymbol{J} \times \boldsymbol{e}_b. \tag{4.9}$$

where $\boldsymbol{e}_b$ is the full non-dimenisional magnetic field in the 3D case, and the non-dimensional poloidal field in the 2D case.

4.3 Parameters and Grid

Properties of the flow are those of PbLi alloy at about 570 K. Simulations are conducted at $10^6 \leq Gr \leq 10^{11}$, $800 \leq Ha \leq 10^4$ and $Pr = 0.0321$. The grids used in simulations are determined by carrying out grid sensitivity tests. As the poloidal magnetic field leads to MHD boundary layers near the walls, grids near the walls are clustered, and the clustering degree is decided carefully. Two clustering schemes are used here. The thickness of Hartmann layer is approximated as $\delta_{Ha} \sim 1/Ha$, thus at high Hartmann number, the clustering degree should increase. So, in the simulations at moderate Hartmann numbers, we use the clustering schemes based on the coordinate transformations (2.60) with the blending coefficients $C_y = C_z = 0.96$. In the simulations at high Hartmann numbers, the scheme is based on the coordinate transformation (2.59) with the clustering coefficient A_y, A_z determined in the grid sensitivity tests. We choose the clustering coefficients so as to secure that at least 6 and 12 grid points are located within the Hartmann and sidewall layers, respectively. It has been shown in [52, 29] that such a resolution is sufficient to accurately reveal the effects of the boundary layers on the nature in high-*Ha* convection-dominated flows. In three-dimensional simulations, the duct length is 4π, and uniform grid in the axial direction is used. The grid step in the axial direction is kept about 0.1 to assure sufficient resolution.

The integral properties we look at when doing grid sensitivity test are the average ki-

Gr	*Ha*	N_y	N_z	Clustering	A_y	A_z
10^9	$Ha \leq 1200$	128	128	(2.60)	0.96	0.96
10^9	$1200 \leq Ha \leq 2000$	128	128	(2.59)	1.5	2.5
10^9	$2000 \leq Ha \leq 4000$	128	128	(2.59)	2.0	3.0
10^9	$4000 \leq Ha \leq 10^4$	128	128	(2.59)	2.0	3.5
10^{10}	$Ha \leq 4000$	128	128	(2.59)	2.0	3.0
10^{10}	$4000 \leq Ha \leq 10^4$	128	128	(2.59)	2.0	3.5
10^{11}	10^4	128	128	(2.59)	2.0	3.5

Table 4.1: Numerical resolution used in 2D simulations. In 3D simulations, the same grids are extended in the x-direction with the step Δx about 0.12.

netic energy, average thermal energy, and the Nusselt number *Nu*.

$$E = \frac{1}{A}\int_A |\boldsymbol{u}|^2 dA. \tag{4.10}$$

$$E_T = \frac{1}{A}\int_A |T|^2 dA. \tag{4.11}$$

$$Nu = \frac{Q}{\langle T \rangle}, \tag{4.12}$$

where $Q = \int_A q dA$ is the total heating rate and $\langle T \rangle = A^{-1}\int_A T dA$ is the mean deviation of the temperature from the wall temperature. These characteristics are all computed using the integration over the duct's cross-section (in 2D computations) or the entire volume of the computational domain (in 3D computations) and then averaged in time. The results of the grid sensitivity tests are summarized in table 4.1.

4.4 Results

4.4.1 Two-dimensional Flows

The results of the two-dimensional simulations at various *Gr* and *Ha* are presented in table 4.2. Integral characteristics *Nu* and E and the type of the flow are shown. For comparison, we also show the analogous data obtained in the 2D simulations with purely toroidal

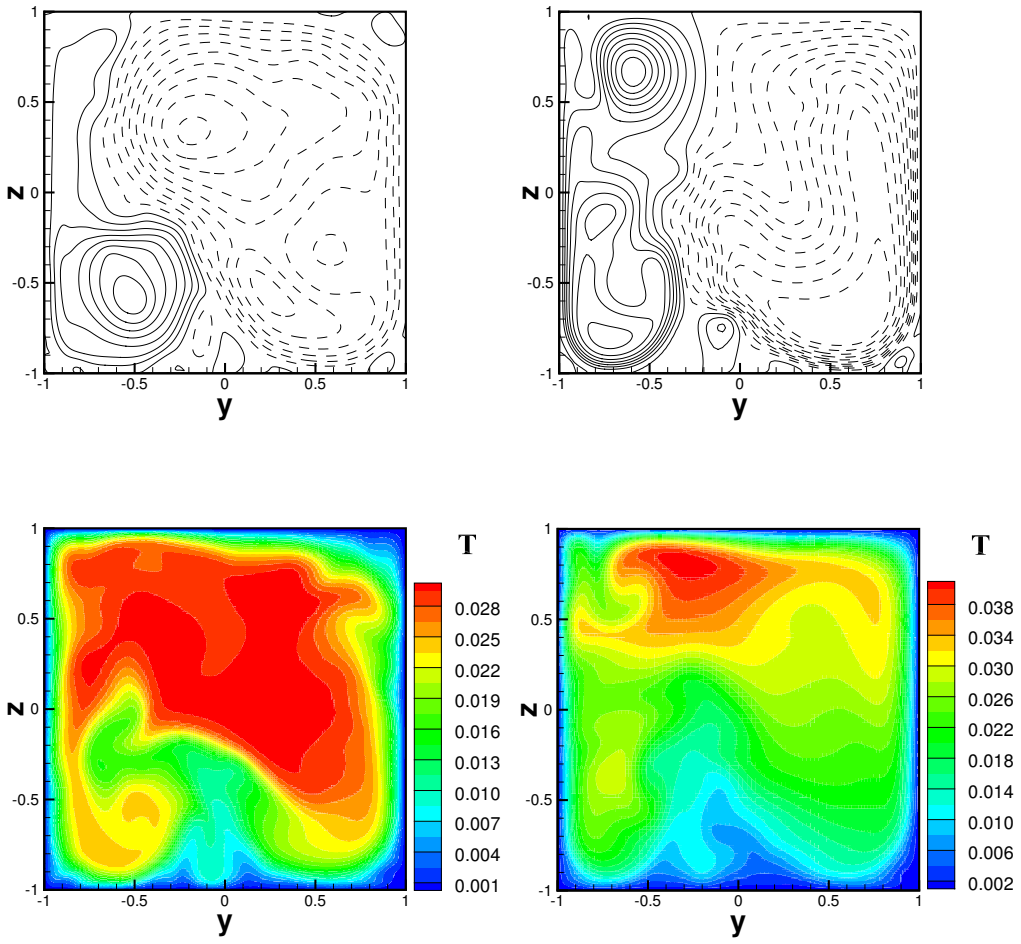

Figure 4.2: Streamfunction (solid lines indicate counterclockwise motion while dashed lines indicate clockwise motion) and temperature T at $Gr = 10^9$, $Ha = 800$ with purely toroidal magnetic field (left) (see Chapter III and [3]) and with both poloidal and toroidal magnetic field (right).

Gr	Ha	E_p	E_t	Nu_p	Nu_t
10^9	800	3.4×10^{-3}	8.0×10^{-3}	80	81.6
10^9	1200	2.4×10^{-3}	8.0×10^{-3}	78	81.6
10^9	1500	2.0×10^{-3}	8.0×10^{-3}	78	81.6
10^9	2500	1.6×10^{-3}	8.0×10^{-3}	75	81.6
10^9	3000	1.3×10^{-3}	8.0×10^{-3}	72	81.6
10^9	4000	1.1×10^{-3}	8.0×10^{-3}	67	81.6
10^9	7000	6.4×10^{-4}	8.0×10^{-3}	56	81.6
10^9	10^4	3.8×10^{-4}	8.0×10^{-3}	48	81.6
10^{10}	3000	9.1×10^{-4}	5.0×10^{-3}	119	128
10^{10}	5000	7.1×10^{-4}	5.0×10^{-3}	114	128
10^{10}	7000	5.3×10^{-4}	5.0×10^{-3}	108	128
10^{10}	10^4	3.8×10^{-4}	5.0×10^{-3}	90	128
10^{11}	10^4	2.9×10^{-4}	3.0×10^{-3}	179	206.6

Table 4.2: Results of two-dimensional simulations. Computational parameters, the total kinetic energy and Nusselt number for flows with both poloidal and toroidal magnetic field (E_p, Nu_p), and for the flows with purely toroidal magnetic field (E_t, Nu_t).

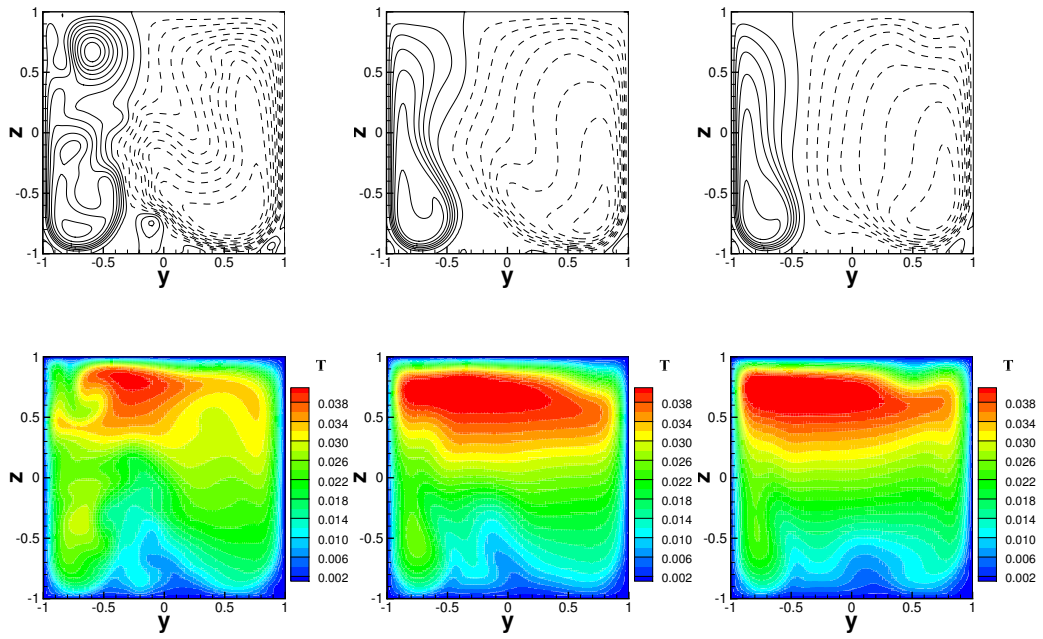

Figure 4.3: Streamfunction (solid lines indicate counterclockwise motion while dashed lines indicate clockwise motion) and temperature T of the flows with both poloidal and toroidal magnetic fields at $Gr = 10^9$, $Ha = 800$ (left), $Ha = 1200$ (middle), $Ha = 1500$ (right).

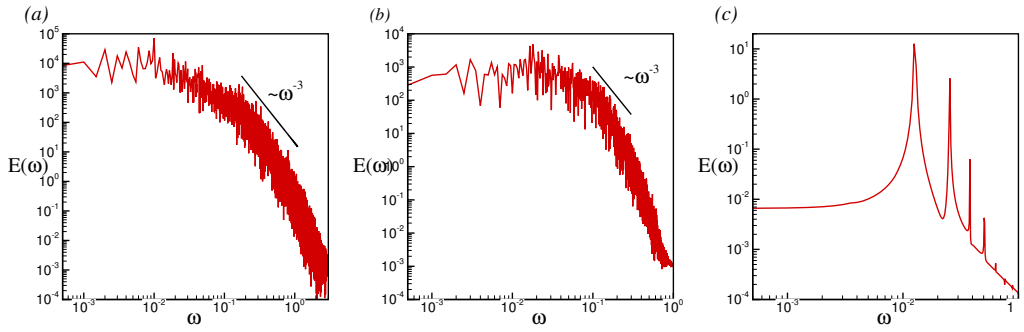

Figure 4.4: Power energy spectra in 2D flows at $Gr = 10^9$, $B_p = 0$ *(a)*, $Ha = 800$ *(b)*, $Ha = 1500$ *(c)* (in the log-scale and ω is the frequency) [4].

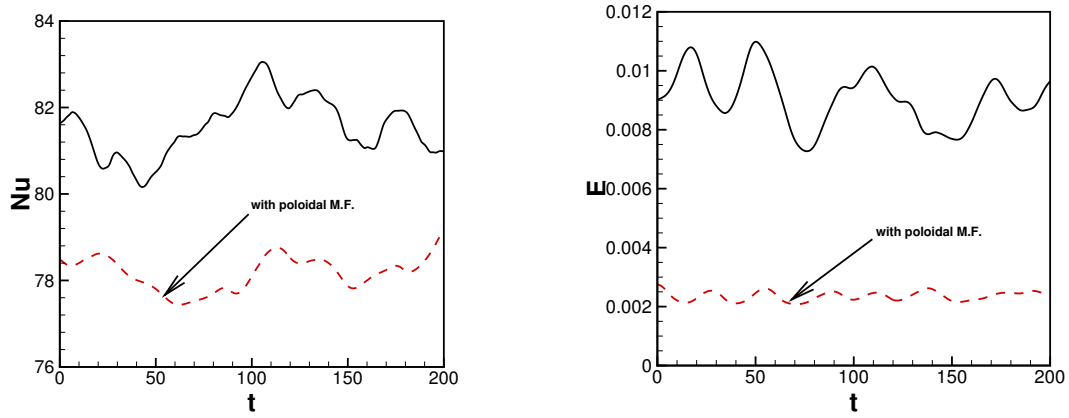

Figure 4.5: Nusselt number and total kinetic energy for $Gr = 10^9$, $Ha = 1200$ with poloidal magnetic field (red, dashed lines) and without poloidal magnetic field (black, solid lines).

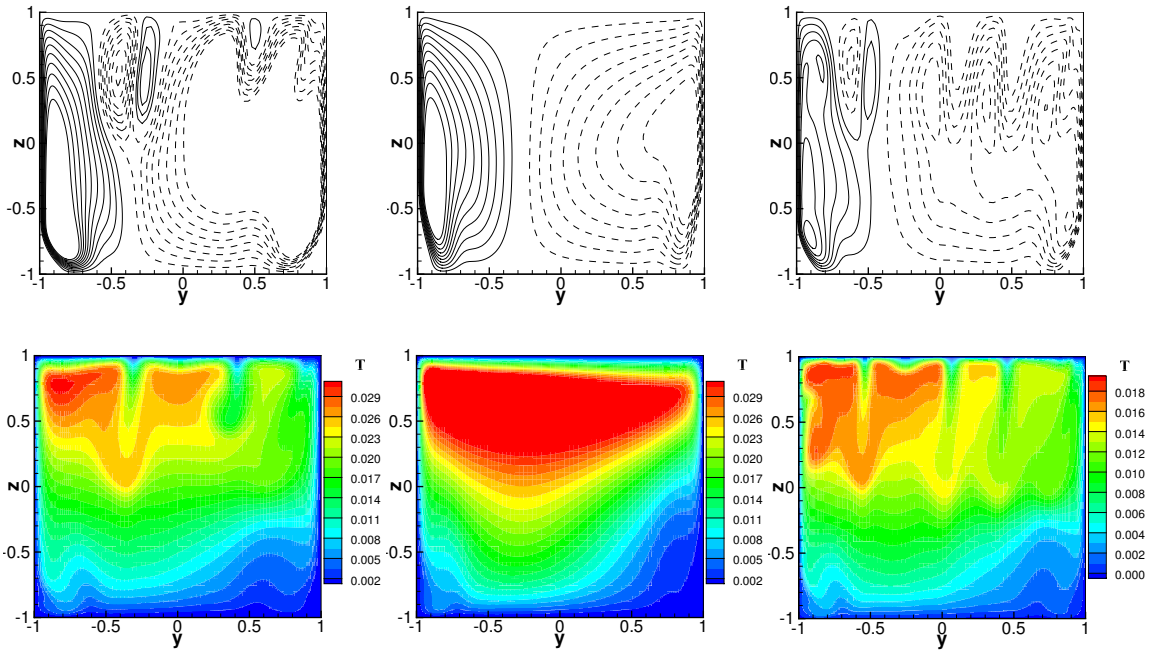

Figure 4.6: Instantaneous distributions of streamfunction Ψ (solid lines indicate counter-clockwise motion, while dashed lines indicate clockwise motion), temperature deviation T and amplitude of velocity u_z in 2D flows at $Gr = 10^{10}$, $Ha = 5000$ *(a)-(c)*, $Gr = 10^{10}$, $Ha = 10^4$ *(d)-(f)*, $Gr = 10^{11}$, $Ha = 10^4$ *(g)-(i)*.

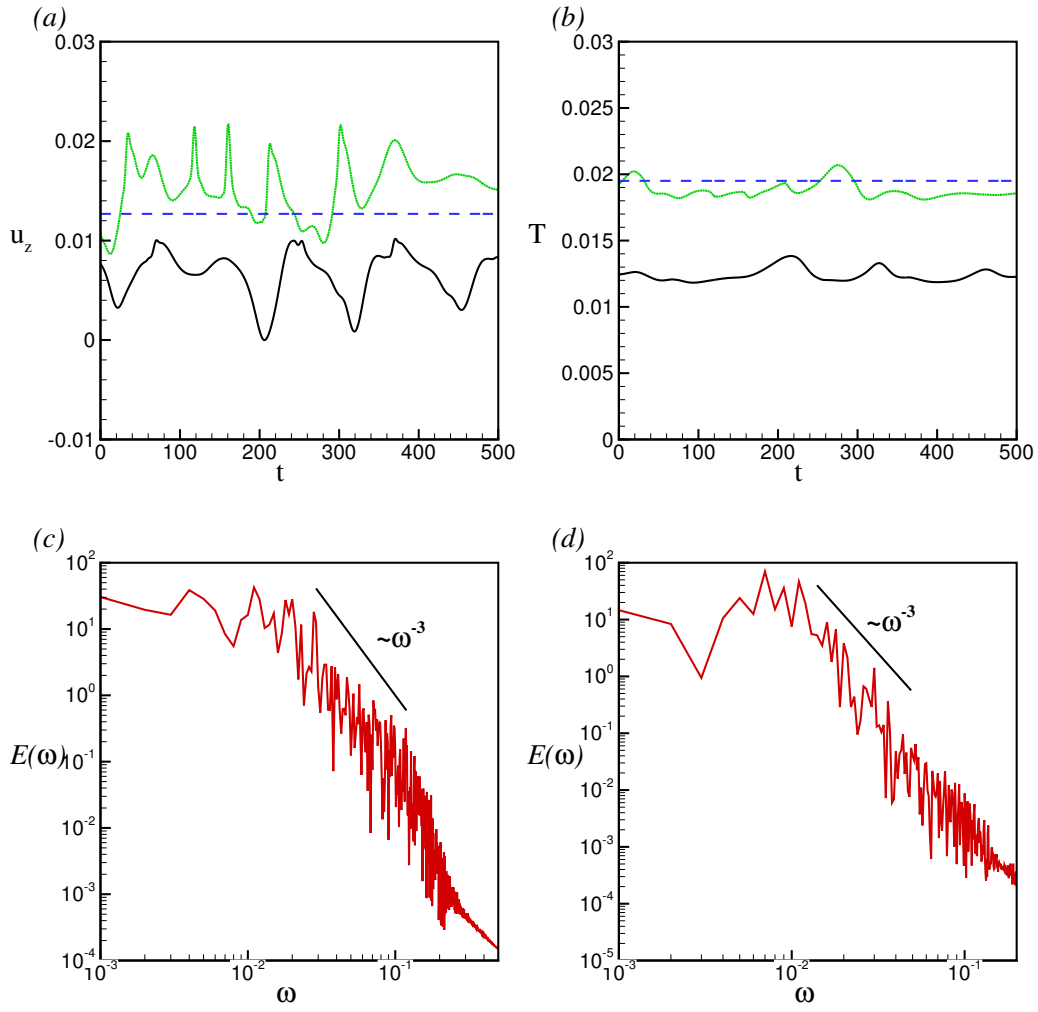

Figure 4.7: Point (at (-0.8,0)) signals of amplitude of vertical velocity *(a)*, and temperature deviation *(b)* in 2D flows shown in Fig. 4.5: at $Gr = 10^{10}$, $Ha = 5000$ (green, dotted lines), $Gr = 10^{10}$, $Ha = 10^4$ (blue, dashed lines), $Gr = 10^{11}$, $Ha = 10^4$ (black, solid lines). Power energy spectra in 2D flows at $Gr = 10^{10}$, $Ha = 5000$ *(c)*, $Gr = 10^{11}$, $Ha = 10^4$ *(d)* (in log-scale) [4].

magnetic field (see Chapter III and [3]). For unsteady flows, the global characteristics are computed over long (many hundreds of time units) periods of fully developed state and averaged in time.

From the table, we can see the total kinetic energy of the flow strongly decreases due to the suppression by the poloidal magnetic field. The suppression effect is much stronger on small-scale structures than on large-scale structures. We expect suppression of turbulence, elongation of flow structures in the vertical direction, and boundary layers. The relevant parameter determining the flow transformation is the effective Stuart number. It is based on the poloidal field B_p and the convection velocity scale $U = \sqrt{\beta g \Delta T d}$:

$$N_p = \frac{Ha_p^2}{Re} = \frac{(0.05Ha)^2}{Gr^{1/2}} = \frac{B_p d\sigma}{\rho U}. \tag{4.13}$$

In many of our cases, the value of N_p is not small and the MHD effect is expected to be significant.

The effect can be observed closer in Figs. 4.2-4.3. In Fig. 4.2, the results for $Gr = 10^9$, $Ha = 800$ are presented and compared with the results obtained in the purely toroidal magnetic field case [3]. The right column is for the flow with both poloidal and toroidal magnetic field. The magnetic field is moderately strong and the Hartmann and Stuart numbers based on the poloidal magnetic field are $Ha_p = 40$, $N_p = 0.05$. Turbulent convection is present for both cases, but some small convection structures in the flow with purely toroidal magnetic field are suppressed in the case with the combined field. Also, the convection rolls are elongated along the poloidal direction in the combined field case.

At the same time, the Nusselt number does not change much after the poloidal magnetic field is added. We see in table 4.2, that Nu_p is only slightly smaller than Nu_t, with a decrease of less than 20%. The heat transfer is still efficient which implies that it is mainly carried out by large-scale convection structures. Due to the absence of small-scale convection structures, the temperature field with both toroidal and poloidal magnetic fields has larger

maximum temperature and more non-uniform distribution as shown in Fig. 4.2.

Our next step is to increase the strength of the magnetic field and analyze the change of the flow structures. Fig. 4.3 shows the results for $Ha = 800$, $Ha = 1200$ and $Ha = 1500$. For the flow with only toroidal magnetic field, the flows of these three cases are all turbulent, while for the combined field cases, the flow becomes oscillating when the magnetic field gets stronger. Thus, after the poloidal magnetic field is imposed, the two-dimensional turbulence is suppressed to two-dimensional oscillations at high Ha and can be further suppressed to steady flow if the magnetic field is sufficiently strong (e.g $Ha = 4000$, $Gr = 10^9$).

The velocity and temperature signals for the case at $Ha = 1200$ have several dominate frequencies, while at $Ha = 1500$, there are less and weaker dominant frequencies than the ones at $Ha = 1200$. We compute the power energy spectrum as:

$$E(\omega) = \mathcal{F}_i^2(\omega), \tag{4.14}$$

where $\mathcal{F}_i(\omega)$ stands for the Fourier transform of the signal of a velocity component. The power energy spectrum shown in Fig. 4.4 verifies this trend. Flows at $Ha = 800$ and $Ha = 1200$ have spectra close to the energy spectrum of a typical 2D turbulent flow, but the spectrum at $Ha = 1500$ only has several isolated frequencies. At $Ha = 1200$, we have also computed the Nusselt number and the average kinetic energy for the cases with and without poloidal magnetic field. The comparison is shown in Fig. 4.5. It is found that the average kinetic energy decreases significantly in the presence of the magnetic field, but the Nusselt number does not decrease much.

Analyzing the cases of high Gr, we focus on the realistic situations when the imposed toroidal magnetic field is also very strong. Thus though the poloidal field is only 5% of the toroidal one, it is quite large and results in large values of the Hartmann numbers $Ha_p \leq 500$. The computational grid has been determined carefully to assure sufficient resolution

of the MHD boundary layers as mentioned earlier. The flow is expected to be suppressed to a laminar state with such a strong imposed magnetic field, but the results reveal a different flow behavior. The results at $Gr = 10^{10}$ and $Gr = 10^{11}$ are shown in Fig. 4.6. The streamfunction and temperature fields for the cases of $Ha = 5000$, $Gr = 10^{10}$ (left), $Ha = 10^4$, $Gr = 10^{10}$ (middle), and $Ha = 10^4$, $Gr = 10^{11}$ (right) are shown. The flow is steady at $Ha = 10^4$ and $Gr = 10^{10}$. This is in agreement with the high value of the effective Stuart number $N_p = 2.5$ and verifies our earlier conclusion that the poloidal magnetic field would decrease the energy of the flow and suppress it to a steady state, if strong enough. The unexpected effect is that the flow structure is not absolutely independent of the z-direction in the core of the duct even under such a strong suppression. Similarly, for the other two cases, the flow is unsteady, with two big circulation rolls and some small rolls located in the top half of the duct. Those small rolls are not suppressed, and the flow in the core is never z-independent. At $Ha = 10^4$, $Gr = 10^{11}$, the spectral analysis of the kinetic energy in Fig. 4.7d shows that it does not strictly follow the $E \sim \omega^{-3}$ law typical for 2D turbulence, but is close to that. Partly it is because our flow is very chaotic due to the intense internal heating but it is not the high-*Re* flow, and partly because the poloidal magnetic field suppresses small-scale structures that modifies the spectral distribution in certain way. Still, the flow can be regarded as quasi-2D turbulence with effective heat transfer.

To summarize, we have compared the flows with and without the poloidal component of the magnetic field. In the simulations with the purely toroidal field, the flow is found to be steady-state with regular convection rolls at low *Gr*, but change to unsteady oscillating regime at $Gr \geq 10^7$ and becomes turbulent at $Gr \geq 10^9$ (see Chapter III and Fig. 4.2a-c). The Nusselt number computed as $Nu = Q/\overline{T}$ is found to grow as $Nu \sim Gr^{0.2}$, and effective heat transfer is always maintained at high *Gr* due to the turbulence (see [3]).

The addded poloidal magnetic field suppresses small-scale convection structures and may lead to steady flow if *Ha* is very large (see Fig. 4.2e). Flow structure consists of two large counter-rotating vortices, and is characterized by strong shear layers forming

between the rolls and strong jets form near the side walls. At $Gr = 10^{11}$ (see Fig. 4.2f), turbulence is suppressed but the flow is not vertically uniform even though the Hartmann number for the poloidal magnetic field is $Ha_p = 500$. Despite the absence of turbulence, the large convection rolls mix the flow effectively, and *Nu* reduces only little in comparison to turbulent flows at the purely toroidal field.

4.4.2 Stability Analysis

The three-dimensional simulations were carried out to test the robustness of our two-dimensional model. Each simulation is initiated with a fully developed 2D state, to which weak 3D random perturbations are added. The evolution of the flow is then simulated for a long period of time t to determine whether the flow becomes 3D or reverts to the 2D state.

In order to evaluate the deviation of the 3D solutions from two-dimensionality, we compute the average energies (3.21) of the perturbations of the velocity components and temperature in comparison to the streamwise-averaged values (see (3.20)).

We find that the flow maintains good two-dimensionality when the magnetic field is strong enough. But we also find that, at a given length of the duct, the critical Hartmann number required to maintain two-dimensionality of the flow is higher when the poloidal magnetic field is added. For example, at $Gr = 10^9$, in a duct of length $L = 4\pi$, the critical Hartmann number increases from $Ha_{cr} = 1025$ to $Ha_{cr} = 1200$. At the same *Ha* below these limits, the kinetic energy of the 3D perturbations is about 20% higher in the flow with the poloidal field. This behavior seems counterintuitive, as one would expect that the two-dimensional flow would be more stable and the perturbations would be suppressed when the magnitude of the total magnetic field is increased. We have performed additional three-dimensional simulations at various parameters with both toroidal and poloidal magnetic fields to study the instability at *Ha* slightly below Ha_{cr}.

It has been found that the growth of 3D perturbations is promoted by the strong shear layers forming in the interior of the duct. When the purely toroidal magnetic field is im-

posed, the two-dimensional flow is turbulent, and no such layers exist. The poloidal magnetic field reshapes the convection structure by suppressing small vorticities, so the surviving structures are large-scale, either steady or slowly varying with time, and forming strong shear layers between them (compare the flows in Figs. 4.8a and 4.8b). The shear layers can be regarded as vortex sheets of finite thickness parallel to the poloidal magnetic field. Their instability has been analyzed, e.g. in [66] and [67]. They have found that the vortex sheets firstly develop instability similar to the Kelvin-Helmholtz instability and resulting in the eddies oriented along the direction which is parallel to the axis of the duct in our system. This effect can be clearly observed in our flows at very high *Gr* in Fig. 4.9. The left column shows the two-dimensional solutions of the flow, while the right column shows the three-dimensional results. We see that the eddies are formed at the shear layers when the instability occurs. It also shows how the strength of the magnetic field influences the unstable mode. When the magnetic field is stronger (see $Ha = 7000$ in Figs. 4.9d), the scale of the eddies decreases compared to that at $Ha = 5000$ (Figs. 4.9b). The reason is that stronger suppression results from a stronger magnetic field, so the energy of unstable mode is reduced and the typical scale is reduced. At higher $Gr = 10^{11}$ and higher $Ha = 10^4$, the structure of the unstable mode is smaller, and the location moves closer to the top wall of the duct. The distributions of the vertical velocity u_z shown in Figs. 4.10a,c,e indicate the shear effect between the rolls in the interior of the flow is significant, and the shear is reduced by the unstable mode at the onset of the instability (see Figs. 4.10b,d,f).

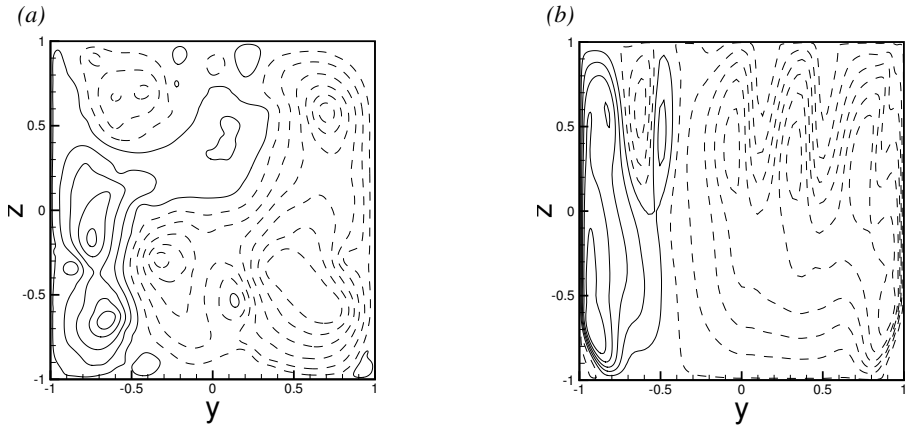

Figure 4.8: Results of 2D simulations. Instantaneous distributions of streamfunction Ψ (solid lines indicate counter-clockwise motion, while dashed lines indicate clockwise motion) in 2D flows with only toroidal magnetic field at $Gr = 10^{11}$ *(a)*, and with both toroidal and poloidal magnetic fields at $Gr = 10^{11}$, $Ha = 10^4$ *(b)*.

These structures are unstable and evolve into three-dimensional structures varying slowly along the axis at the onset of secondary instability. Presence of the strong toroidal magnetic field suppresses the flow variation, thus only the unstable modes with large wavelength can survive. The resulting eddies are three-dimensional in the sense that they vary in a snake-like manner. This is illustrated by the results of the three-dimensional simulations at $Gr = 10^{10}$ $Ha = 5000$, $Ha = 7000$ and $Gr = 10^{11}$ $Ha = 10^4$ shown in Figs. 4.11-4.13, respectively. In the horizontal plane x-y of the flow at $Ha = 5000$ (Fig. 4.10a), the distribution of the spanwise velocity u_y indicates that the unstable mode is three-dimensional with the typical axial length of about 8. At $Ha = 7000$ (Fig. 4.12b), unstable eddies occur in two regions: one is around $y = -0.4$ and one is around $y = 0.6$. The locations match the locations of the strong shear layers in Fig. 4.9c. At higher *Gr*, more shear layers are present in the two-dimensional solution (see Fig. 4.9e as an example), and, thus, more unstable eddies are expected when the instability occurs. Fig. 4.12c and Fig. 4.13c are the zoom-in plots to give better view of the wavelength of the unstable mode. We can see that, smaller eddy has similar or slightly larger wavelength, which means the aspect ratio (wavelength to transverse size) of the eddy increases. This observation agrees with the expected effect

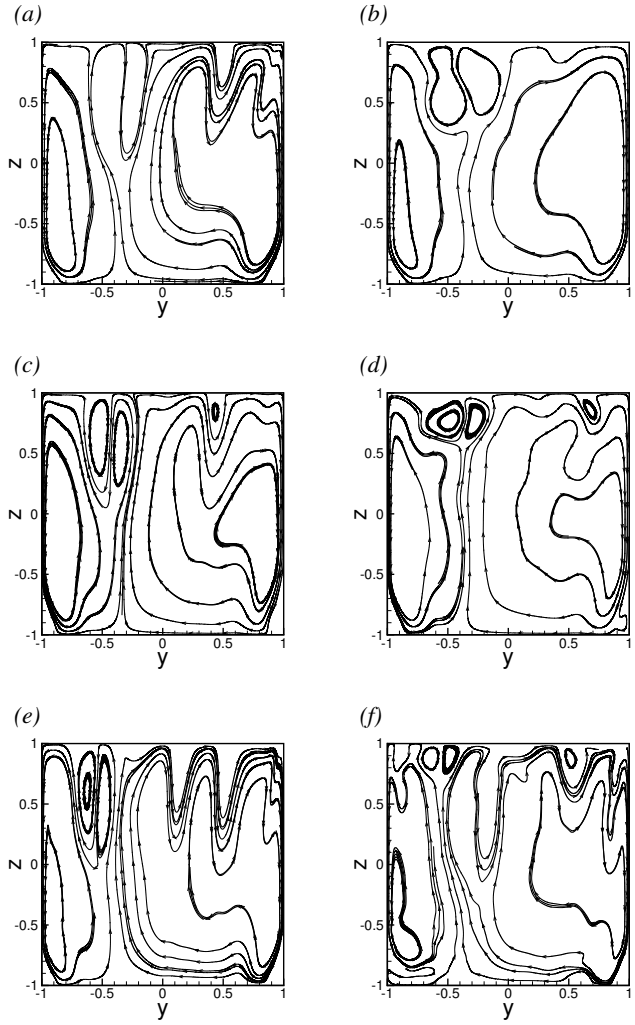

Figure 4.9: Results at $Gr = 10^{10}$, $Ha = 5000$ *(a)-(b)*, $Gr = 10^{10}$, $Ha = 7000$ *(c)-(d)* and $Gr = 10^{11}$, $Ha = 10^4$ *(e)-(f)*. Streamtraces computed using the velocity fields in 2D solutions (left column), and in three-dimensional solutions (right column) are shown.

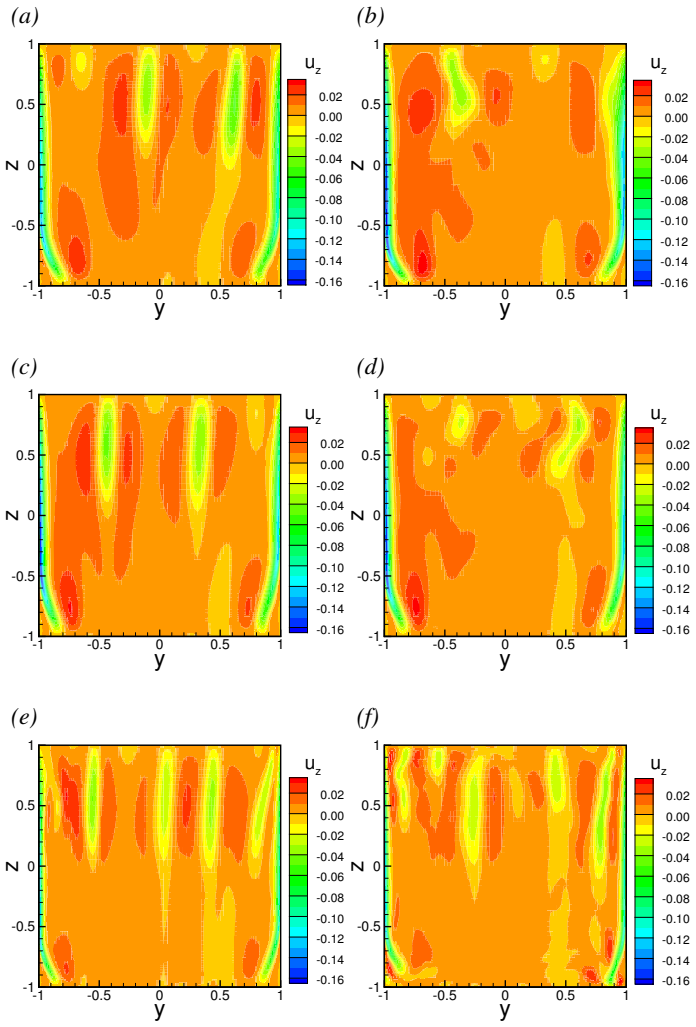

Figure 4.10: Results at $Gr = 10^{10}$, $Ha = 5000$ *(a)-(b)*, $Gr = 10^{10}$, $Ha = 7000$ *(c)-(d)* and $Gr = 10^{11}$, $Ha = 10^4$ *(e)-(f)*. Distributions of vertical velocity u_z in 2D solutions (left column), and in 3D solutions (right column) are shown.

of the increased strength of the magnetic field.

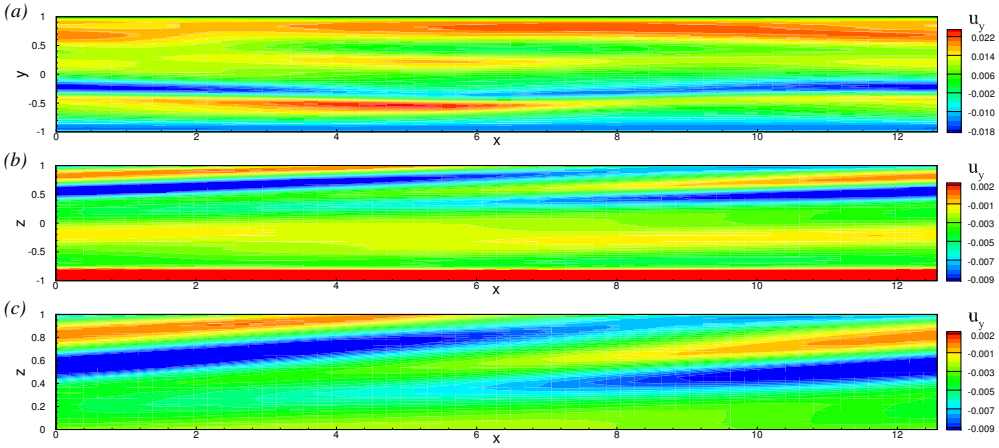

Figure 4.11: Results of 3D simulations at $Gr = 10^{10}$, $Ha = 5000$. Distributions of spanwise velocity u_y in the horizontal plane at $z = 0.5$ *(a)*, in the vertical plane at $y = -0.5$ *(b)* and in upper half of the vertical plane at $y = -0.5$ *(c)*.

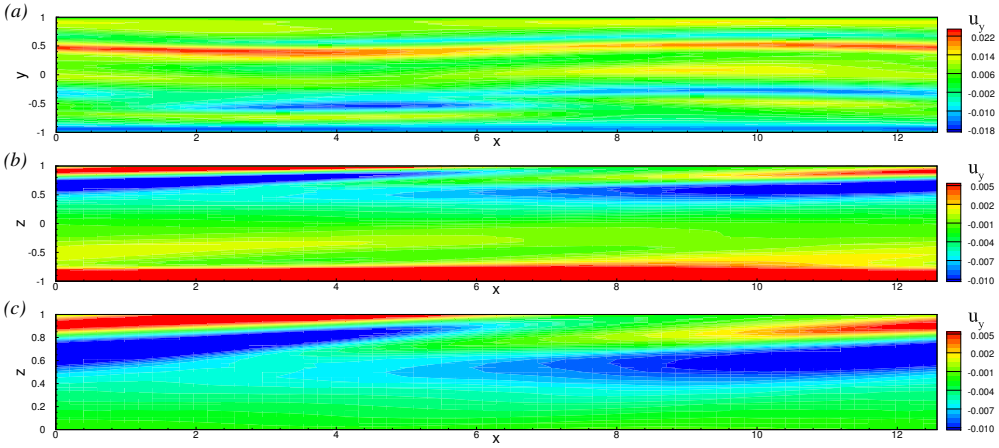

Figure 4.12: Results of 3D simulations at $Gr = 10^{10}$, $Ha = 7000$. Distributions of spanwise velocity u_y in the horizontal plane at $z = 0.75$ *(a)*, in the vertical plane at $y = -0.5$ *(b)* and in upper half of the vertical plane at $y = -0.5$ *(c)*.

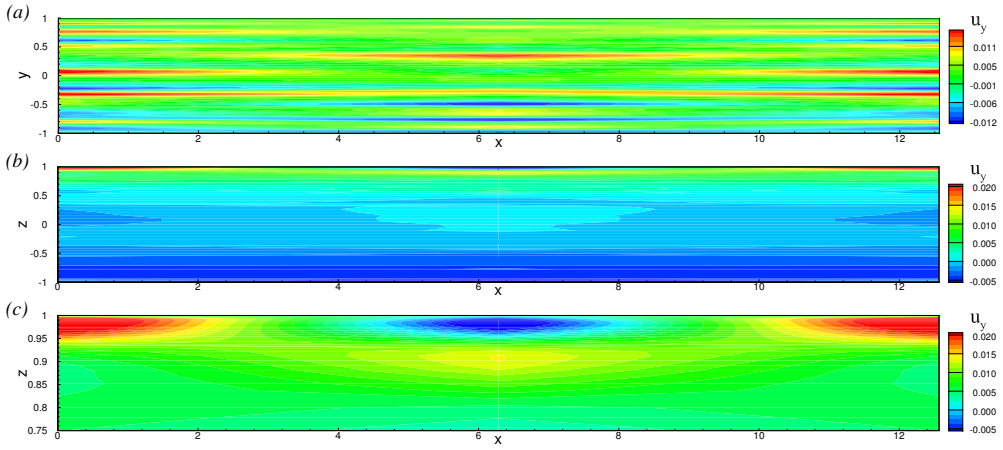

Figure 4.13: Results of 3D simulations at $Gr = 10^{11}$, $Ha = 10^4$. Distributions of spanwise velocity u_y in the horizontal plane at $z = 0.9$ *(a)*, in the vertical plane at $y = -0.5$ *(b)* and in top one eighth region of the vertical plane at $y = -0.5$ *(c)*.

Another possible instability mechanism leading to three-dimensionality in our flow is the instability of an elliptic vortex in an axial magnetic field [67]. And elliptic vortex in a two-dimensional solution is also unstable, but the the instability is weaker compared to the one associated with the vortex sheets. In Fig. 4.6, the spanwise velocity u_y distribution in the vertical plane x-z shows that the instability only occurs at the shear layer region. The rest of the flow remians nearly two-dimensional. This observation, together with the observation on the aspect ratio, suggests that, at high *Gr* and high *Ha* corresponding to the realistic reactor conditions, the unstable mode has small scale in the transverse plane and large wavelength, and the location moves closer to the top wall. These modes only exist at locations of shear layers, leaving the rest of the flow two-dimensional. It is expected that at extremely high *Gr* and *Ha*, the region of unstable mode is small compared to the duct domain, and would be insignificant to the flow properties. Thus the three-dimensional instability does not influence the overall characteristics of the flow much. The two-dimensional model is still a good choice to study the flow. Also, as we indicated before, there exist critical Hartmann numbers above which the flow is two-dimensional.

4.5 Conclusions

The effect of the poloidal component of the magnetic field on the heat transfer in the flow with strong internal heating has been studied. The poloidal magnetic field suppresses the small-scale convection structures, elongates the circulation rolls along the poloidal direction, forms strong shear layers in the interior of the flow and strong thin jets near the side walls. It decreases the kinetic energy of the flow significantly and makes the flow less stable. The Nusselt number does not decrease much, as the large-scale circulation rolls carrying out the heat convection survive even when the poloidal magnetic field is strong. At high *Gr* and *Ha*, the flow is suppressed from turbulence to 2D oscillation state. It does not, however, form a z-independent core, as one would expect at such a high vertical magnetic field. At very high *Gr*, quasi-2D turbulence may still survive, and the strong mixing effect makes the heat transfer effective. Thus, even though the poloidal magnetic field is quite weak compared to the main field, it is critical to the flow behavior in the toroidal layout of the blanket design and should be considered.

The three-dimensional stability analysis indicates that the flow is less stable to 3D perturbations due to the reshaping of the convection structures caused by the poloidal field. Strong shear layers are formed, and the instability occurs at these layers. When the transition to three-dimensionality occurs, the unstable mode is in the form of axially oriented eddies, inclined at certain angles with respect to the duct's axis. The unstable mode changes slowly in the axial direction. Its ratio of the transverse size to axial wavelength increases when the strength of the magnetic field increases. The instability only happens at the locations with strong shear in the interior of the duct. The rest of the flow remains stable to the 3D perturbations. As a result, the 3D instabilities have limited effect on the overall flow features.

Even though the poloidal magnetic field suppresses the flow variations, and prevent the flow from being turbulent, the surviving large-scale circulation rolls still provide sufficient mixing effect. This means that the promise of the separately cooled blanket concept iden-

tified using the simplified model in Chapter III remains valid. Also, the flow in such a configuration never suffers from the high-amplitude low-frequency temperature fluctuation anticipated in other blanket schemes as shown in [23, 68, 26, 27, 31, 29]. As indicated by our results, the amplitudes of the temperature fluctuations in the flows are never high, even at very large *Gr* and *Ha*. In the case at $Gr = 10^{11}$ and $Ha = 10^4$, if the duct half-width is taken as $d = 10$ cm, the amplitude of temperature fluctuation is just 6.6 K (see Fig. 4.6b (black, solid line)) [4].

CHAPTER V

Effect of Mean Flow

The results presented in this chapter are published in [5]. In this Chapter, we again consider a model of a toroidal blanket with magnetic field oriented in the direction of the duct. The model is different from those in the Chapter III and IV where we analyzed a separately cooled blanket with negligible mean flow and constant wall temperature. We now move on to another blanket type, where the heat is diverted by the flow itself. So, the key change is the presence of significant mean flow in the duct. In regard of heat balance, the configuration is conceptually similar to the DCLL blanket [17]. FCI is used to make the duct walls thermally and electrically insulated to avoid excess MHD pressure drop. The auxiliary cooling is only applied to the first wall to remove the radiation heat flux of plasma, while the heat deposited by the absorbed neutrons is fully diverted by the flow (see Fig. 1.4).

The results presented in Chapter III and IV suggest that the flow is either two-dimensional turbulent or consists of effective convection cells in the transverse plane, and that the mixing effect is always effective. The sufficient heat transfer removes the potential of the instability associated with the high-amplitude low-frequency temperature fluctuations found in poloidal ducts and indicates that the thermal convection affects the flow significantly and positively.

The purpose of this chapter is to check an idealized model of another type of the toroidal

blanket to see if the effect of convection is also significant and beneficial to the blanket operation. Also, it is a more complicated case of mixed (combined natural and forced) convection than in the previously considered natural convection systems.

5.1 Configuration

The flow configuration is similar to that in Chapter III (compare Figs. 3.1 and 5.1). The difference is that there is mean flow in the axial direction now. It is assumed that the heat transfer by the mean flow completely diverts the heat deposited within the duct by the absorbed neutrons. This allows us to model the duct walls as thermally perfectly insulated. We do not consider the poloidal component of the magnetic field. The magnetic field $\boldsymbol{B}$ is purely toroidal, steady, and uniform. Assuming that the flow is fully-developed and the magnetic field is very strong, we adopt the assumption of two-dimensional (streamwise uniform) flow in this configuration again. The validity of the assumption is then verified in the 3D stability analysis. The computational domain is a square in the two-dimensional simulations, and a fairly long straight duct with neglected ends effect in the three-dimensional analysis (see Fig. 5.1).

5.2 Governing Equations and Boundary Conditions

The typical scales are similar to those used in Chapters III and IV, except that the velocity scale is now the mean flow velocity U_m. This also implies a different time scale d/U_m. The non-dimensional governing equations are:

$$\frac{\partial \boldsymbol{u}}{\partial t} + (\boldsymbol{u}\cdot\nabla)\boldsymbol{u} = -\nabla p - \nabla\hat{p} - \nabla\tilde{p} + \frac{1}{\boldsymbol{Re}}\nabla^2\boldsymbol{u} + \boldsymbol{F}_b + \boldsymbol{F}_L, \tag{5.1}$$

$$\nabla\cdot\boldsymbol{u} = 0, \tag{5.2}$$

$$\frac{\partial\theta}{\partial t} + \boldsymbol{u}\cdot\nabla\theta = \frac{1}{\boldsymbol{Pe}}(\nabla^2\theta + q) - u_x\frac{dT_m}{dx}. \tag{5.3}$$

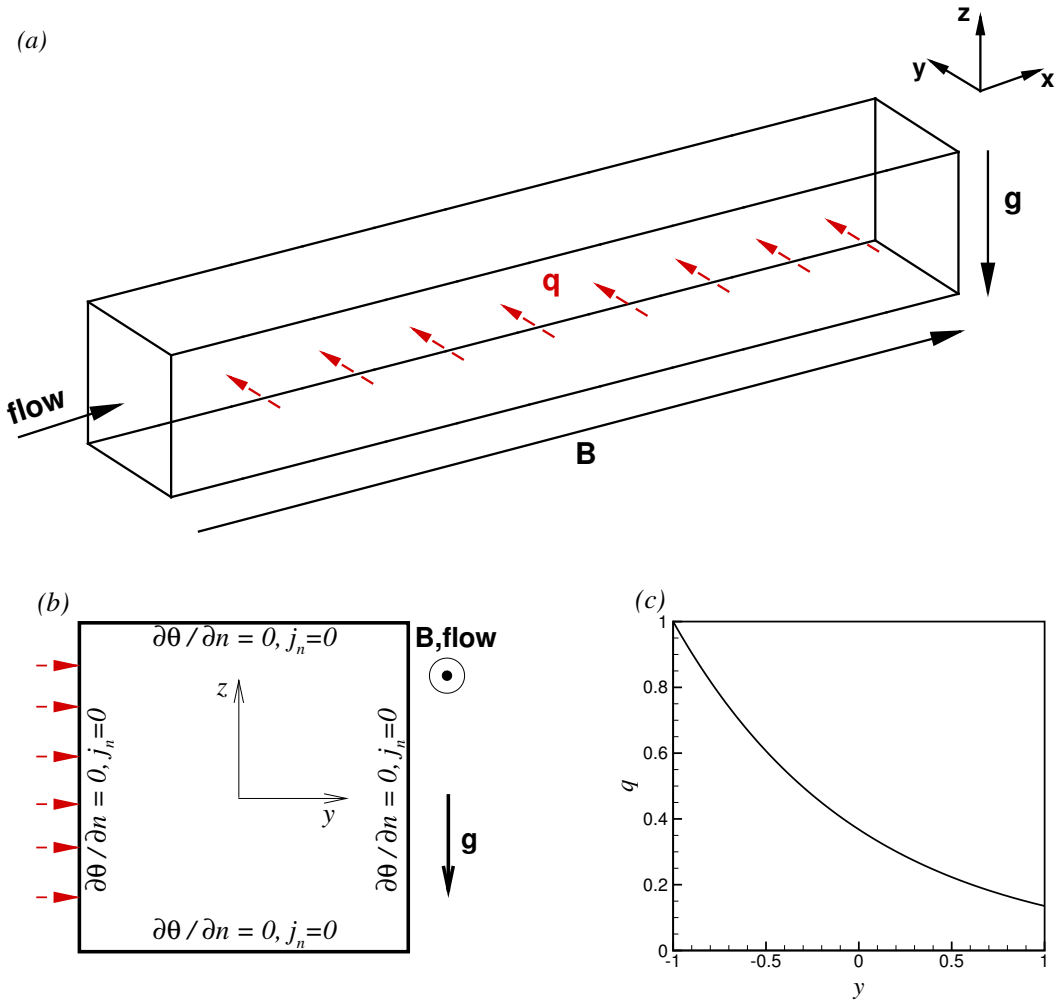

Figure 5.1: Geometry of the flow and coordinate system for 3D and 2D simulations. q is the volumetric internal heating rate.

The Lorentz force $\boldsymbol{F}_L$ is zero in 2D simulations. In 3D simulations, it is found as shown by (3.6)-(3.8).

The same model of the internal heating rate is used, with the non-dimensional heating rate being $q = \exp[-(y+1)]$. The non-dimensional parameters are the Grashof number *Gr* (2.44), Reynolds number $\mathit{Re} = Ud/\nu$ (2.40), which is now an independent parameter unrelated to *Gr*, Prandtl number *Pr* (2.41), and Hartmann number *Ha* (2.43). The Peclet number $\mathit{Pe} = \mathit{RePr}$ (2.42) also appears in (5.3).

In a duct with insulated walls and internal heating source, the mean flow temperature grows along the duct. In order to study the flow using a 2D model, or a 3D model with periodic inlet-exit conditions, special decomposition of the temperature field is necessary:

$$T(\boldsymbol{x}, t) = T_m(x) + \theta(y, z, t). \tag{5.4}$$

θ is the temperature fluctuations and T_m is the mean-mixed temperature

$$T_m(x) = \frac{1}{A}\int_A u_x T dA, \tag{5.5}$$

where A is the cross-section area of the duct. Considering the steady-state or time-averaged energy balance between the volumetric internal heating and the heat transfer by the streamwise flow, we find

$$\frac{dT_m}{dx} = \frac{Q}{A\mathit{Pe}} = \frac{Q}{A\mathit{PrRe}} = const > 0, \tag{5.6}$$

where $Q = \int_A q dA$ is the non-dimensional internal heating rate per unit length of the duct. The mean-mixed temperature grows linearly along the duct with a constant gradient depending on the internal heating rate and the streamwise velocity. It can be easily shown that the mean temperature $\overline{T} = A^{-1}\int_A T dA$ grows linearly with the same gradient. Thus, for a duct of a given length, the increase of the mean temperature between inlet and exit is known, once the Grashof number *Gr* and the Reynolds number *Re* are fixed.

The buoyancy force is

$$\boldsymbol{F}_b = \frac{Gr}{Re^2}\theta \boldsymbol{e}_z. \tag{5.7}$$

This term only includes the force associated with the temperature fluctuations found as a part of solution (see (5.1)-(5.3)). In order to account for the buoyancy force caused by the mean-mixed temperature $T_m(x)$

$$\tilde{\boldsymbol{F}}_b = \frac{Gr}{Re^2} T_m(x) \boldsymbol{e}_z, \tag{5.8}$$

we apply the formulation used earlier in [69, 70, 27, 29]. The total pressure field P is represented as:

$$P = \hat{p}(x) + \tilde{p}(x, z) + p(x, y, z, t). \tag{5.9}$$

According to this formula, the total pressure field consists of the perturbations of $p(x, y, z, t)$, the field $\tilde{p}(x, z)$ corresponding to the buoyancy force (5.8), and the pressure $\hat{p}(x)$ whose constant streamwise gradient drives the flow. The axial uniformity or inlet-exit periodicity conditions can only be applied to the perturbations field $p(x, y, z, t)$. The gradient $d\hat{p}(x)/dx$ is spatially uniform, and its value is adjusted at every time step to maintain the non-dimensional mean velocity equal to one. The role played by $\tilde{p}(x, z)$ is non-trivial and needs a more detailed discussion. It arises in response to the buoyancy force (5.8) associated with the mean-mixed temperature and has the form

$$\tilde{p}(x, z) = \frac{dT_m}{dx} \frac{Gr}{Re^2} xz = \frac{QGr}{ARe^3 Pr} xz. \tag{5.10}$$

Thus, in the vertical momentum equation, the gradient of this term represents exactly the buoyancy force $\tilde{\boldsymbol{F}}_b$

$$\frac{\partial \tilde{p}(x, z)}{\partial z} \boldsymbol{e}_z = \frac{QGr}{ARe^3 Pr} x \boldsymbol{e}_z = \frac{Gr}{Re^2} T_m(x) \boldsymbol{e}_z. \tag{5.11}$$

This buoyancy force increases linearly with x and has non-zero curl. Accordingly, it cannot be represented as a pure gradient. An additional term appears in the x-component equation:

$$\frac{\partial \tilde{p}}{\partial x} = \frac{QGr}{ARe^3 Pr} z = \frac{Gr}{Re^2} T_m(x) z. \tag{5.12}$$

This gradient drives the flow in the positive x-direction in the lower half of the duct and in the negative x-direction in its upper half. It can result in perceptible top-bottom asymmetry of the streamwise velocity profile at high $GrRe^{-3}$ as indicated by [27, 29, 5]. It should be stressed that $\tilde{p}$ is not an artifact force, but the real physical effect that would normally be generated by the total pressure field. The only reason we have this term as separate is that we want to study the flow as 2D (streamwise-uniform) or in a 3D model with periodic inlet-exit conditions.

The boundary conditions at the walls are those of perfect electric insulation

$$\frac{\partial \phi}{\partial n} = 0 \text{ at } y = \pm 1, \ z = \pm 1, \tag{5.13}$$

thermal insulation

$$\frac{\partial \theta}{\partial n} = 0 \text{ at } y = \pm 1, \ z = \pm 1, \tag{5.14}$$

and no-slip

$$\boldsymbol{u} = 0 \text{ at } y = \pm 1, \ z = \pm 1. \tag{5.15}$$

5.3 Parameters and Grid

In the model with insulated walls and strong internal heating, heat is diverted by the flow itself, thus the working temperature is expected to be higher than that in a model with external heat exchanger [9]. The working temperature is estimated as 625 K, and the flow properties are those of the PbLi alloy (see [6] and table 2.1). We carried out the simulations at $Pr = 0.0235$, $10^6 \leq Gr \leq 10^{11}$ and $10^3 \leq Re \leq 10^6$.

Gr	Re	N_y	N_z
10^6	$2000 \leq Re \leq 10^4$	64	64
10^7	$5000 \leq Re \leq 10^4$	96	96
10^8	$10^4 \leq Re \leq 10^5$	128	128
10^9	$2 \times 10^4 \leq Re \leq 10^6$	128	128
10^{10}	$5 \times 10^4 \leq Re \leq 10^6$	256	256
10^{11}	10^6	256	256

Table 5.1: Numerical resolution used in simulations [5].

The range of the Reynolds number cannot be arbitrarily decided but has to take into account practical technological considerations for a blanket. For a blanket module with the typical duct width, too large Reynolds number means the mean flow velocity is too high, and may require unacceptably excessive power input to drive the flow. At the same time, the Reynolds number cannot be too small. We see in (5.12) that this leads to strong streamwise gradient $\partial\tilde{p}/\partial x$. As shown later in this chapter, the resulting change of the flow structure is profound and, generally, undesirable.

The numerical scheme is the finite difference solver described in section 2.3.1. There is no poloidal magnetic field, thus no thin MHD boundary layers near the walls. The requirement on the clustering degree of the grid is not high, thus coordinate transformation (2.60) is sufficient and the blending coefficients $C_y = C_z = 0.96$ are used. This clustering scheme was used in [52, 3] for simulations of duct flows at high Reynolds and Grashof numbers successfully.

Grid sensitivity tests were carried out to determine the resolution that provides accurate solutions. Grids used in the two-dimensional simulations are summarized in table 5.1. In the three-dimensional simulations, the grid step Δx is always kept less than 0.1.

5.4 Results

5.4.1 Two-dimensional flows

The flow is firstly studied using a two-dimensional model with the assumption that the axial magnetic field is very strong, so the flow variations in the axial direction can be neglected. Our computational domain is a square as shown in Fig. 5.1. The computed integral properties are the averaged temperature difference between the top and bottom walls, the kinetic energy of transverse circulations and the kinetic energy of the streamwise velocity:

$$E_{\perp} = \frac{1}{A}\int_{A}({u_y}^2 + {u_z}^2)dA, \tag{5.16}$$

$$E_x = \frac{1}{A}\int_{A}{u_x}^2 dA, \tag{5.17}$$

where A is the cross-section area. Two pressure gradients are also interesting to be compared: the pressure gradient associated with the growing mean-mixed temperature $\partial\tilde{p}/\partial x = \frac{QGr}{ARe^3Pr}$ and the driving pressure gradient $d\hat{p}/dx$. The pre-determined coefficients are *Gr* and *Re*. Each test lasts thousands of time units. For the unsteady flow, the integral properties are time averaged.

The integral properties are shown in table 5.2, where we also indicate flow's spatial type and time dependency (see further text for a discusssion). We then look into the detailed flow structures of each type with the results shown in Figs. 5.2-5.6. For each case, we compute the flow until fully developed and show the streamfunction in the transverse plane, the distributions of the temperature fluctuations θ, streamwise velocity u_x, and the time signal of the vertical velocity u_z at the location (-0.7, 0). We firstly look at the flows at moderate Grashof numbers $10^6 \leq Gr \leq 10^8$ (see Fig. 5.2), and then move to high Grashof numbers $Gr \geq 10^9$ (see Fig. 5.3-5.4). The effect of *Re* is shown in Fig. 5.3 by keeping $Gr = 10^9$ but varying *Re*. The effect of *Gr* is shown in Fig. 5.4 by keeping $Re = 5 \times 10^5$ but varying *Gr*.

There are two types of the flow (see table 5.2) which can be described as those of

Gr	*Re*	$\frac{QGr}{ARe^3Pr}$	$d\hat{p}/dx$	θ_{top}-θ_{bot}	$E_\perp$	E_x	Flow type	Time behavior
10^6	2000	2.3×10^{-3}	4.6×10^{-3}	0.049	3.26×10^{-2}	1.42	I	S
10^6	10^4	1.8×10^{-5}	8.6×10^{-4}	0.047	1.43×10^{-3}	1.45	I	S
10^7	5000	1.5×10^{-3}	3.4×10^{-3}	0.073	1.51×10^{-2}	1.23	I	U
10^7	10^4	1.8×10^{-4}	1.7×10^{-3}	0.034	4.06×10^{-3}	1.24	I	U
10^8	10^4	1.8×10^{-3}	2.3×10^{-3}	0.048	6.00×10^{-3}	1.76	I	U
10^8	2×10^4	2.3×10^{-4}	1.3×10^{-3}	0.041	2.33×10^{-3}	1.15	I	U
10^8	10^5	1.8×10^{-6}	2.6×10^{-4}	0.037	1.22×10^{-4}	1.15	I	U
10^9	2×10^4	2.3×10^{-3}	1.6×10^{-3}	0.474	3.74×10^{-4}	1.81	II	S
10^9	5×10^4	1.5×10^{-4}	8.3×10^{-3}	0.026	1.76×10^{-3}	1.11	I	U
10^9	10^5	1.8×10^{-5}	4.3×10^{-3}	0.019	4.94×10^{-4}	1.11	I	U
10^9	5×10^5	1.5×10^{-7}	7.7×10^{-5}	0.021	1.53×10^{-5}	1.11	I	U
10^9	10^6	1.8×10^{-8}	3.6×10^{-5}	0.025	3.07×10^{-6}	1.11	I	U
10^{10}	10^5	1.8×10^{-4}	3.5×10^{-4}	0.110	9.46×10^{-5}	1.20	II	U
10^{10}	2×10^5	2.3×10^{-5}	1.7×10^{-4}	0.069	3.39×10^{-5}	1.17	II	U
10^{10}	5×10^5	1.5×10^{-6}	6.9×10^{-5}	0.053	8.81×10^{-6}	1.15	II	U
10^{10}	10^6	1.8×10^{-7}	3.8×10^{-5}	0.040	4.80×10^{-6}	1.11	II	U
10^{11}	5×10^5	1.5×10^{-5}	8.9×10^{-5}	0.111	2.11×10^{-5}	1.15	II	U

Table 5.2: Summary of simulation results. $\frac{QGr}{ARe^3Pr}$ is the parameter that measures the strength of the additional streamwise pressure gradient (see (5.12)). $d\hat{p}/dx$ is the constant streamwise gradient applied to drive the flow. θ_{top}-θ_{bot} is the difference between the average temperatures of the top and bottom walls. $E_\perp$ and E_x are the average kinetic energies of transverse (y, z) and streamwise (x) velocity components. For unsteady flow regimes, the integral characteristics are obtained by time-averaging over long (thousands of time units) periods. Time behavior (S for steady-state and U for unsteady) and flow type (I for flows with developed convection and II for flows with suppressed convection) are also identified (see text for discussion).

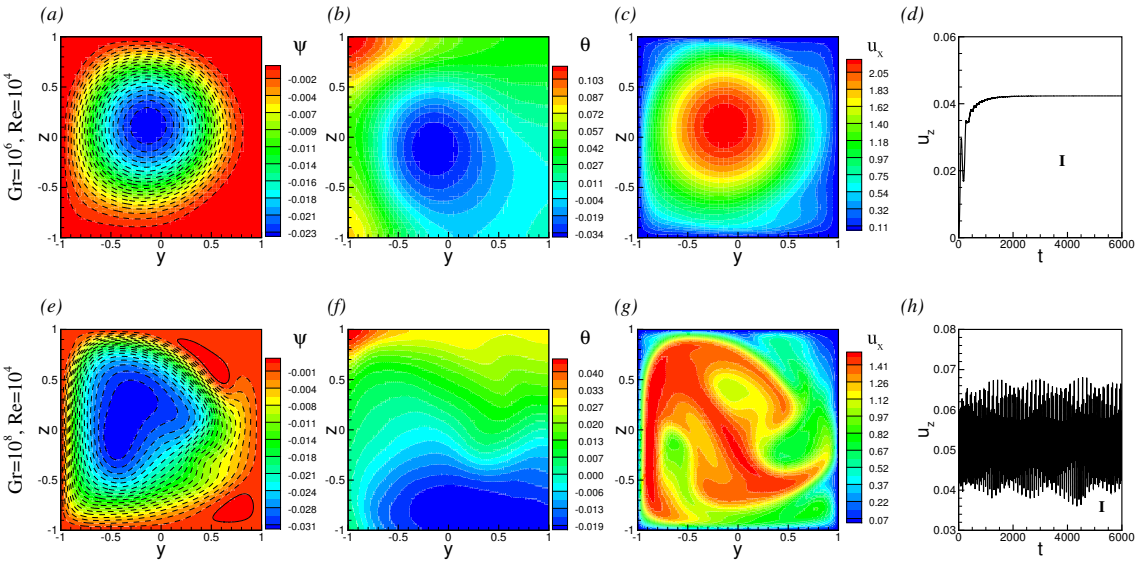

Figure 5.2: Instantaneous distributions of streamfunction Ψ (solid lines indicate counter-clockwise motion, while dashed lines indicate clockwise motion), temperature fluctuation θ and amplitude of velocity u_x. The time signals of vertical velocity u_z are $y = -0.7, z = 0$ is also shown. Flow at $Gr = 10^6$, $Re = 10^4$ is shown in *(a)-(d)*. Flow at $Gr = 10^8$, $Re = 10^4$ is shown in *(e)-(h)*. Flow type (Regime I or II) is indicated in *(d)* and *(h)*.

'developed convection' (type I) (for example, Fig. 5.2) and 'suppressed convection' (type II) (for example, Fig. 5.3a-d). The typical features of each regime are discussed in this section.

The flow is steady-state or quasi-periodic at low *Gr*, such as $Gr = 10^6$, as indicated by the time signal of u_z in Fig. 5.2d. There is one big convection roll generated by internal heating, and the driven streamwise velocity shows the profile similar to that in a hydrodynamic duct flow (see Fig. 5.2c). As *Gr* increases, convection structure becomes stronger, which can be proved by $E_\perp$ in table 5.2. Also, the profile of u_x is disturbed and mixed by the transverse convection (see Fig. 5.2g). The main factor that determines the flow at low *Gr* is the buoyancy force associated with the temperature fluctuation field θ. In the governing equations, we find that, in addition to the conventional balance between the streamwise pressure gradient and the viscous stresses, the amplitude of the buoyancy force (5.7) is pro-

portional to $GrRe^{-2}$, and it tends to generate possibly turbulent circulation in the y-z-plane. We call the flow regime illustrated in Fig. 5.2 flow Regime I. It is characterized by developed convection flow in the transverse plane. The kinetic energy of the transverse velocity $E_\perp$ is relatively high (see table 5.2). From the table 5.2 we can see that not only flows at low *Gr* numbers but also some flows at moderate *Re* and high *Gr* are of this regime. For the temperature distribution, at low *Gr*, there is hot spot at the top left corner of the duct as a result of developed transverse convection (see Fig. 5.2b,f).

No turbulence is generated at low *Gr* since the strength of internal heating is not intense enough.

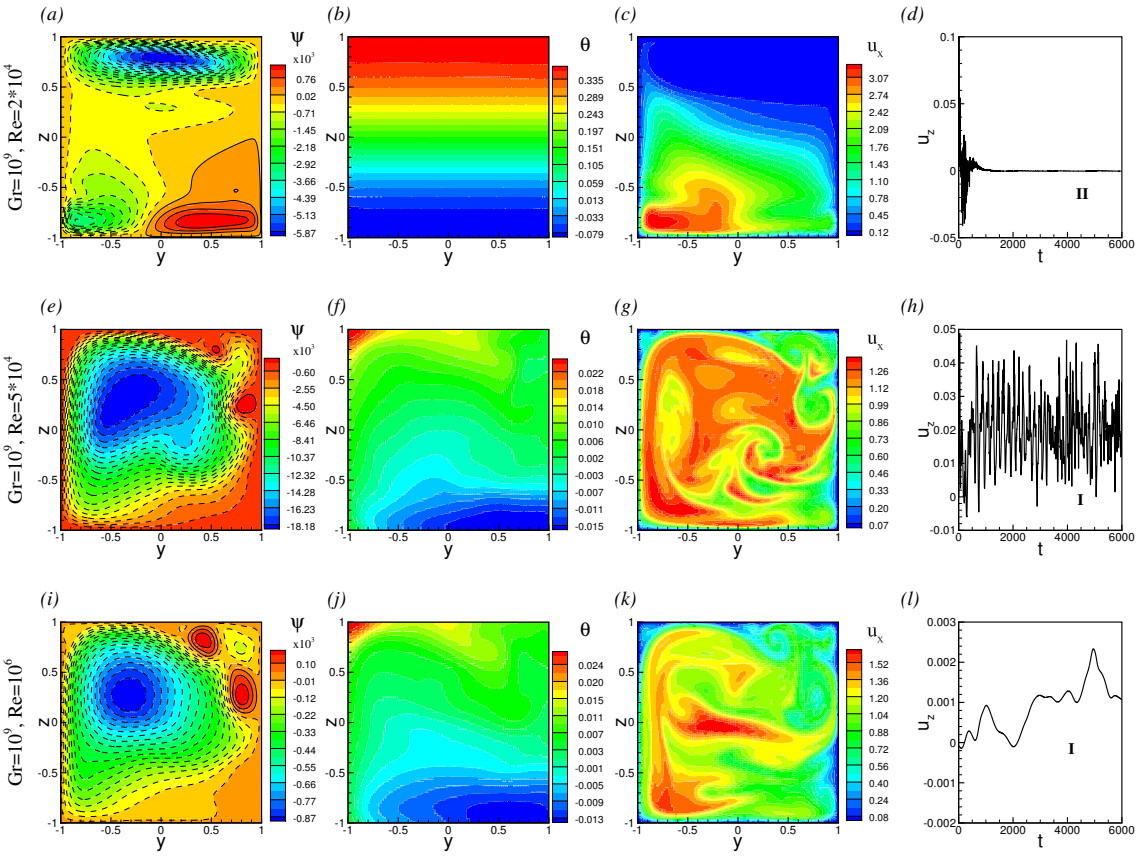

Figure 5.3: Instantaneous distributions of streamfunction Ψ (solid lines indicate counter-clockwise motion, while dashed lines indicate clockwise motion), temperature fluctuation θ, and amplitude of velocity u_x. The time signals of vertical velocity u_z at $y = -0.7, z = 0$ are also shown. Flows at $Gr = 10^9$ and $Re = 2 \times 10^4$, 5×10^4, and 10^6 are shown in, respectively, *(a)-(d)*, *(e)-(h)*, and *(i)-(l)*. Note that the typical time scales used to obtain the nondimensional time t are different for different *Re*. Flow type (Regime I or II) is indicated in *(d)*, *(h)* and *(l)*.

At high *Gr* numbers, flow is influenced by two factors. In addition to the convection caused in the transverse plane by the temperature perturbations θ, the flow becomes strongly affected by the convection effects associated with the mean-mixed temperature. The case, when the latter effect dominates, is illustrated in Fig. 5.3a-d. We call such flows Regime II or the state with suppressed convection. An explanation of development of such states is as follows. As the walls are insulated, and heat is transported by the mean flow with the gradient (5.6), the mean flow temperature increases linearly as a function of the

x-coordinate. Thus, the mean temperature can increase faster at higher *Gr*. The corresponding axial force $\partial\tilde{p}/\partial x$, as described by (5.12), tends to accelerate flow in the lower half of the duct and slow it down in the upper half. The direct result of this buoyancy effect associated with growing T_m is the top-bottom asymmetry of the flow, which is illustrated by the profile of streamwise velocity in Fig. 5.3c. We have very strong forward flow in the lower half of the duct, while the upper half flow is slowed down and can, in the extreme cases, even become a reversed flow. Another result of the buoyancy force associated with the mean-mixed temperature can be seen in Fig. 5.3b. As a consequence of the asymmetric velocity u_x, the heat transfer in the streamwise direction is stronger in the lower part than in the upper part of the duct. This makes the upper part hotter than the lower part. If the flow is not driven fast enough at high *Gr*, the effect can be very strong and make the flow noticeably stably stratified.

This effect can be observed in table 5.2 by comparing $\dfrac{QGr}{ARe^3Pr}$ and $\dfrac{d\hat{p}}{dx}$. The Regime II appears when $\dfrac{QGr}{ARe^3Pr}$ is close to or larger than $\dfrac{d\hat{p}}{dx}$. In this case, the buoyancy effect associated with $T_m(x)$ is strong, the flow becomes stably stratified and its structure changes accordingly (see, for example, Fig. 5.3a,d). The temperature difference between the top and bottom walls becomes significantly higher (see Fig. 5.3b and table 5.2).

If *Re* is sufficiently high to secure Regime I, the fields of non-dimensional u_x and θ do not change much with *Re*(see Figs. 5.3e-h and 5.3i-l). At the same time, $E_\perp$ decreases at higher *Re* (see table 5.2), which indicates weaker convection. An explanation can be seen from the simiplified balances between the transverse transport by the convection flow and viscous or conductive transport

$$(Re\boldsymbol{u}_\perp)\cdot\nabla_\perp u_x = \nabla^2 u_x, \tag{5.18}$$

$$(Re\boldsymbol{u}_\perp)\cdot\nabla_\perp \theta = \nabla^2 \theta. \tag{5.19}$$

where the index of $\perp$ represents in the transverse plane. In our units, larger *Re* implies

that proportionally smaller transverse velocity is needed to achieve the same change of u_x. Increase of *Re* and *Pe* reduces $\boldsymbol{u}_\perp$, but, apparently, keeps the effect about the same.

The time signal of the vertical velocity u_z at various *Re* indicates that the flow becomes more chaotic as *Re* increases, which is expected. Flow changes from steady state (see Fig. 5.3d) to oscillating flow with several dominating frequencies (see Fig. 5.3h), and to a unsteady and less periodic flow at much higher Reynolds number $Re = 10^6$ (see Fig. 5.3l). It is hard to be more specific here, because, it is difficult to do the spectral analysis of the flow at moderate *Gr* and high *Re*. The reason is that the typical time of the convection flow defined as $t_{conv} = \frac{\sqrt{\kappa}}{\sqrt{\beta g q_0 d}}$ (see [4]) has the non-dimensional form $\tilde{t}_{conv} = \frac{t_{conv} U}{d} = ReGr^{-1/2}$, which can be very large. Simulations need to be ran for very long time to get enough data for accurate spectral analysis of the flow.

Fig. 5.4 illustrate the effect of increasing *Gr*, at the same *Re* ($Re = 5 \times 10^5$). The flow is more stability stratified at higher *Gr*, and convection structure and u_x profile are quite different from the low-*Gr* regime. Effect of $\tilde{p}(x, z)$ is strong, as we can see that the temperature field is modified significantly in Fig. 5.4f and Fig. 5.4j. The convection rolls are smaller and relocated to lower half of the duct. The magnitudes of the streamfunction indicate that the circulation is much weaker at higher *Gr*. The u_x profile has strong jet near the bottom. The upper half of duct is not properly cooled due to the stable stratification effect. The temperature difference between the top and bottom walls is large and heat and mass transfer is ineffective in the upper half of the duct.

No developed turbulence is found. In some cases, the signals look chaotic (see Figs. 5.3h and 5.4l), but the spectra (see Figs. 5.5a and 5.5c) do not show the behavior typical for 'fully developed' 2D turbulence [59].

The power energy spectra (4.14) of two typical flows at $Gr = 10^9$ $Re = 5 \times 10^4$ and $Gr = 10^{11}$, $Re = 5 \times 10^5$ are discussed because they are representative of the two flow regimes and their time signals appear more chaotic than other cases (see Figs. 5.3h and 5.4l). So if there is any turbulent flow of this model, these two are the most likely cases.

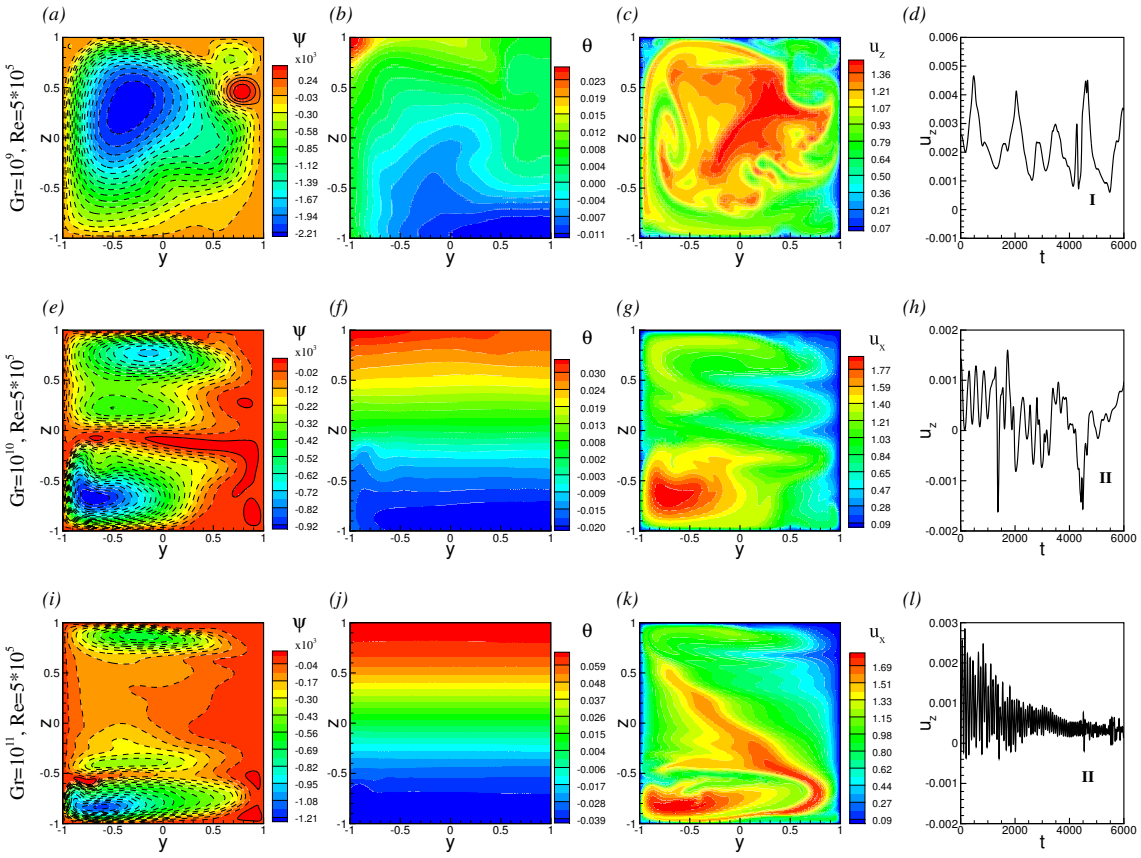

Figure 5.4: Instantaneous distributions of streamfunction Ψ (solid lines indicate counter-clockwise motion, while dashed lines indicate clockwise motion), temperature fluctuation θ, and amplitude of velocity u_x. The time signals of vertical velocity u_z at $y = -0.7, z = 0$ are also shown. Flows at $Re = 5 \times 10^5$ and $Gr = 10^9$, 10^{10}, and 10^{11} are shown, respectively, in *(a)-(d)*, *(e)-(h)*, and *(i)-(l)*. Flow type (Regime I or II) is indicated in *(d)*, *(h)* and *(l)*.

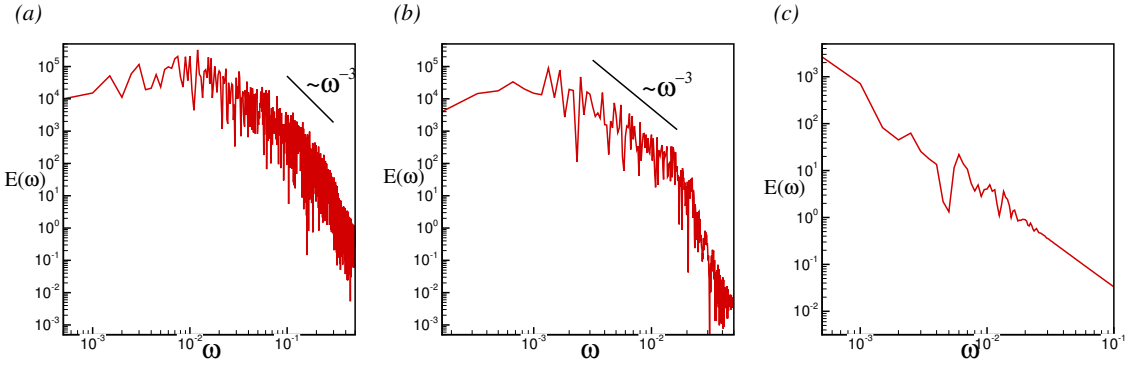

Figure 5.5: Power energy spectra (in log-scale) at $Gr = 10^9$, $Re = 5 \times 10^4$ *(a)*, at $Gr = 10^9$, $Re = 5 \times 10^5$ *(b)* and $Gr = 10^{11}$, $Re = 5 \times 10^5$ *(c)*.

The spectrum of the flow at $Gr = 10^9$ $Re = 5 \times 10^4$ in Fig. 5.5a has a continuum of active frequencies with a small portion following $E \sim \omega^{-3}$. We identify this as weak turbulence. The spectrum of the flow at $Gr = 10^{11}$, $Re = 5 \times 10^5$ in Fig. 5.5c consists of only a few frequencies, so the flow is not turbulent.

We have found that the flow type is not determined by a single parameter group such as $GrRe^{-3}$ or $GrRe^{-2}$, or by the ratio of the amplitude of $\partial\tilde{p}/\partial x$ (3rd column in table 5.2) to the driving pressure gradient $d\hat{p}/dx$. Rather, the flows at low-to-moderate Grashof numbers ($Gr \leq 10^9$, with an exception of the special case $Gr = 10^9$, $Re = 2 \times 10^4$) are all of the developed convection type. The flows at $Gr \geq 10^{10}$ are all of the suppressed convection type.

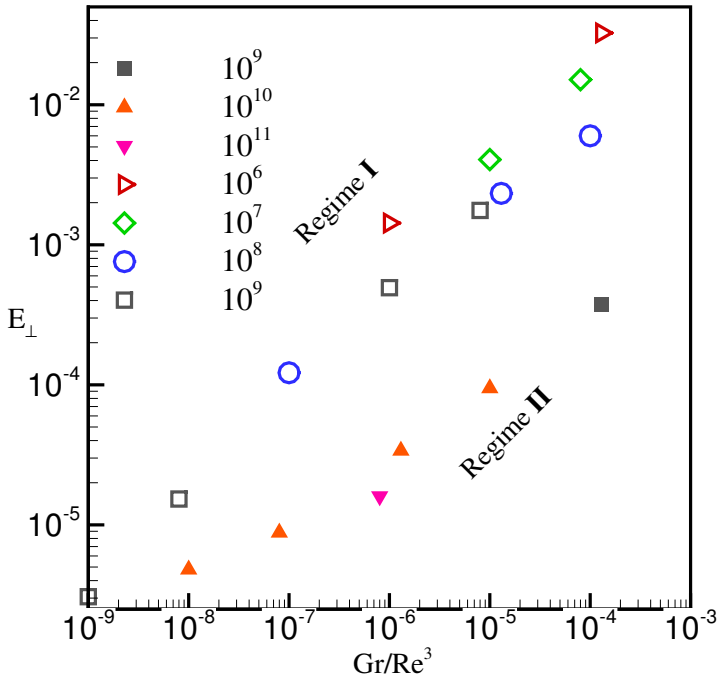

Figure 5.6: Relationship between the transverse kinetic energy $E_\perp$ and Gr/Re^3. Data of all the flow simulations (see table 5.2) are shown. Unfilled and filled symbols represent, respectively, the flows with developed (Regime I) and suppressed (Regime II) transverse convection [5].

However, the parameter $GrRe^{-3}$ can be used to roughly classify the flow regimes, as shown in Fig. 5.6. The transverse kinetic energy $E_\perp$, which indicates the strength of transverse convection, correlates reasonably well with $GrRe^{-3}$. The two regimes of the flow lie on two branches in the chart. This suggests that the flow at very high *Gr* (close to the fusion reactor conditions) are likely to be on the branch of Regime II, which is with the transverse convection suppressed.

The effect of suppression of thermal convection by the buoyancy force associated with the mean temperature is new and unexpected one. It is interesting to estimate the forces involved in this effect for the typical reactor blanket conditions. With the definition (5.5) of the mean-mixed temperature and using the heat balance in a segment of the duct of length L, one obtains:

$$A \times U_m \times \Delta T_m \times \rho \times C_p = Q \times L \tag{5.20}$$

where all the variables are dimensional, C_p is the specific heat of the liquid metal flow, Q is the internal heating rate per unit length calculated as $Q = \int_A q_0 q(y) dA = 2(1 - e^{-2})d^2$. Taking the flow at $Gr = 10^{11}$, $Ha = 10^4$, and $Re = 5 \times 10^5$, using the duct half-width $d = 10\ cm$, length $L = 2\ m$ and the fluid properties at 625 K [6], we find $\Delta T_m = \frac{Gr}{Re} \times \frac{1}{Pr} \times \frac{\nu^2}{g\beta d^4} \times \frac{2(1-e^{-2})d^2}{4d^2} \times L = 2.3\ K$. The buoyancy force arising due to this growth of mean-mixed temperature is $\tilde{F}_b = \rho g \beta \Delta T_m = 23.8\ N/m^3$. The corresponding pressure gradient $\partial\tilde{p}/\partial z = \tilde{F}_b = 23.8\ N/m^3$ and thus the maximum vertical pressure difference in the flow is $\Delta\tilde{p} = 23.8 \times 0.2 = 3.5\ Pa$. It is not a large pressure difference at first glance, but we should compare it with the driving flow gradient. In a viscous flow in a duct, assuming the flow is laminar, the friction coefficient $C_f = \frac{2\tau_w}{\rho U^2} = 14/Re_D$ [71] and thus the shear stress is $\tau_w = \rho U^2 \frac{7}{2Re} = 65.8\ mPa$. Applying the force balance we find $\Delta P_{friction} = \frac{1}{A}\tau_w A_{side} = \frac{1}{0.04} \times \tau_w(0.2 \times 2 \times 4) = 2.632\ Pa$. It is obvious that the $\tilde{p}$ is comparable and even more significant than the friction pressure gradient. Thus, though 2.3 K is a small value of temperature increase, the buoyancy force associated with it is quite

significant.

5.4.2 Stability Analysis

Three-dimensional simulations were performed at $10^9 \leq Gr \leq 10^{11}$, and $10^4 \leq Re \leq 5 \times 10^5$ to test the validity of our two-dimensionality assumption. Only flows with very strong magnetic field close to the real tokamak reactor conditions are considered. Thus very large Hartmann number $Ha = 10^4$ was used in all the cases except one case at $Gr = 10^9$, $Ha = 5000$ and $Re = 10^6$, in which the effect of magnetic field strength was studied. The length of the duct was taken as 4π and the inlet-exit conditions were periodic. Similar to the procedures in Chapter IV, we took the two-dimensional solutions as base states and added three-dimensional random perturbations. The flow evolutions were computed for long periods of time (at least 1000 time units) until the flow converged to a fully developed 3D state (the case of instability) or reverted to a 2D state (the stable case).

The flow regimes found in the 3D simulations are illustrated in Figs. 5.7-5.12. For each case, we show the distributions of the temperature fluctuations θ, the streamwsie velocity u_x in the transverse plane, vertical velocity u_z in the mid vertical plane at $y = 0$, and the temperature fluctuations θ in the mid vertical plane at $y = 0$. Figs. 5.7 - 5.9 show the flows obtained at moderately high Grashof number $Gr = 10^9$. The flow with very strong streamwise velocity at $Re = 10^6$ and $Ha = 10^4$ is shown in Fig. 5.7, while Fig. 5.8 shows the flow at the same Reynolds number $Re = 10^6$ but lower Hartmann number $Ha = 5000$. Flow with low streamwise velocity at $Re = 2 \times 10^4$ is shown in Fig. 5.9. In Figs. 5.10-5.12, flows at high Grashof number $Gr \geq 10^{10}$ and reasonably high Reynolds number $Re = 5 \times 10^5$ are shown.

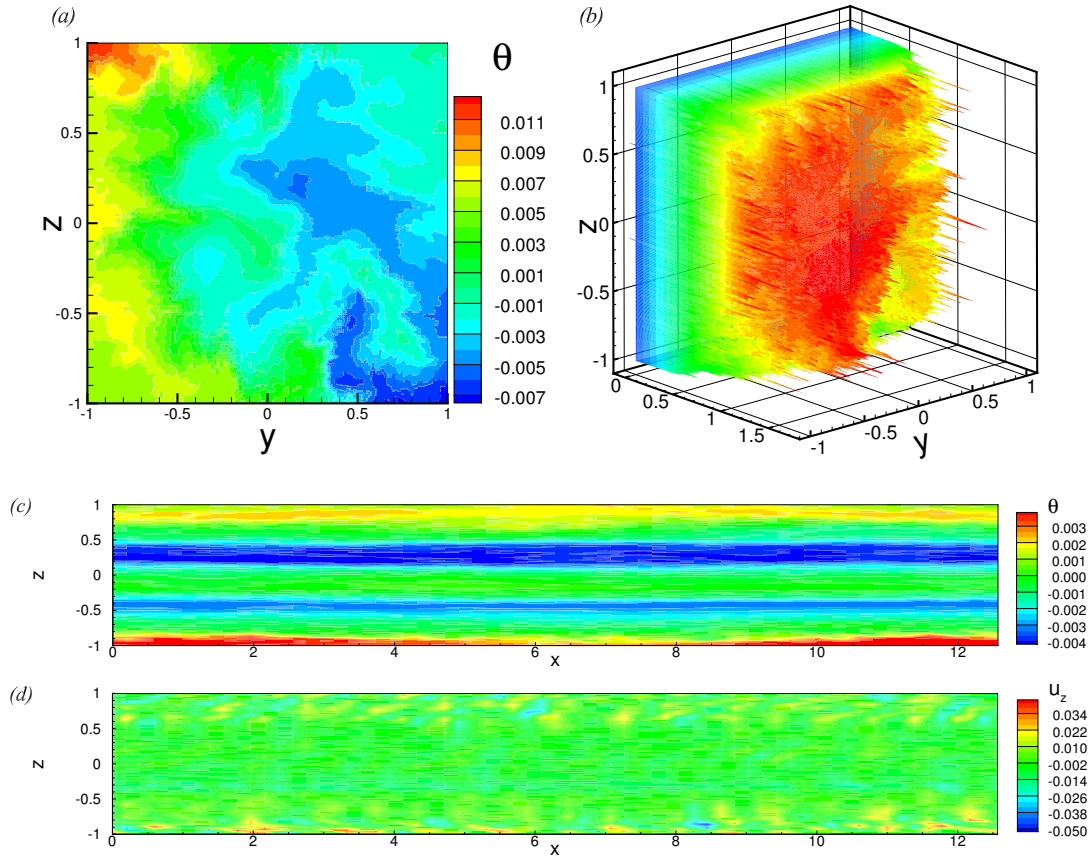

Figure 5.7: Results of 3D simulations at $Gr = 10^9$, $Ha = 10^4$ and $Re = 10^6$. Temperature fluctuation θ and streamwise velocity u_x in the transverse plane *(a)-(b)*, temperature fluctuation θ and distributions of vertical velocity u_z in the vertical plane at $y = 0.5$ *(c)-(d)*.

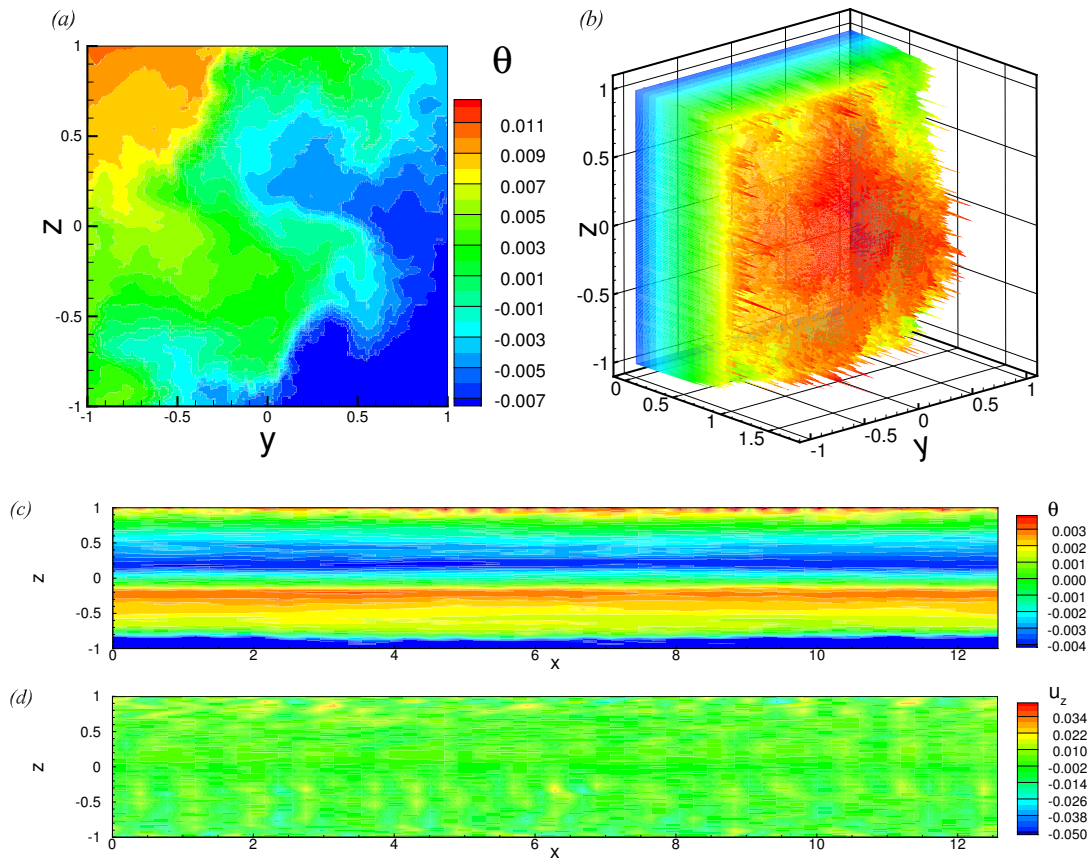

Figure 5.8: Results of 3D simulations at $Gr = 10^9$, $Ha = 5000$ and $Re = 10^6$. Temperature fluctuation θ and streamwise velocity u_x in the transverse plane *(a)-(b)*, temperature fluctuation θ and distributions of vertical velocity u_z in the vertical plane at $y = 0.5$ *(c)-(d)*.

In the cases of developed convection (Regime I), the flow is found to be always unstable to 3D perturbations (see Figs. 5.7-5.8). The flow of Regime I at $Gr = 10^9$, $Ha = 10^4$, $Re = 10^6$ is shown in Fig. 5.7. The profile of streamwise velocity indicates that large convection structures break down into small-scale structures, and it is chaotic in the transverse plane. Although the circulation structures change, the temperature field maintains the distribution similar to that in the 2D solutions. There are hot/cold spots in the corners of the duct. Compared to the 2D solution shown in Fig.5.3j, the temperature difference has decreased by about 50%, which we attribute to the better mixing effect of the 3D flow. Additionally, the cross-section in Fig. 5.7c shows that the flow has 3D structures developed with the

typical length of about 1.5. These 3D structures are located near the top and bottom walls. There are jets of u_x in the 3D region near the bottom wall, and the shear layers formed between the velocity jets and bottom wall may be the reason of the onset of instability.

Also, the effect of strength of magnetic field is studied. Flows at the same *Gr* but different Hartmann numbers are compared in Figs. 5.7-5.8. It shows that increasing *Ha* makes the flow closer to two-dimensionality. The 3D structures are suppressed as shown by their lower kinetic energy. The temperature difference between the top and bottom walls is also reduced at higher *Ha*.

In the cases of suppressed convection (Regime II), after adding 3D perturbations, the flow shows good two-dimensionality with quite weak 3D features (see Fig. 5.9). The flow of Regime II at $Gr = 10^9$, $Ha = 10^4$ and $Re = 2 \times 10^4$ has stably stratified temperature distribution in 2D solutions due to the modification by the buoyancy force associated with the growing mean temperature. We have expected that these flows would be stable to 3D perturbations. However, they turn out to be unstable as well. As one can see in Fig. 5.9, the temperature distributions and streamwise velocity profiles in the transverse plane both indicate small structures formed after adding the 3D perturbations. The temperature and velocity fields are tilted by these structures (see Fig. 5.9a). In the x-z plane, the distribution of the vertical velocity indicates an unstable mode similar to the mode found for the 3D solutions of Regime I. However, the fully developed 3D perturbations are not strong enough to modify the global flow structure or change the temperature distribution significantly or reduce the temperature gradient in the walls. In fact, the overall temperature distribution remains similar to that in the 2D solutions, which means that the 2D result predicts the temperature field accurately. So, the 2D model does not exactly produce the flow structure but predicts the integral properties of the flow well for the flows of Regime II.

In summary, the 2D flows are always unstable, but the intensity of 3D perturbations is higher in flows of Regime I, and lower in flows of Regime II.

As we described in the two-dimensional study, in the most interesting cases of high

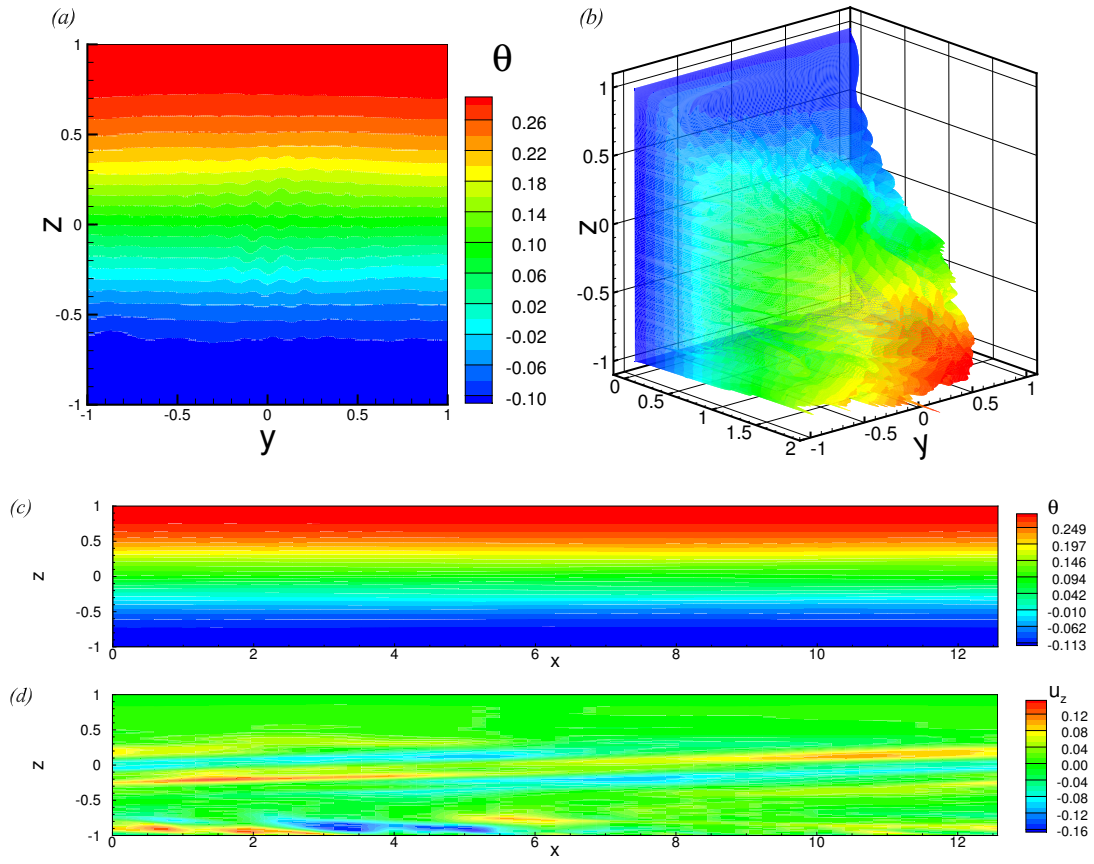

Figure 5.9: Results of 3D simulations at $Gr = 10^9$, $Ha = 10^4$ and $Re = 2 \times 10^4$. Temperature fluctuation θ and streamwise velocity u_x in the transverse plane *(a)-(b)*, temperature fluctuation θ and distributions of vertical velocity u_z in the vertical plane at $y = 0.5$ *(c)-(d)*.

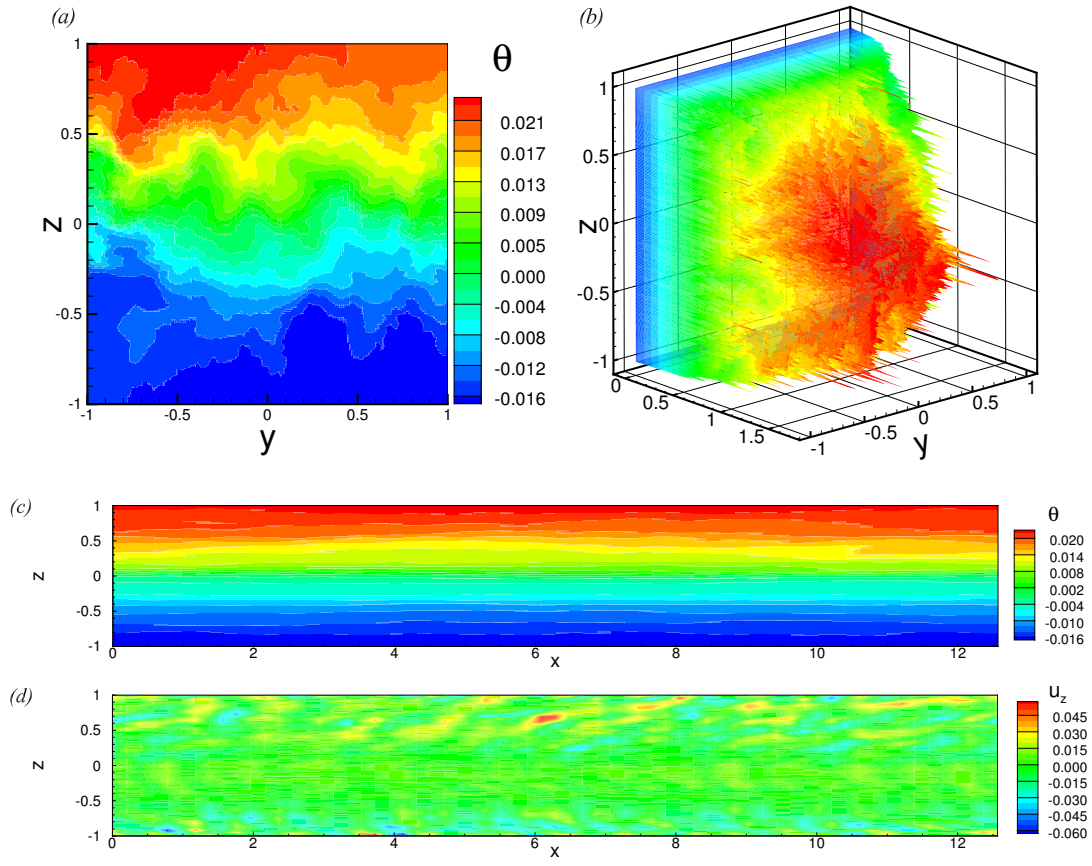

Figure 5.10: Results of 3D simulations at $Gr = 10^{10}$, $Ha = 10^4$ and $Re = 5 \times 10^5$. Temperature fluctuation θ and streamwise velocity u_x in the transverse plane *(a)-(b)*, temperature fluctuation θ and distributions of vertical velocity u_z in the vertical plane at $y = 0.5$ *(c)-(d)*.

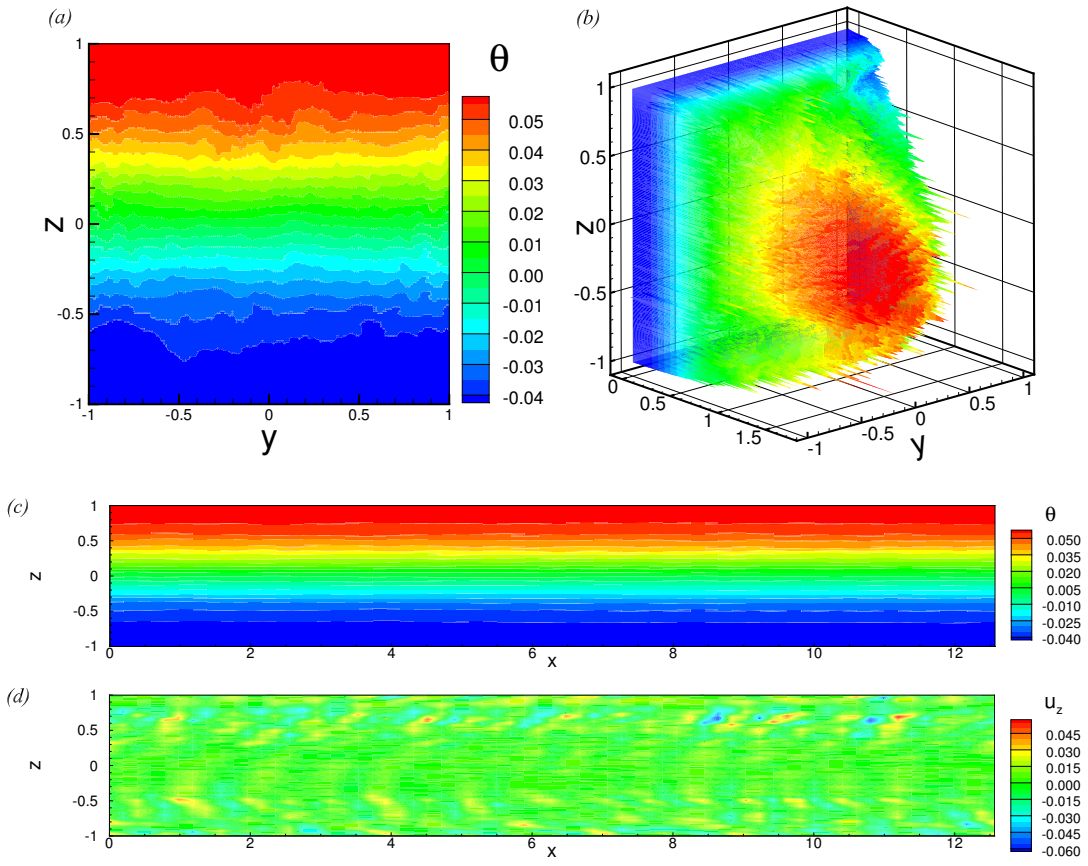

Figure 5.11: Results of 3D simulations at $Gr = 10^{11}$, $Ha = 10^4$ and $Re = 5 \times 10^5$. Temperature fluctuation θ and streamwise velocity u_x in the transverse plane *(a)-(b)*, temperature fluctuation θ and distributions of vertical velocity u_z in the vertical plane at $y = 0.5$ *(c)-(d)*.

$Gr \geq 10^{10}$, the flow is always with suppressed convection in the transverse plane, which is classified as the 'Regime II'. 3D simulations of these flows produce results qualitatively similar to the results found for Regime II at $Gr = 10^9$, (see Figs. 5.10-5.11). That is, the temperature field is quite similar to what we find in the 2D simulations, and the temperature difference between top and bottom walls predicted in the 2D model is verified in the 3D model. Flow is unstable to 3D perturbations but, even when fully developed, they are weak and do not change the flow substantially.

The insignificant modification of the temperature field may also be explained by the low Prandtl number of the fluid, i.e. by strong heat conduction. The weak secondary circulations may affect the streamwise velocity profile a little, but practically does not affect the temperature distribution.

In 3D flows, for example, at $Gr = 10^{11}$, $Re = 5 \times 10^5$ and $Ha = 10^4$ as shown in Fig. 5.11, the vector field in the transverse section shows that the large convection cells (though they are weak in 2D solution due to the suppression effect) break down into very small structures. The vertical velocity u_z in the vertical plane x-z shows that flow is three-dimensional, and the wavelength of the unstable mode is not large. Though the Hartmann number is very large here $Ha = 10^4$, the flow is not two-dimensional, or even with large wavelength. The reason is that the typical size of the 3D flow structures in the transverse plane is small. As indicated in [72], under the suppression by magnetic field, the ratio between the typical wavelengths in the directions parallel and perpendicular to the magnetic field is proportional to the square root of the Stuart number $l_\parallel / l_\perp \sim N^{1/2}$. In the case of $Gr = 10^{11}$, $Re = 5 \times 10^5$, $Ha = 10^4$ shown in Fig. 5.11, $l_\parallel / l_\perp \sim 14$, which is not very large. Due to the small value of $l_\perp$, not large $l_\parallel$ is expected.

We note that the breakdown of the large-scale convection structures does not change the integral properties of the flow significantly. The reason is that the transverse circulations, in both 2D and 3D structures, are very weak.

We can see comparing Fig. 5.4j and Fig. 5.11a that the magnitude of temperature de-

creases a little when the flow becomes three-dimensional. However, the temperature is still stably stratified, with large temperature gradient in the walls.

5.5 Conclusions

The 2D simulations have shown that there are two well-defined states in the model of a fully developed two-dimensional flow with volumetric internal heating and insulating walls.

At small to moderate Grashof numbers ($Gr \leq 10^9$), the flow is in the regime of developed convection (Regime I). The flow structure consists of large-scale convection rolls. The mixing effect is strong in the square domain. This regime appears at reasonably high Reynolds numbers (large enough to limit the mean temperature increase to less than several K along the duct length of 2 m). Flow of Regime I is always unstable to three-dimensional perturbations, and the temperature difference in the flow decreases due to better mixing when it becomes 3D.

In the flow with moderate Reynolds numbers, the growth of mean temperature leads to an additional buoyancy force causing the top-bottom asymmetry of the streamwise velocity. The flow's temperature becomes stably stratified. The thermal convection in the transverse plane is suppressed. The mixing effect in the absence of convection is quite weak, and the wall temperature difference between the top and bottom walls is very large. We call this state of the flow the regime of suppressed convection or Regime II. The three-dimensional stability analysis shows that the flows of Regime II are unstable to three-dimensional perturbations. The fully developed 3D flows are chaotic. The temperature distribution is nearly two-dimensional with very weak variation in the streamwise direction. However, the temperature field is always stably stratified with hot upper part and cold lower part, and the temperature variation is always large in the flows at high Gr.

Regime II is the common state of the flows at large Grashof numbers ($Gr \geq 10^9$), i.e. in the more interesting cases approaching the conditions of a fusion reactor. The effect

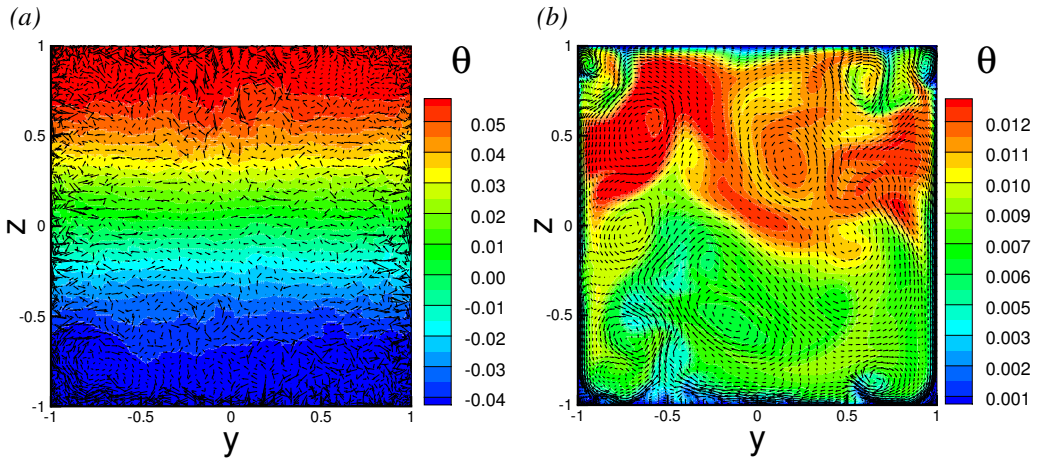

Figure 5.12: Temperature field and vector field in transverse plane of 3D simulations at $Gr = 10^{11}$, $Ha = 10^4$ with mean flow $Re = 5 \times 10^5$ *(a)* and without mean flow $Re = 0$ *(b)*. The boundary conditions for the flow *(b)* are isothermal (a model from Chapter III).

of suppression of the thermal convection in the transverse plane clearly distinguishes the model considered in this chapter from the model of a separately cooled blanket in Chapters III and IV. It strongly affects the operation of the blanket. The most important aspect here is the strong temperature gradient developing in the duct walls. It is clearly seen in Fig. 5.12 that a blanket, in which heat is diverted by the mean flow has significantly larger temperature difference between the top and bottom walls. For example, if we consider a duct of half-width $d = 10\ cm$ and use the material properties of PbLi at 625 K, the difference θ_{top}-θ_{bot} between the average temperature of the top and bottom walls (see table 5.2) can be recalculated as 322 K at $Gr = 10^{11}$, $Re = 5 \times 10^5$. The value remains about the same in the 3D simulations.

The apparent main conclusion of our study is that, at high Grashof numbers typical for the reactor conditions, the thermal convection not only does not promote mixing and uniform temperature in a toroidal duct of a dual-coolant blanket, but leads, via the effect of the streamwise growth of the mean temperature, to potentially damaging temperature gradients within the duct walls.

CHAPTER VI

Downward Flow in Vertical Duct

6.1 Introduction and Configuration

Mixed convection in a downward flow in a vertical duct with one wall heated is considered in this Chapter. The work is motivated by the design of blankets with poloidal ducts, where the ducts in a large part of the blanket are nearly vertical, flow of liquid metal is directed downward in the half of the ducts, and the main component of the magnetic field is perpendicular to the flow direction. An example of such a blanket is the DCLL concept discussed in section 1.1 and illustrated in Fig. 1.4.

The convection in a downward flow in a vertical round pipe and duct has been investigated before both experimentally [23, 32, 25, 68] and numerically [31, 33]. It is an interesting configuration, as the thermal convection is found to be critical for the flow behavior. Large-amplitude low-frequency temperature fluctuations are observed in the flow [32, 25, 68]. Their development is attributed to growth of the 'elevator' instability modes [31, 33]. As in all the flows in pipes and ducts with non-zero mean flow (see, e.g. our discussion in Chapter V), the temperature of the fluid grows along the duct. In the case of a vertical duct with a down ward flow, the fluid becomes hotter in the lower part, i.e., unstably stratified. The associated buoyancy force leads to the convection instability in the form of exponentially growing vertical jets. As shown in [33], the jets are stabilized by the magnetic field, but periodically become unstable and break down into strong vortices.

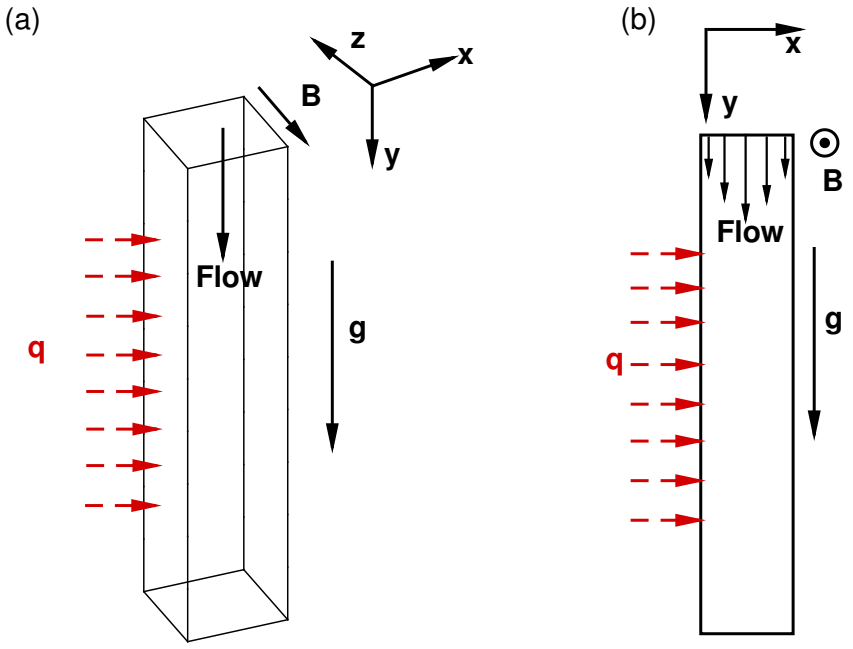

Figure 6.1: Geometry of the flow and the coordinate system for full three-dimensional flow *(a)*, and two-dimensional approximation applied in our study *(b)*. q is the surface heating flux. Heating is only imposed on a part of the wall.

These breakdown events manifest themselves as strong fluctuations of temperature. The previous studies were done either in theoretical manner, or with very idealized inlet-exit condition, or at low *Gr* and *Ha* numbers. To understand the nature of the flow better, we study it with more practical inlet-exit conditions and in a wide range parameters, including the parameters typical for a fusion reactor.

Differently from the previous chapters, we treat the problem as purely two-dimensional. The approach is based on the assumption that the magnetic field is strong enough to suppress the flow variations along the field lines, and that effects of the MHD boundary layers effects can be represented by a linear friction term in the momentum equation as proposed in [49].

The configuration of the flow is shown in Fig. 6.1. Differently from the previous studies of similar systems in [31, 26], the periodic inlet-exit conditions are replaced by the more

realistic conditions with imposed flow at the inlet and free flow at the exit. Buffer layers are added at the inlet and exit to minimize the effect of the boundary conditions and render the model closer to the realistic situation. Heating is modeled as the constant flux applied at one wall, which is the same as was adopted in [31]. There is another reason for using the constant heat flux at the wall instead of volumetric internal heating. By doing that we model the exiting laboratory experiments, in which the internal volumetric heating by absorbed neutrons cannot be reproduced and the heating of the wall by resistive heating elements is applied. Since ours is the first study of such a vertical duct flow with natural inlet-exit condition, we would like to make the model setting closer to the existing experiments, so the results can later be compared with the laboratory results.

6.2 Governing Equations and Boundary Conditions

The governing equations still consist of the conservation of mass, conservation of momentum, and conservation of energy. However, as a very strong magnetic field is imposed perpendicularly to one set of the duct walls, the flow is reduced to a two-dimensional flow with additional magnetic viscous term. We still adopt the quasi-static approximation and Boussinesq approximation. In the asymptotic limit

$$Ha \gg 1, \;\; N > 1, \tag{6.1}$$

the governing equations integrated wall-to-wall along the magnetic field can be simplified to:

$$\nabla \cdot \boldsymbol{u} = 0, \tag{6.2}$$

$$\frac{\partial \boldsymbol{u}}{\partial t} + (\boldsymbol{u} \cdot \nabla)\boldsymbol{u} = -\frac{1}{\rho}\nabla P + \nu \nabla^2 \boldsymbol{u} - \frac{B}{d}\left(\frac{\sigma \nu}{\rho}\right)^{1/2} \boldsymbol{u} + \boldsymbol{F}_b, \tag{6.3}$$

$$\left[\frac{\partial T}{\partial t} + (\boldsymbol{u} \cdot \nabla)T\right] = \frac{\kappa}{\rho c_p}\nabla^2 T, \tag{6.4}$$

where $\boldsymbol{u}$, P, $\boldsymbol{F}_b$ and T are z-averaged field (see [49]). The equations are non-dimesionalized using d, U and $Q_0 d/\kappa$ as the length, velocity and temperature scales, where Q_0 is the typical scale of the constant surface heat flux. The typical scales of time, pressure and magnetic field are d/U, B and ρU^2, respectively. The non-dimensionalized equations are as follows:

$$\nabla \cdot \boldsymbol{u} = 0, \tag{6.5}$$

$$\frac{\partial \boldsymbol{u}}{\partial t} + (\boldsymbol{u} \cdot \nabla)\boldsymbol{u} = -\nabla P + \frac{1}{Re}\nabla^2 \boldsymbol{u} - \frac{Ha}{Re}\boldsymbol{u} + \boldsymbol{F}_b, \tag{6.6}$$

$$\frac{\partial T}{\partial t} + (\boldsymbol{u} \cdot \nabla)T = \frac{1}{Pe}\nabla^2 T, \tag{6.7}$$

The approximation has been verified and examined in [26, 73, 74]. The net Lorentz force is zero as it should in a flow with perfectly insulating walls. The effect of the magnetic field is reduced to its dominant component - the friction in the thin Hartmann layers. In the asymptotic limit (6.1) the friction can, as explained in [49], be accurately modeled by the linear friction term in the momentum equation (6.6). The model was originally developed in [49] for isothermal flows in ducts with electrically insulated walls. It can be easily seen that under the conditions (6.1) the temperature field in non-isothermal problem can also be accurately approximated by a 2D field.

Since the flow is two-dimensional and the fluid is incompressible, we use the streamfunction-vorticity formulation (see, e.g. [75]). The streamfunction ϕ and vorticity ω are defined as

$$u_x = \frac{\partial \psi}{\partial y}, \quad u_y = -\frac{\partial \psi}{\partial x}, \tag{6.8}$$

$$\omega = \frac{\partial u_y}{\partial x} - \frac{\partial u_x}{\partial y}. \tag{6.9}$$

Taking the curl of the momentum equation and expressing velocity components u_x, u_y in the incompressibility condition via the streamfunction, we obtain the equations in the

$\psi - \omega$ formulation:

$$\frac{\partial \omega}{\partial t} + (\boldsymbol{u} \cdot \nabla)\omega = \frac{1}{Re}\nabla^2\omega - \frac{Ha}{Re}\omega + \boldsymbol{F}_b, \tag{6.10}$$

$$\nabla^2\psi = -\omega, \tag{6.11}$$

$$\frac{\partial T}{\partial t} + \boldsymbol{u} \cdot \nabla T = \frac{1}{Pe}\nabla^2 T \tag{6.12}$$

$$\tag{6.13}$$

The non-dimensional parameters are the *Re*, *Ha*, *Pe* as introduced in Chapter II. The combination Ha/Re represents the effect of friction in the MHD Hartmann layers. The buoyancy force is computed as:

$$\boldsymbol{F}_b = -\frac{Gr}{Re^2}\frac{\partial T}{\partial x}. \tag{6.14}$$

For the boundary conditions, walls are considered electrically insulated and no-slip. In a two-dimensional model, with open inlet-exit, only two walls are considered. One wall is subjected to constant heat flux (except the buffer portions near the inlet and exit), and the other wall is thermally insulated:

$$\boldsymbol{u} = j_n = 0 \qquad \text{at } x = \pm 1, \tag{6.15}$$

$$\frac{\partial T}{\partial x} = -1 \qquad \text{at } x = -1,\ \frac{L_y}{6} \leq y \leq \frac{5L_y}{6} \tag{6.16}$$

$$\frac{\partial T}{\partial x} = 0 \qquad \text{at } x = -1,\ y < \frac{L_y}{6}, y > \frac{5L_y}{6} \tag{6.17}$$

$$\frac{\partial T}{\partial x} = 0 \qquad \text{at } x = 1. \tag{6.18}$$

Parabolic velocity profile and isothermal flow are imposed at the inlet. A free flow conditions are applied at the exit:

$$u_x = 0,\ u_y = 1.5(1-x)^2, T = 0 \qquad \text{at } y = 0, \tag{6.19}$$

$$\frac{\partial u_x}{\partial y} = \frac{\partial u_y}{\partial y} = \frac{\partial T}{\partial y} = 0 \qquad \text{at } y = L_y. \tag{6.20}$$

Here, the j_n is wall-normal current and L_y is the non-dimensional duct length $L_y = L/d$.

Small-amplitude random perturbations of velocity and temperature distributed around zero are added to initialize the flow.

6.3 Parameters and Grid

The flow properties are those of the LiPb alloy at 570 K [6]. The Prandtl number is $\mathrm{Pr} = 0.0321$. As a model of a duct in a dual-coolant liquid metal blanket, we study the flows at the Reynolds number $5000 \leq \mathit{Re} \leq 10^5$, the Grashof number $10^6 \leq \mathit{Gr} \leq 10^{10}$ and the Hartmann number $10^3 \leq \mathit{Ha} \leq 10^4$. The non-dimensional duct length is $L = 30$ and $L = 60$.

Uniform grid is used. The numerical resolution is decided on the basis of the grid sensitivity tests. The grids chosen are summarized in table 6.1. The integral characteristics include the average kinetic energy E, thermal energy E_T, averaged mean temperature $\overline{T}$, and the x-averaged temperature in the middle of the duct $T_{ave}(L/2)$:

$$E = \frac{1}{A}\int_A (|u_x|^2 + |u_y|^2)dA, \tag{6.21}$$

$$E_T = \frac{1}{A}\int_A T^2 dA, \tag{6.22}$$

$$\overline{T} = A^{-1}\int_A T dA, \tag{6.23}$$

$$T_{ave} = \frac{1}{2}\int_{-1}^{1} T(x, y = L/2)dx, \tag{6.24}$$

$$\tag{6.25}$$

where A is the area of the rectangle domain.

Gr	Ha	Re	N_x	N_y	L_y
10^8	$10^3 \leq Ha \leq 10^4$	$5000 \leq Re \leq 10^4$	64	600	30
10^8	$10^3 \leq Ha \leq 10^4$	$5000 \leq Re \leq 10^4$	64	1200	60
10^8	$Ha = 1000$	$Re \geq 2 \times 10^4$	96	900	30
10^9	$10^3 \leq Ha \leq 10^4$	$5000 \leq Re \leq 10^5$	96	900	30
10^{10}	$Ha = 10^4$	$5 \times 10^4 \leq Re \leq 10^5$	96	900	30

Table 6.1: Parameters studied and the corresponding numerical resolution.

Gr	Ha	Re	$\frac{Gr}{Re^2}$	$\frac{Ha}{Re}$	$\frac{Ha^2}{Re}$	E	$\overline{T}$	Flow type
10^6	100	500	4.00	0.20	20	3.04	0.451	unstable
10^6	100	1000	1.00	0.10	10	3.03	0.420	steady
10^8	1000	5000	4.00	0.20	200	1.54	0.063	unstable
10^8	1000	10^4	1.00	0.10	100	1.27	0.045	intermittent
10^8	1000	2×10^4	0.25	0.05	50	1.12	0.023	steady
10^8	1000	5×10^4	0.04	0.02	20	1.10	0.006	steady
10^8	5000	5000	4.00	1.00	5000	1.53	0.170	steady
10^8	5000	10^4	1.00	0.50	2500	1.01	0.022	steady
10^8	10^4	5000	4.00	2.00	2×10^4	1.03	0.050	steady
10^8	10^4	10^4	1.00	1.00	10^4	1.00	0.019	steady
10^9	1000	10^4	10.00	0.10	100	2.16	0.031	unstable
10^9	1000	4×10^4	0.625	0.025	25	1.26	0.015	unstable
10^9	1000	5×10^4	0.40	0.02	20	1.16	0.009	intermittent
10^9	1000	10^5	0.10	0.01	10	1.16	0.007	intermittent
10^9	5000	10^4	10.00	0.50	2500	1.40	0.039	unstable
10^9	5000	2×10^4	2.50	0.25	1250	1.21	0.030	unstable
10^9	5000	3×10^4	1.11	0.17	833	1.09	0.018	intermittent
10^9	5000	4×10^4	0.625	0.125	625	1.03	0.007	steady
10^9	5000	5×10^4	0.40	0.10	500	1.03	0.005	steady
10^9	10^4	1.5×10^4	4.44	0.67	6670	1.59	0.102	unstable
10^9	10^4	2×10^4	2.50	0.50	5000	1.13	0.035	intermittent
10^9	10^4	3×10^4	1.11	0.33	3333	1.01	0.008	steady
10^9	10^4	5×10^4	0.40	0.20	2000	1.01	0.004	steady
10^{10}	10^4	5×10^4	4.00	0.20	2000	1.16	0.011	unstable
10^{10}	10^4	10^5	1.00	0.10	1000	1.05	0.005	unstable

Table 6.2: Summary of simulation results. $\frac{Gr}{Re^2}$ is the parameter that measures the strength of the buoyancy effect. $\frac{Ha}{Re}$ represents the strength of the damping effect of the magnetic field. $\frac{Ha^2}{Re}$ is the Stuart number that measures the relative strength of electromagnetic to inertial forces. Volume-averaged kinetic energy E and mean temperature $\overline{T}$ are also averaged in time for unsteady flows.

6.4 Results

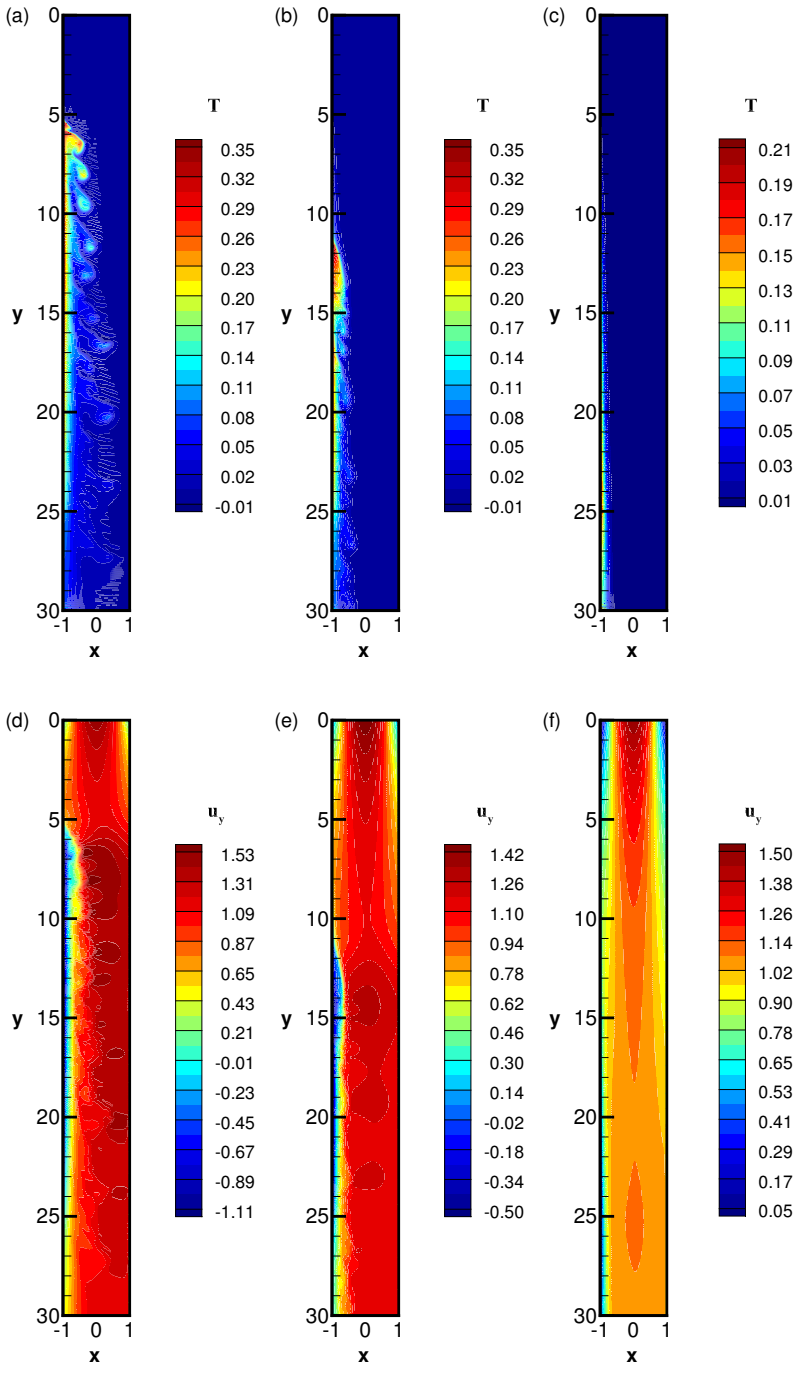

Figure 6.2: Instantaneous distributions of temperature T and amplitude of vertical velocity u_y in the flows $Gr = 10^9$, $Ha = 5000$, $Re = 2 \times 10^4$ *(a),(d)*, $Re = 3 \times 10^4$ *(b),(e)* and $Re = 4 \times 10^4$ *(c),(f)*. Duct length is $L_y = 30$.

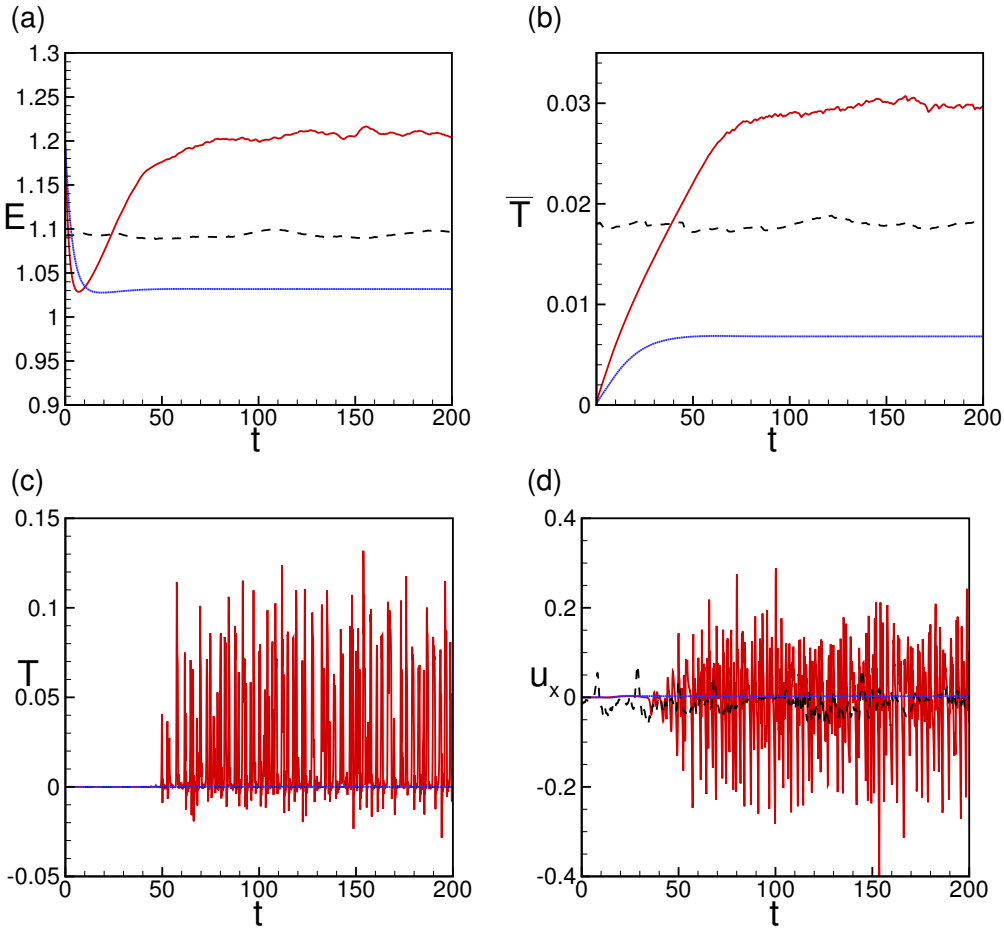

Figure 6.3: Results of the flows at $Gr = 10^9$, $Ha = 5000$, $Re = 2 \times 10^4$ (red, solid lines), $Re = 3 \times 10^4$ (black, dashed lines) and $Re = 4 \times 10^4$ (blue, dotted line). Total kinetic energy *(a)* and mean temperature *(b)* of the flows. Point signals of velocity u_x *(c)* and temperature T *(d)* at the center of the duct. Only parts of actual simulations are shown.

The most extensive studies have been performed at $Gr = 10^8$ and $Gr = 10^9$. The results are summarized in table 6.2. The detailed flow structures and the integral properties at different *Gr*, *Ha* and *Re* are shown in Figs. 6.2-6.10.

Three typical flow regimes: 'unstable', 'intermittent', and 'steady' are identified (see flows at $Gr = 10^9$, $Ha = 5000$ in Fig. 6.2-6.3 as examples). We classify the flow as unstable if the jets are clearly unstable to two-dimensional rolls and the resulting breakdowns of the jets occur continuously in time (see Fig. 6.2a,d). This leads to the time signals of the temperature of velocity in the form of continuous high-amplitude fluctuations (see Fig. 6.3c,d). In such a flow at low-to-moderate Reynolds number $Re = 2 \times 10^4$ in Fig. 6.2a,d, the vertical velocity field shows the unstable mode is of wavelength $\lambda \sim 2$. The wavelength may change with *Gr* and *Re* as illustrated below. The temperature distribution also indicates the developed instability and temperature fluctuations appear in the flow (see red line in Fig. 6.3b,c). At higher Reynolds number $Re = 3 \times 10^4$, the flow is intermittent. The upstream and downstream jets are weaker compared to the unstable regime (see Fig. 6.2d,e). The time signals of the velocity u_x and the analysis of the flow states at various time, show that the instability develops sporadically. Brief events of instability results in partial destruction of the jets. The events are followed by periods when instability does not occur and the jets grow back to full amplitude. An example of such a flow is shown in Fig. 6.3b,e. At large Reynolds number $Re = 4 \times 10^4$, the flow is steady-state. In the vertical velocity u_y field, there is no upstream jet, and the main flow is dominated by the imposed velocity field. In the temperature field, there is temperature growth in a thin layer near the heated wall. The major part of the flow has nearly uniform temperature distribution (see Fig. 6.2c). The integral properties E and $\overline{T}$ decrease as the regime of the flow changes to steady-state (see Fig. 6.3a,b).

There are three non-dimensional parameters considered in the study: *Re*, *Ha* and *Gr*. We then look into the role of each parameter.

We first look at the effect of *Re*. Taking flows in the duct $L_y = 30$ at $Gr = 10^8$ as

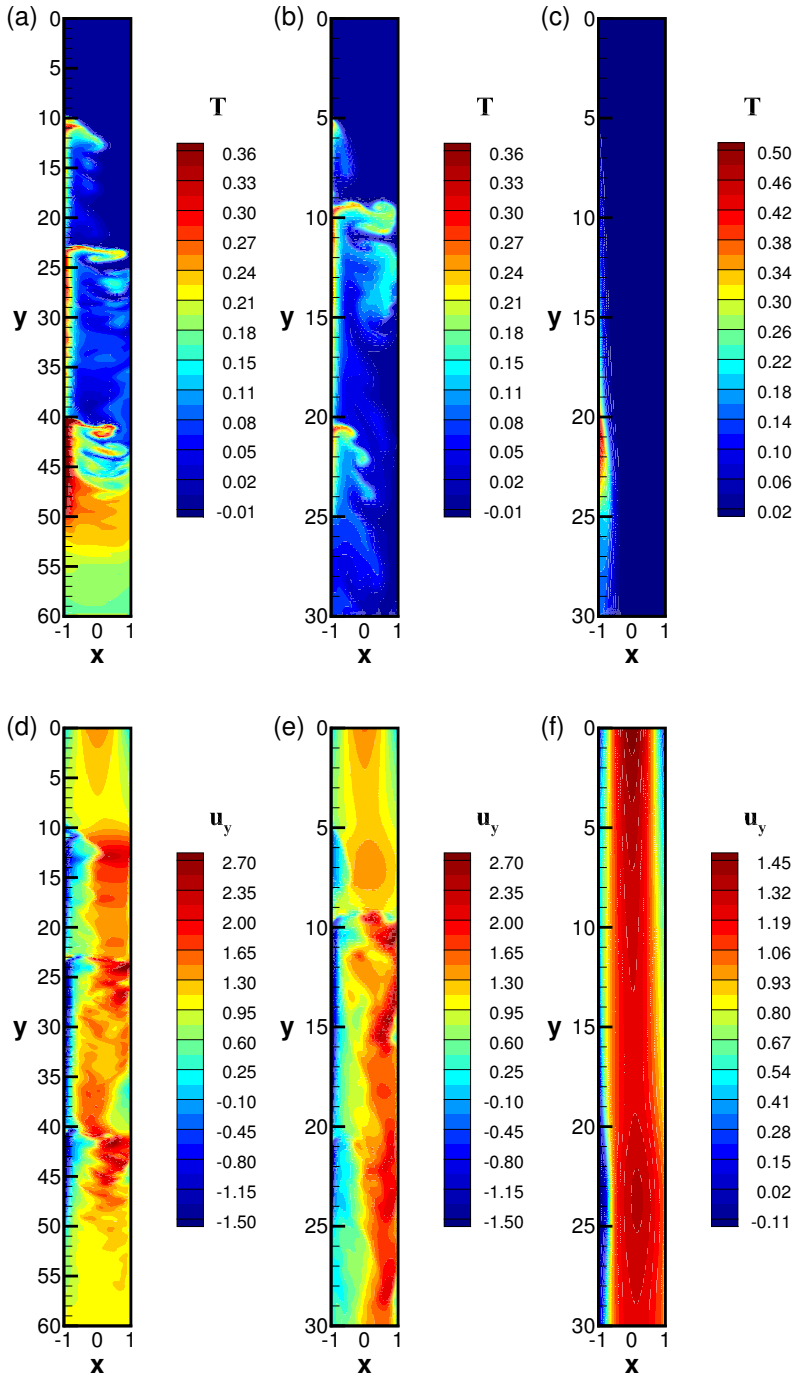

Figure 6.4: Instantaneous distributions of temperature T and amplitude of vertical velocity u_y in the flows at $Gr = 10^8$, $Ha = 1000$, $Re = 5000$, $L_y = 60$ *(a),(d)*, $L_y = 30$ *(b),(e)* and $Gr = 10^8$, $Ha = 1000$, $Re = 2 \times 10^4$, $L_y = 30$ *(c),(f)*.

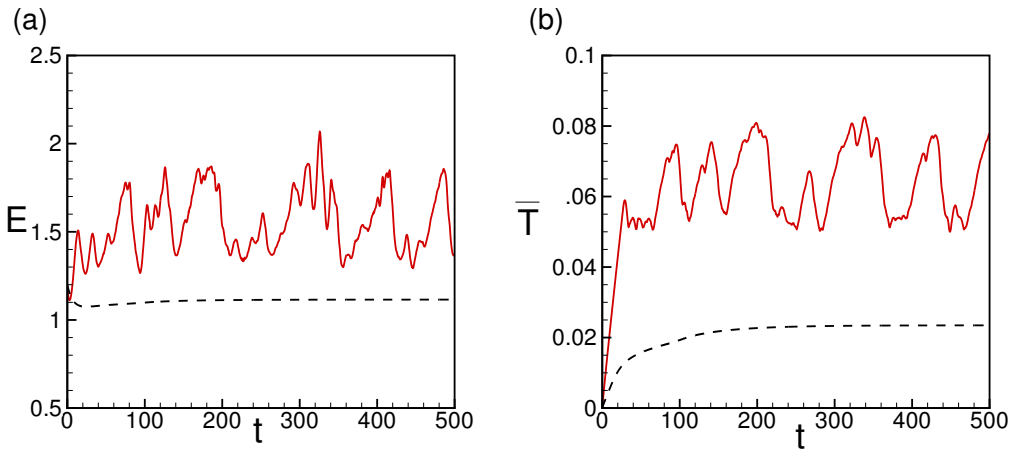

Figure 6.5: Total kinetic energy *(a)* and mean temperature *(b)* in the flows at $Gr = 10^8$, $Ha = 1000$, $Re = 5000$ (red, solid lines) and $Re = 2 \times 10^4$ (black, dashed lines). Only parts of actual simulations are shown.

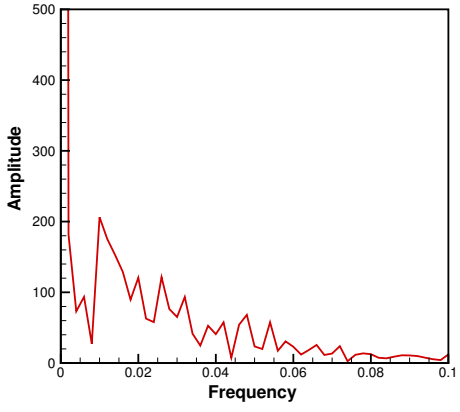

Figure 6.6: Spectral decomposition of total kinetic energy signal $E(t)$ in the flow at $Gr = 10^8$, $Ha = 1000$ and $Re = 5000$.

an example, we see in Fig. 6.4 (middle and right columns) that, the structure of the flow changes significantly when *Re* increases. The flow is unstable with developed instability at $Re = 5000$ and the axial wavelength of the dominating unstable mode is about 10. However, different from the common hydrodynamic flow, increasing *Re* does not lead to stronger and more irregular perturbations. Instead, the flow becomes steady-state with a hot spot at the bottom (see Fig. 6.4c,f), in which the flow at $Re = 2 \times 10^4$ is shown as an example.

The reason to the change of regime is the mechanism of forming the 'elevator modes' mentioned at the beginning of this chapter. The temperature of the flow grows downstream, which creates unstable stratification and, if the effect is strong enough, causes thermal convection in the form of a pair of growing upstream and downstream jets. As discussed in [31, 33], the secondary instability is the reason for irregular structures in the flow.

The sufficiently strong jets develop once the Reynolds number is lower than a critical value. This is because when the flow is driven slowly, due to the heating from the wall, the mean temperature of the flow would grow stronger along the duct, and the buoyancy effect causing the jets would be strong. Increasing *Re* would reduce the mean temperature growth and remove the potential for the jet growth and the flow becomes stable and steady-state. In Fig. 6.4, at moderate Reynolds number $Re = 5000$, when the instability occurs in the flow, hotter fluid particles are moving to the upper part and the large convection structures break into small cells. The distribution of vertical velocity u_y shows a strong upward jet near the heated wall. The average velocity of the upward jet is comparable to velocity of the downward flow. The signals of the integral properties of the two flow states are shown in Fig. 6.5. The total kinetic energy and the mean temperature of the flow decrease when the instability occurs. The Fourier analysis of the total kinetic energy in the flow at $Gr = 10^8$, $Ha = 1000$ and $Re = 5000$ (see Fig. 6.6) shows that, after the flow becomes unsteady, the flow is dominated by several frequencies.

So, in the flows at fixed *Gr* and *Ha*, increasing *Re* will stabilize the flow, i.e., change the

regime from unstable or intermittent to steady-state. There is a critical Reynolds number Re_{cr} below which, instability occurs.

The duct length discussed so far is $L_y = 30$ and we want to know whether the duct length would affect the flow behavior or not. So we have carried out simulations at different duct lengths, and found that the duct length, if taken above 30, does not influence the nature and quantitative properties of the flow structures. The effect of the duct length is illustrated in Fig. 6.4a,d and Fig. 6.4b,e by the flows at $Gr = 10^8$, $Ha = 1000$ and $Re = 5000$. The flow fields in the duct of $L_y = 60$ and $L_y = 30$ are compared. The temperature fields of these two cases are quite similar, and the dominant wavelengths of the unstable modes are nearly the same. The strength of the upward jet is also similar in these two cases. In the steady-state flows in the ducts of different lengths, the flow structures are also similar, except the 'penetrating length' (represents how far the hot jet moving upward and entering the buffer layer) of hotter fluid particles is longer when duct length is larger. This is because the flow in a longer domain is heated more by the wall heating and the corresponding buoyancy effect creating the jets is stronger. But if we compare the relative lengths of the penetrating length to buffer regions, the relative lengths in different domains are similar. The velocity fields also show similar flow structures. The duct length $L_y = 30$ is larger than the wavelength of the dominating unstable mode thus using duct length $L_y = 30$ is sufficient to resolve the flow features. The signals of velocity and temperature of the flow show that increasing the duct length just delays the flow development, thus we choose to study the flows at $L_y = 30$ to reduce the computational cost.

The magnetic field has damping effect on the flow which is represented by the term $(Ha/Re)\omega$ in the momentum equation. Thus Hartmann number *Ha* should also affect the flow behavior. This effect is illustrated in Fig. 6.7. Flows at $Gr = 10^9$, $Re = 10^4$, $Ha = 1000$ and $Ha = 5000$ are compared. These two flows are both unstable with developed instability. The evolutions of the flows to these states are different. Flow develops slower at higher *Ha*. The energy of the flow decreases (see Fig. 6.7a). At higher *Ha*, due to

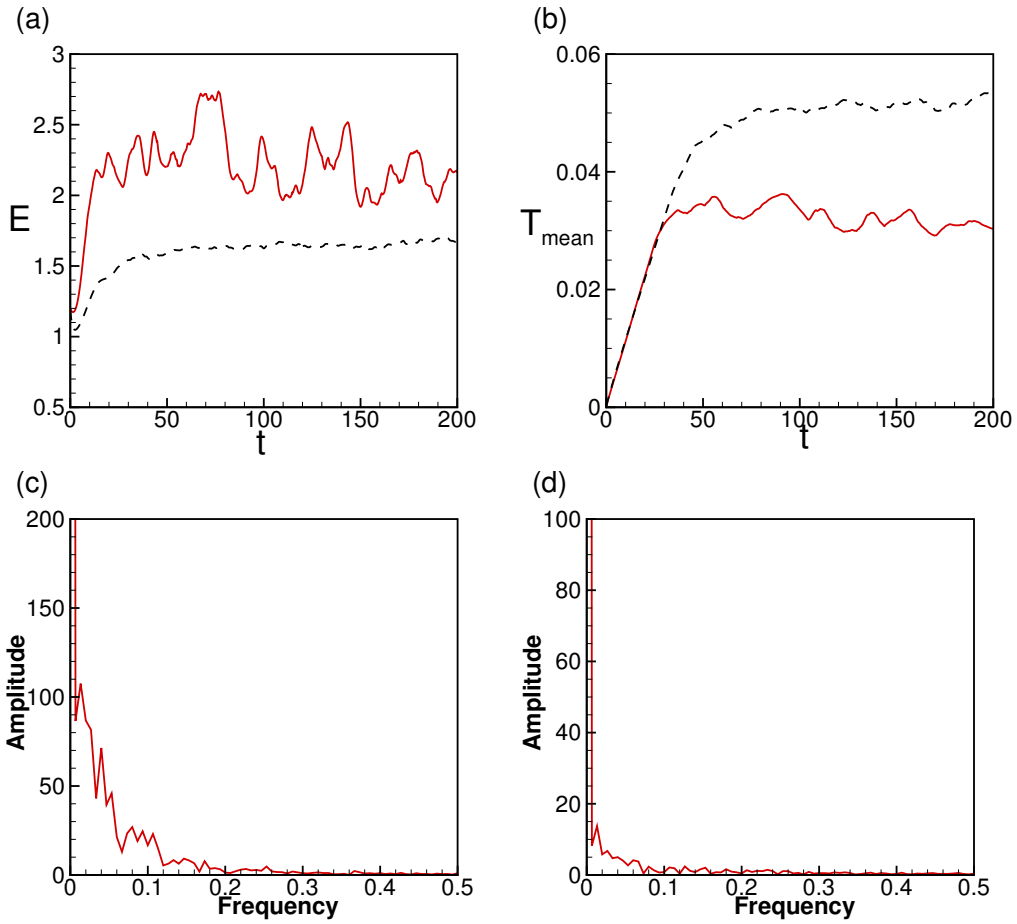

Figure 6.7: Total kinetic energy *(a)* and mean temperature *(b)* in the flow at $Gr = 10^9$, $Re = 5000$ and $Ha = 1000$ (red, solid lines) and $Ha = 5000$ (black, dashed lines). Spectral decompositions of total kinetic energy signal $E(t)$ in the flow at $Gr = 10^9$, $Re = 10^4$, $Ha = 1000$ *(c)* and $Ha = 5000$ *(d)*.

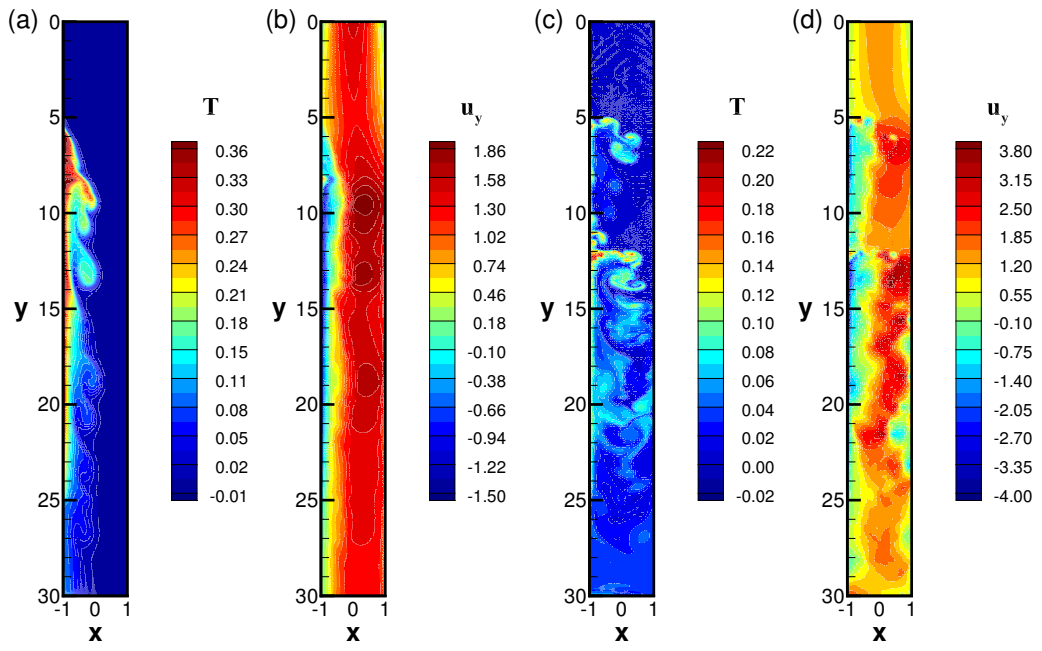

Figure 6.8: Instantaneous distributions of temperature T and amplitude of vertical velocity u_y in the flows at $Ha = 1000$, $Re = 10^4$, $Gr = 10^8$ *(a)-(b)* and $Gr = 10^9$ *(c)-(d)*. Note that the isolevels are different at different *Gr*.

the damping by the magnetic field, the flow has fewer dominating frequencies and the amplitude of the oscillations decreases. The mixing of the flow is less active and the mean flow temperature decreases. Thus we conclude that the *Ha* would affect the development time of the flow, reduce the energy and mean temperature of the flow.

The effect of *Gr* is illustrated by Fig. 6.8 and Fig. 6.10. At the same Hartmann and Reynolds numbers $Ha = 1000$ and $Re = 10^4$, flows at $Gr = 10^8$ and $Gr = 10^9$ are shown in Fig. 6.8. The flow at $Gr = 10^9$ is unstable with developed instability, while the flow is unsteady at $Gr = 10^8$ but its behavior is intermittent. The point signals of the velocity u_x and the temperature T at the center of the duct in Fig. 6.9 illustrate the intermittent behavior clearly. The temperature and velocity fields at $Gr = 10^8$ (see Fig. 6.8a,b) show that the convection structures break down at the top of the upward jet near heated wall at the onset of the instability. The vertical velocity fields (see Fig. 6.8b,d) show that the instability at higher *Gr* generates much stronger and thinner jet near the heated wall.

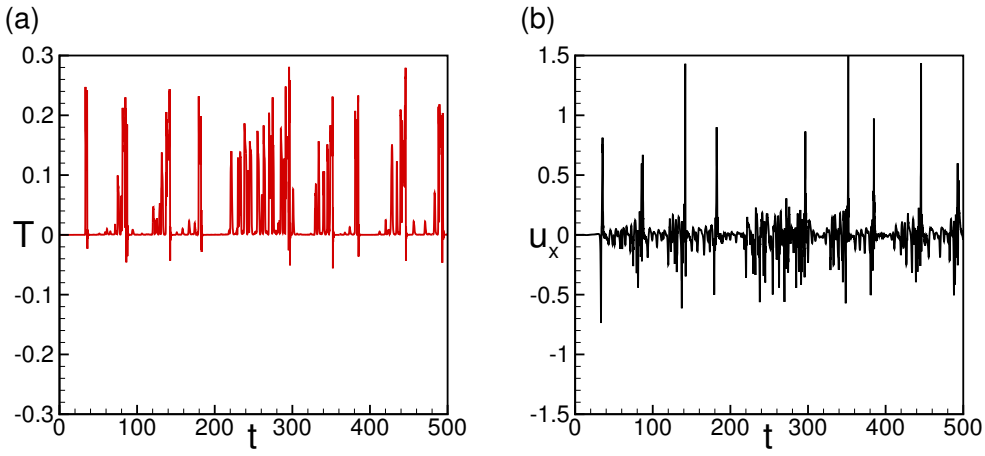

Figure 6.9: Point signals of velocity u_x and temperature T at the center of the duct at $Gr = 10^8$, $Ha = 1000$ and $Re = 10^4$.

As we have mentioned above, the flow at $Gr = 10^9$ is unstable with developed instability, which indicates that the critical Reynolds number Re_{cr} for instability is higher as Gr increases. This is expected, since the buoyancy effect represented by the group parameter Gr/Re^2 requires larger Re to remove the instability potential. However, the simulations in a wide rage of Gr, Ha and Re (see table 6.2) suggest that the critical Re is not simply decided by the Gr/Re^2 or another group parameter. The Ha/Re which represents the damping effect of the magnetic field, would decreases as Re increases. The weaker damping effects would leave the flow more energy to develop the instability. Thus it is incorrect to conclude that Gr/Re^2 solely determines the flow state.

From our previous experience with convection in MHD flow, we expect that the flow regimes are different at low and high Grashof numbers. In order to check this effect, we have picked three cases at $Gr = 10^6$, $Gr = 10^8$ and $Gr = 10^{10}$ and Re and Ha selected in such a way that the non-dimensional groups Gr/Re^2 and Ha/Re remain the same, all with unsteady fully developed instability. They are compared to each other in Fig. 6.10. At $Gr = 10^6$, $Ha = 100$ and $Re = 500$, we can see the unstable mode in the flow is of a large wavelength $\lambda = 15$. The spectrum analysis shows the break-down behavior is of low frequency (see Fig. 6.11). The vertical velocity field shows the strength and width of the

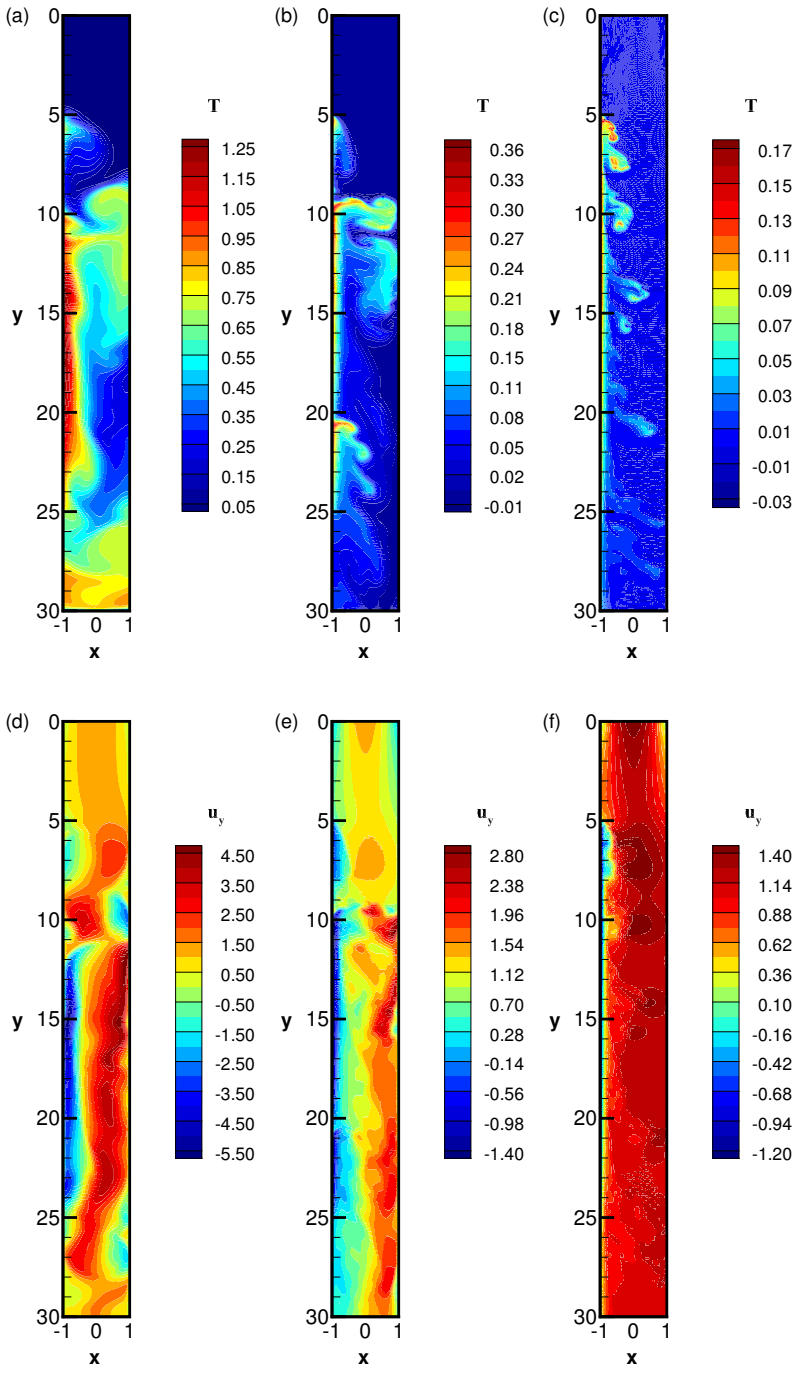

Figure 6.10: Instantaneous distributions of temperature T and amplitude of vertical velocity u_y in the flows at $Gr = 10^6$, $Ha = 100$, $Re = 500$ *(a),(d)*, $Gr = 10^8$, $Ha = 1000$, $Re = 5000$ *(b),(e)* and $Gr = 10^{10}$, $Ha = 10^4$, $Re = 5 \times 10^4$ *(c),(f)*. Note that the isolevels are different at different *Gr*.

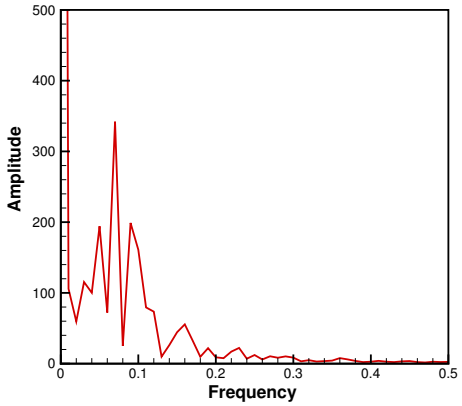

Figure 6.11: Spectral decomposition of total kinetic energy signal $E(t)$ in the flow at $Gr = 10^6$, $Ha = 100$ and $Re = 500$.

upward jet is quite similar to the downward mean flow. As Gr increases, the jet becomes thinner and stronger and the instability is of higher frequency. The results at $Gr = 10^6$ and $Gr = 10^8$ qualitatively match the results from the experiment by [25], where the instability is detected with comparable velocity of the upward and downward flow jets. As we mentioned, the flow behavior at higher Gr is usually different from the low-Gr regime, and we expect the jets change to stronger and thinner at the conditions closer to real blanket condition in a fusion reactor. At $Gr = 10^{10}$, the wavelengths of unstable modes are much smaller, and the revolution of the flow is much faster. The upward jet is very strong and thin near the heated wall.

We tried to summarized the flow states using a chart but as we said, there is no single group parameter determining the flow state. Table 6.2 roughly indicates that the flows at $Gr/Re^4 \sim 1$ or higher and the $Ha/Re \sim 0.1$ or less would have the state of developed instability.

6.5 Conclusions

The study of thermal convection in a downward flow in a vertical duct with one wall heated reveals that the flow can be steady-state, intermittent, or unstable with developed instability depending on the parameters. Duct length above $L_y = 30$ does not affect the flow nature. Higher *Ha* delays the flow evolution and reduces its kinetic energy. The amplitude of the buoyancy force Gr/Re^2 affects the flow in a major way. The flows at low-to-moderate *Gr* have upward and downward jets of approximately the same maximum velocity, and the developed instability are of a large scale and low frequency. The flows at high *Gr* have stronger upward jet near the heated wall, and the convection structures break down into smaller scales leading to higher oscillation frequencies. The flow behavior is determined by the buoyancy effect and the magnetic damping together. There is no clearly identifiable group parameter determining the flow structure.

With very strong heating flux and reasonably fast mean flow, the flow can be unstable with developed instability at the conditions close to the conditions of a fusion reactor. The instability would result in temperature fluctuations, and their frequency would increases as *Gr* increases.

CHAPTER VII

Conclusions

We have studied the thermal convection in the flows within horizontal or vertical ducts with imposed strong magnetic field at the non-dimensional parameters close to the conditions of a blanket of a fusion reactor. The main conclusion is that, *the thermal convection is critical to the state of the liquid metal flow and should always be considered in the design of liquid metal blankets*.

For the model of a separately cooled blanket with toroidal ducts, we find that the results of the previous studies, which did not consider convection, must be viewed as largely incorrect. The commonly accepted assumption of a steady and laminar flow with passive heat transfer in the blanket is wrong. Our results indicate that the flow is turbulent at high Gr with effective heat transfer in the purely toroidal magnetic field. Weak poloidal component of the magnetic field suppresses the turbulence, elongates convection structures and forms near-wall jets. It also forms shear layers in the flow, which results in the flow being more unstable to three-dimensional perturbations. However, the poloidal magnetic field does not affect the heat transfer toward the walls much. The suppressed flow maintains effective heat and mass transfer.

For the model of a dual-coolant blanket with toroidal ducts, the effect of the mean flow is found to be beyond expectations. At high Gr, the flow is dominated by the top-bottom asymmetry of the streamwise velocity and stable stratification of temperature caused by

the buoyancy force associated with the growth of the mean temperature along the duct. The result is the suppression of thermal convection, weak mixing, and substantial gradients of wall temperature. The suppression of the thermal convection in the transverse plane strongly affects the operation of the blanket and causes potentially harmful temperature gradients in the walls. The results lead us to question the concept of a dual-coolant blanket with toroidal ducts.

For the model of a dual-coolant blanket with downward flow in poloidal ducts, three flow regimes: steady-state, intermittent, or unstable with developed instability are identified at different parameters. Effects of *Ha*, *Re* and *Gr* are studied. The structure of the flow is determined by multiple effects. No single parameters determining the flow state is found. In the unstable flows at low-to-moderate *Gr*, the unstable mode is of a large wavelength and low frequency, with comparably strong upstream and downstream jets developing in the flow. In the unstable flows at high *Gr*, upstream jet is much stronger and closer to the heated wall and the dominant frequency of the developed instability increases. The flow at the conditions close to those of a reactor is expected to be unstable with developed instability. As a result of the instability, temperature fluctuations similar to those identified in the previous studies of poloidal ducts are expected to appear.

BIBLIOGRAPHY

[1] S. Smolentsev, R. Moreau, L. Bühler, and C. Mistrangelo. MHD thermofluid issues of liquid-metal blankets: Phenomena and advances. *Fusion Eng. Design*, 85(7-9):1196–1205, 2010.

[2] S. Malang, M. S. Tillack, L. Barleon, S. Baumgärtner, H. U. Borgstedt, L. Bühler, F. Dammel, H. Feuerstein, U. Fischer, K. Gabel, et al. Development of self-cooled liquid metal breeder blankets. *EUR(Luxembourg)*, 1995.

[3] X. Zhang and O. Zikanov. Two-dimensional turbulent convection in a toroidal duct of a liquid metal blanket of a fusion reactor. *J. Fluid Mech.*, 779:36–52, 2015.

[4] X. Zhang and O. Zikanov. Thermal convection in a toroidal duct of a liquid metal blanket. Part I. Effect of poloidal magnetic field. *Fusion Eng. Des.*, 2017. In press.

[5] X. Zhang and O. Zikanov. Thermal convection in a toroidal duct of a liquid metal blanket. Part II. Effect of axial mean flow. *Fusion Eng. Des.*, 2017. In press.

[6] B. Schulz. Thermophysical properties of the Li(17)Pb(83) alloy. *Fusion Eng. Des.*, 14:199–205, 1991.

[7] E. Mas de les Valls, L.a. Sedano, L. Batet, I. Ricapito, a. Aiello, O. Gastaldi, and F. Gabriel. Lead-lithium eutectic material database for nuclear fusion technology. *J. Nucl. Mater.*, 376(3):353–357, 2008.

[8] T. J. Dolan, R. W. Moir, W. Manheimer, L. C. Cadwallader, and M. J. Neumann. *Magnetic fusion technology*. Springer, 2013.

[9] M. Abdou, N. B. Morley, S. Smolentsev, A. Ying, S. Malang, A. Rowcliffe, and M. Ulrickson. Blanket/first wall challenges and required R&D on the pathway to DEMO . *Fusion Eng. Design*, 100:2 – 43, 2015.

[10] M. Abdou, G. D. Morgan, et al. Blanket comparison and selection study. In *ANL/FPP-83-1*. Argonne National Laboratory, 1983.

[11] A. Y. Ying and A. A Gaizer. The effects of imperfect insulator coatings on mhd and heat transfer in rectangular ducts. *Fusion Eng. Des.*, 27:634–641, 1995.

[12] A. Gaizer and M. Abdou. Effects of imperfect insulating coatings on the flow partitioning between parallel channels in self-cooled liquid metal blankets. *Fusion Technology*, 30, 1996.

[13] C. Mistrangelo and L. Bühler. *Magnetoconvection in HCLL blankets*, volume 7672. KIT Scientific Publishing, 2014.

[14] J. F. Salavy, G Aiello, O David, F Gabriel, L Giancarli, C Girard, N Jonqueres, G Laffont, S Madeleine, Y Poitevin, and G. Rampal. The HCLL Test Blanket Module system: Present reference design, system integration in ITER and R&D needs. *Fusion Eng. Des.*, 83:1157–1162, 2008.

[15] G. Rampal, Y. Puma, AL.and Poitevin, E. Rigal, and C. Szczepanski, J.and Boudot. HCLL TBM for ITER-design studies. *Fusion Eng. Des.*, 75:917–922, 2005.

[16] S. Smolentsev, R. Moreau, and M. Abdou. Characterization of key magnetohydrodynamic phenomena for PbLi flows for the US DCLL blanket. *Fusion Eng. Design*, 83:771–783, 2008.

[17] S. Smolentsev, N. B. Morley, M. A. Abdou, and S. Malang. Dual-coolant lead–lithium (dcll) blanket status and r&d needs. *Fusion Eng. Des.*, 100:44–54, 2015.

[18] P. A. Davidson. *An Introduction to Magnetohydrodynamics*. Cambridge University Press, 2001.

[19] I. R. Kirillov et al. Lithium cooled blanket of rf demo reactor. *Fusion Eng. Des.*, 49:457–465, 2000.

[20] I. A. Belyaev, Ya. I. Listratov, N. G. Razuvanov, and V. G. Sviridov. Liquid metal heat transfer in inclined tube affected by longitudinal magnetic field. In *Proc. 8^{th} PAMIR Conf. Fund. Appl. MHD, Borgo, Corsica, France*, pages 43–47. INP, Open Library, 2011.

[21] L. G. Genin, V. G. Zhilin, Y. P. Ivochkin, N. G. Razuvanov, V. G. Sviridov, A. A. Shestakov, and E. V. Sviridov. Liquid metal heat transfer in a vertical tube affected by transverse magnetic field. In *Proc. 8^{th} PAMIR Conf. Fund. Appl. MHD, Borgo, Corsica, France*, pages 31–35. INP, Open Library, 2011.

[22] I. A. Belyaev, L. G. Genin, Ya. I. Listratov, I. A. Melnikov, V. G. Sviridov, E. V. Sviridov, Yu. P. Ivochkin, N. G. Razuvanov, and Yu. S. Shpansky. Specific features of liquid metal heat transfer in a tokamak reactor. *Magnetohydrodynamics*, 49:177–190, 2013.

[23] I. A. Melnikov, E. V. Sviridov, V. G. Sviridov, and N. G. Razuvanov. Heat transfer of mhd flow: experimental and numerical research. In *Proc. 9^{th} PAMIR Conf. Fund. Appl. MHD, Riga, Latvia*, volume 1, pages 65–69. INP, Open Library, 2014.

[24] I. Poddubnyi, N. Razuvanov, V. Sviridov, and Yu. Ivochkin. Experimental research of the heat transfer liquid metal downwards flow in rectangular duct in magnetic field. In *Proc. 9^{th} PAMIR Conf. Fund. Appl. MHD, Riga, Latvia*, volume 1, pages 330–334. INP, Open Library, 2014.

[25] I. A. Melnikov, E. V. Sviridov, V. G. Sviridov, and N. G. Razuvanov. Experimental investigation of MHD heat transfer in a vertical round tube affected by transverse magnetic field. *Fusion Eng. Des.*, 112:505–512, 2016.

[26] N. Vetcha, S. Smolentsev, M. Abdou, and R. Moreau. Study of instabilities and quasi-two-dimensional turbulence in volumetrically heated magnetohydrodynamic flows in a vertical rectangular duct. *Phys. Fluids*, 25(2):024102, 2013.

[27] O. Zikanov, Ya. Listratov, and V. G. Sviridov. Natural convection in horizontal pipe flow with strong transverse magnetic field. *J. Fluid Mech.*, 720:486–516, 2013.

[28] C. Mistrangelo and L. Bühler. Magneto-convective flows in electrically and thermally coupled channels. *Fusion Eng. Design*, pages 5–9, 2013.

[29] X. Zhang and O. Zikanov. Mixed convection in a horizontal duct with bottom heating and strong transverse magnetic field. *J. Fluid Mech.*, 757:33–56, 2014.

[30] X. Lv and O. Zikanov. Mixed convection in horizontal duct flow with transverse magnetic field and heating of side wall. *Phys. Fluids*, 26(9):097106, 2014.

[31] L. Liu and O. Zikanov. Elevator mode convection in flows with strong magnetic fields. *Phys. Fluids*, 27(4):044103, 2015.

[32] Ya. Listratov, I. Melnikov, N. Razuvanov, V. Sviridov, and O. Zikanov. Convection instability and temperature fluctuations in a downward flow in a vertical pipe with strong transverse magnetic field. In *Proc. 10^{th} PAMIR Conf. Fund. Appl. MHD, Cagliari, Italy*, volume 1. INP, Open Library, 2016.

[33] O. Zikanov and Ya. Listratov. Numerical investigation of MHD heat transfer in a vertical round tube affected by transverse magnetic field. *Fusion Eng. Des.*, 113:151–161, 2016.

[34] J. C. R. Hunt and R. Hancox. *The use of liquid lithium as coolant in a toroidal fusion reactor*. Technical Report CLM-R 115, Culham Lab., England, 1971.

[35] H. Madrame, K. Taghavi, and M.S. Tillack. The influence of leakage currents on mhd pressure drop. *Fusion Technol.;*, 8, 1985.

[36] D. L. Smith, C. C. Baker, D. K. Sze, G. D. Morgan, M. A. Abdou, S. J. Piet, K. R. Schultz, R. W. Moir, and J. D. Gordon. Overview of the blanket comparison and selection study. *Fusion Sci. Technol.*, 8(1P1):10–44, 1985.

[37] S. Malang, K. Arheidt, L. Barleon, H.U. Borgstedt, V. Casal, U. Fischer, W. Link, J. Reimann, K. Rust, and G. Schmidt. Self-cooled liquid-metal blanket concept. *Fusion Technol.*, 14(3), 1988.

[38] T. Q. Hua and Walker J. S. Three-dimensional mhd flow in insulating circular ducts in non-uniform transverse magnetic fields. *Int. J. of Eng. Sci.*, 27(9):1079–1091, 1989.

[39] T. J. Moon and J. S. Walker. Liquid metal flow through a sharp elbow in the plane of a strong magnetic field. *J. Fluid Mech.*, 213:397–418, 1990.

[40] S. Molokov and L. Bühler. Liquid metal flow in a u-bend in a strong uniform magnetic field. *J. Fluid Mech.*, 267:325–352, 1994.

[41] R. Stieglitz, L. Barleon, L. Bühler, and S. Molokov. Magnetohydrodynamic flow in a right-angle bend in a strong magnetic field. *J. Fluid Mech.*, 326:91–123, 1996.

[42] S. Molokov, R. Moreau, and H. K. Moffatt. *Magnetohydrodynamics: Historical evolution and trends*. Springer, Berlin, 2007.

[43] R. P. Feynman, R. B. Leighton, and M. Sands. *The Feynman lectures on physics, vol. 2: Mainly electromagnetism and matter*. Addison-Wesley, 1979.

[44] D. D. Gray and A. Giorgini. The validity of the boussinesq approximation for liquids and gases. *Int. J. Heat Mass Transfer.*, 19(5):545–551, 1976.

[45] N. Vetcha, S. Smolentsev, and M. Abdou. Theoretical study of mixed convection in poloidal flows of DCLL blanket. *Fusion Sci. Technol.*, 56(2):851, 2009.

[46] C. Mistrangelo and L. Bühler. Numerical analysis of buoyant-convective liquid metal flow in channels exposed to strong magnetic fields. In *Fusion Engineering (SOFE), 2011 IEEE/NPSS 24th Symposium on*, pages 1–6. IEEE, 2011.

[47] W. Ni, S. Qiu, G. Su, W. Tian, and Y. Wu. Numerical investigation of buoyant effect on flow and heat transfer of Lithium–Lead Eutectic in DFLL–TBM. *Progress in Nuclear Energy*, 58:108–115, 2012.

[48] S. Smolentsev, M. Morley, and M. Abdou. MHD and thermal issues of the SiCf/SiC flowchannel insert. *Fusion Sci. Technol.*, 50:107–119, 2006.

[49] J. Sommeria and R. Moreau. Why, how and when MHD-turbulence becomes two-dimensional. *J. Fluid Mech.*, 118:507–518, 1982.

[50] K. Moffatt. On the suppression of turbulence by a uniform magnetic field. *J. Fluid Mech.*, 23:571–592, 1967.

[51] D. Krasnov, O. Zikanov, and T. Boeck. Comparative study of finite difference approaches to simulation of magnetohydrodynamic turbulence at low magnetic Reynolds number. *Comp. Fluids*, 50:46–59, 2011.

[52] D. Krasnov, O. Zikanov, and T. Boeck. Numerical study of magnetohydrodynamic duct flow at high Reynolds and Hartmann numbers. *J. Fluid Mech.*, 704:421–446, 2012.

[53] Yu. Zhao and O. Zikanov. Instabilities and turbulence in magnetohydrodynamic flow in a toroidal duct prior to transition in Hartmann layers. *J. Fluid Mech.*, 692:288–316, 2012.

[54] X. Nicolas, J. M. Luijkx, and J. K. Platten. Linear stability of mixed convection flows in horizontal rectangular channels of finite transversal extension heated from below. *Int. J. Heat Mass Transfer.*, 43(4):589–610, 2000.

[55] Y. Morinishi, T. S. Lund, O. V. Vasilyev, and P. Moin. Fully conservative higher order finite difference schemes for incompressible flow. *J. Comp. Phys.*, 143:90–124, 1998.

[56] M. Ni, R. Munipalli, P. Huang, N. B. Morley, and M. A. Abdou. A current density conservative scheme for incompressible MHD flows at a low magnetic Reynolds number. Part I: On a rectangular collocated grid system. *J. Comp. Phys.*, 227:174–204, 2007.

[57] O. Zikanov. *Essential computational fluid dynamics*. Wiley, Hoboken, NJ, 2010.

[58] J. C. Adams, P. Swarztrauber, and R. Sweet. Efficient fortran subprograms for the solution of separable elliptic partial differential equations. http://www.cisl.ucar.edu/css/software/fishpack/, 1999.

[59] H. J. H. Clercx and G. J. F. van Heijst. Two-dimensional Navier-Stokes turbulence in bounded domains. *Appl. Mech. Rev.*, 62:02082, 2009.

[60] D. Goluskin and E. A. Spiegel. Convection driven by internal heating. *Physics Letters A*, 377(1):83–92, 2012.

[61] O. Zikanov and A. Thess. Direct numerical simulation of forced MHD turbulence at low magnetic Reynolds number. *J. Fluid Mech.*, 358:299–333, 1998.

[62] T. Boeck, D. Krasnov, and E. Zienicke. Numerical study of turbulent magnetohydrodynamic channel flow. *J. Fluid Mech.*, 572:179, 2007.

[63] P. Dey and O. Zikanov. Turbulent flow and transport of passive scalar in magnetohydrodynamic channel flows with different orientations of magnetic field. *Int. J. Heat Fluid Flow*, 36:101–117, 2012.

[64] D. Krasnov, A. Thess, T. Boeck, Y. Zhao, and O. Zikanov. Patterned turbulence in liquid metal flow: Computational reconstruction of the Hartmann experiment. *Phys. Rev. Lett.*, 110:084501, 2013.

[65] X. Zhang and O. Zikanov. Thermal convection in a duct with strong axial magnetic field. *Magnetohydrodynamics*, 2017. In press.

[66] A. Vorobev and O. Zikanov. Instability and transition to turbulence in a free shear layer affected by a parallel magnetic field. *J. Fluid Mech.*, 574:131–154, 2007.

[67] A. Thess and O. Zikanov. Transition from two-dimensional to three-dimensional magnetohydrodynamic turbulence. *J. Fluid Mech.*, 579:383–412, 2007.

[68] I. R. Kirillov, D. M. Obukhov, L. G. Genin, V. G. Sviridov, N. G. Razuvanov, V. M. Batenin, I. A. Belyaev, I. I. Poddubnyi, and N. Yu. Pyatnitskaya. Buoyancy effects in vertical rectangular duct with coplanar magnetic field and single sided heat load. *Fusion Eng. Des.*, 104:1–8, 2016.

[69] T. Alboussière, J. P. Garandet, and R. Moreau. Buoyancy-driven convection with a uniform magnetic field. Part 1. Asymptotic analysis. *J. Fluid Mech.*, 253:545–563, 1993.

[70] T. P. Lyubimova, D. V. Lyubimov, V. A. Morozov, R. V. Scuridin, H. B. Hadid, and D. Henry. Stability of convection in a horizontal channel subjected to a longitudinal temperature gradient. Part 1. Effect of aspect ratio and Prandtl number. *J. Fluid Mech.*, 635:275–296, 2009.

[71] M.W. Frank et al. Viscous fluid flow. *McGraw-Hill, New York*, 1991.

[72] P. A. Davidson. The role of angular momentum in the magnetic damping of turbulence. *J. Fluid Mech.*, 336:123–150, 1997.

[73] A. Potherat, J. Sommeria, and R. Moreau. An effective two-dimensional model for MHD flows with transverse magnetic field. *J. Fluid Mech.*, 424:75–100, 2000.

[74] A. Pothérat, J. Sommeria, and Moreau R. Numerical simulations of an effective two-dimensional model for flows with a transverse magnetic field. *J. Fluid Mech.*, 534:115–143, 2005.

[75] P. K. Kundu, I. M. Cohen, and D. R. Dowling. *Fluid Mechanics*. Academic Press, 2012.